INFORMATION TO USERS

This manuscript has been reproduced from the microfilm master. UMI films the text directly from the original or copy submitted. Thus, some thesis and dissertation copies are in typewriter face, while others may be from any type of computer printer.

The quality of this reproduction is dependent upon the quality of the copy submitted. Broken or indistinct print, colored or poor quality illustrations and photographs, print bleedthrough, substandard margins, and improper alignment can adversely affect reproduction.

In the unlikely event that the author did not send UMI a complete manuscript and there are missing pages, these will be noted. Also, if unauthorized copyright material had to be removed, a note will indicate the deletion.

Oversize materials (e.g., maps, drawings, charts) are reproduced by sectioning the original, beginning at the upper left-hand corner and continuing from left to right in equal sections with small overlaps.

Photographs included in the original manuscript have been reproduced xerographically in this copy. Higher quality 6" x 9" black and white photographic prints are available for any photographs or illustrations appearing in this copy for an additional charge. Contact UMI directly to order.

Bell & Howell Information and Learning
300 North Zeeb Road, Ann Arbor, MI 48106-1346 USA

UMI®
800-521-0600

POWER AND SPECTRAL CHARACTERIZATION OF InGaAsP-InP MULTI-QUANTUM WELL LASERS

By
KELVIN PROSYK, B. SC.

A Thesis

Submitted to the School of Graduate Studies

in Partial Fulfilment of the Requirements

for the Degree

Doctor of Philosophy

McMaster University

CHARACTERIZATION OF InGaAsP-InP MQW LASERS

DOCTOR OF PHILOSOPHY (1998) McMaster University

(Engineering Physics) Hamilton, Ontario

TITLE: Power and Spectral Characterization of InGaAsP-InP Multi-Quantum Well Lasers

AUTHOR: Kelvin Prosyk, B. Sc. (University of Waterloo)

SUPERVISOR: Dr. J. G. Simmons

NUMBER OF PAGES: xiii, 163

ABSTRACT

A detailed study is presented of power and spectral measurement methodology commonly used to characterize and optimize the fundamental continuous-wave properties of semiconductor lasers. These properties include: efficiency, optical loss, the temperature sensitivity of threshold, gain, and spectral linewidth. The techniques studied are found to often yield erroneous or misleading results. The conditions under which errors can occur are investigated and precautionary measures necessary to avoid these problems are outlined.

The effect of well number, length, and temperature on efficiency and optical loss is investigated. A phenomenological model based on inter-valence band absorption (IVBA) for the description of the results is developed. The model provides evidence of the importance of IVBA in determining laser characteristics, including the failure to lase. The operating regime where IVBA dominates is found to be clearly identifiable. It is also found that, in the presence of IVBA, there exists a potential for misleading measurements of the internal efficiency and the optical loss. Using the high temperature sensitivity of the gain coefficient, it is possible to obtain an indication as to whether IVBA is affecting the experimental results.

In order to study the temperature dependence of the threshold current, a derivation of the empirical T_{max} relation is given which provides meaning to the fitting parameters. The experimentally determined T_{max} is shown to correlate with the T_{max} predicted from data obtained by the IVBA model for a range of lengths and well numbers. The conditions under which the T_{max} relation is valid are determined.

The gain coefficient for lasers having five quantum wells is calculated theoretically

and compared to the gain coefficient obtained experimentally both from the IVBA model for efficiency and from the length dependence of the threshold current density. The efficiency method agrees with theory to within experimental error. However, the threshold method yields a value which is approximately one-half of the theoretical value, a phenomenon which has been previously observed in the literature but for which no explanation has been found. Direct measurement of the below-threshold output spectrum of the lasers demonstrates that the cause of this discrepancy is an unexpected length dependence of the gain coefficient. Non-uniform carrier injection into the quantum wells is suggested as a possible physical mechanism.

A potential for gross inaccuracies in the measurement of laser linewidth using the delayed self-homodyne (DSH) technique is discovered. It is found that the accuracy of the DSH technique depends on the amount of noise in the laser bias current source to a previously unappreciated degree. This is due to a combination of the high FM sensitivity of semiconductor lasers and the long optical delay lines required by the DSH technique. The errors behave in a manner usually associated with intrinsic 1/f noise, and can cause all of the associated properties of residual linewidth, linewidth floor, non-Lorentzian lineshape, and premature re-broadening of the laser line. Guidelines for proper filtering of the current source are given to ensure accurate measurement.

ACKNOWLEDGMENTS

I would like to thank my supervisor, Dr. John Simmons. Your support and gentle guidance has been invaluable over the years. To Dr. John Goodwin, whose idea and equipment is responsible for Chapter 6, I owe many thanks, in particular for giving me a glimpse of what it is to be an experimental wizard. I am grateful to Nortel Technology for the lasers used in this thesis, and to Dr. Jack Evans, who acted as a liaison with Nortel and from whom I inherited a lab full of useful equipment. Kudos go to Rob Kalnins, Mike Moyer and James Gazzola, who assisted me in the lab during their summer work terms and who proved by their ability that they deserved to be top Engineering Physics graduates.

Finally, I would like to acknowledge the genius and insight of D. Bohm's ontological interpretation of quantum mechanics, as outlined in his book *The Undivided Universe*. His work should be a mandatory part of undergraduate quantum physics courses.

Kelvin Prosyk

December, 1997

TABLE OF CONTENTS

LIST OF FIGURES AND TABLES

PREFACE

Much of the work presented in this thesis has either been published by myself and co-authors during the course of my studies or will soon be published in a modified form. Where the journal of submission is known, a footnote has been provided at the beginning of the chapter. All theoretical calculations, experimental measurements and explanatory comments in this thesis are original work done by me during the period of my full-time Ph.D. studies at McMaster University, and have not received previous credit at this or any other institution.

CHAPTER ONE

INTRODUCTION

1.1 MOTIVATION

SEMICONDUCTOR lasers can be found in a wide range of applications, from common items such as compact disc players and high speed printers, to the esoteric and astonishing 1997 Sojourner sent to explore the Ares Vallis flood plain of Mars. The minute size, low power demands and low cost of these devices are attractive advantages.

Perhaps the greatest driving force behind progress in semiconductor lasers, however, is optical communications. With an emitting wavelength of 1.3 or 1.55 μm, they are used as transmitters in optical fibre links, either directly modulated or with an external modulator. At 0.98 μm, they can be used to pump Erbium-doped fibre amplifiers used as repeaters in long-distance links. The ability to design a range of emission wavelengths is useful for high-capacity wavelength division multiplexing (WDM), where a number of lasers at slightly different wavelengths are used to send a series of signals simultaneously. Not only are improved devices required for current communications demands, but proposals for future uses, such as fibre-to-the-home and land-line components for the

expansion of wireless networks, ensure that interest in semiconductor lasers will continue for some time.

Crucial to further progress in semiconductor lasers is an understanding of the underlying physics of the devices, as well as the development of an arsenal of meaningful characterization techniques. This is complicated by the small size (typically less than 1 mm cubed), the difficulty in physically accessing the inside of the laser in a non-destructive manner, and the high degree of coupling that exists between the various physical processes occurring during operation. As a result, many standard characterization techniques are indirect and rely on *a priori* models of laser behaviour. When the assumptions used to generate a model are invalid, experimental results can be misleading. If the original assumptions are not re-examined and corrected, consequences can range from numerical results which simply do not agree with theory, to the postulation of new but highly suspect physical mechanisms.

1.2 Historical Context

1.2.1 Evolution to Commercial Transmitters [1]

Successful lasing in a forward-biased GaAs p-n junction was first observed in 1962 [2]-[5]. Later improvements in liquid phase epitaxy led to room-temperature, pulsed-mode lasing action in 1969 [6]. In 1970, the first continuous-wave (CW) room-temperature semiconductor laser was demonstrated [7]. Since these lasers were based on GaAs, the lasing wavelength was usually in the range of 0.8-0.9 μm.

The advent of low-loss optical fibre in the 1.3-1.55 μm wavelength range led to a pursuit for lasers operating in the infrared. InGaAsP lasers on InP substrates provided a viable solution, and in 1977 a 1.3 μm InGaAsP/InP laser was demonstrated [8], with lasing at 1.55 μm soon to follow. By 1984, InGaAsP/InP lasers in long-haul optical

communication systems had been introduced commercially [9].

1.2.2 Characterization of Threshold

Since the first semiconductor laser, improvements to the threshold current and electrical-to-optical conversion efficiency have been sought. Between 1962 and 1975, the threshold current density had decreased by over two orders of magnitude [1]. Further progress was made by: improvements in the design of the device geometry [10]; the introduction of thin (< 500 Å) narrow bandgap epilayers which act to form a quantum well potential for carriers in the crystal [11], [12]; and the intentional introduction of lattice-mismatch strain into the quantum wells [13]. An example of a multi-quantum well laser with a ridge to confine the current and optical mode is shown in Fig. 1.1.

In addition to an overall reduction in current consumption, a reduction in the temperature sensitivity of threshold current is also desirable. The ambient temperature in a

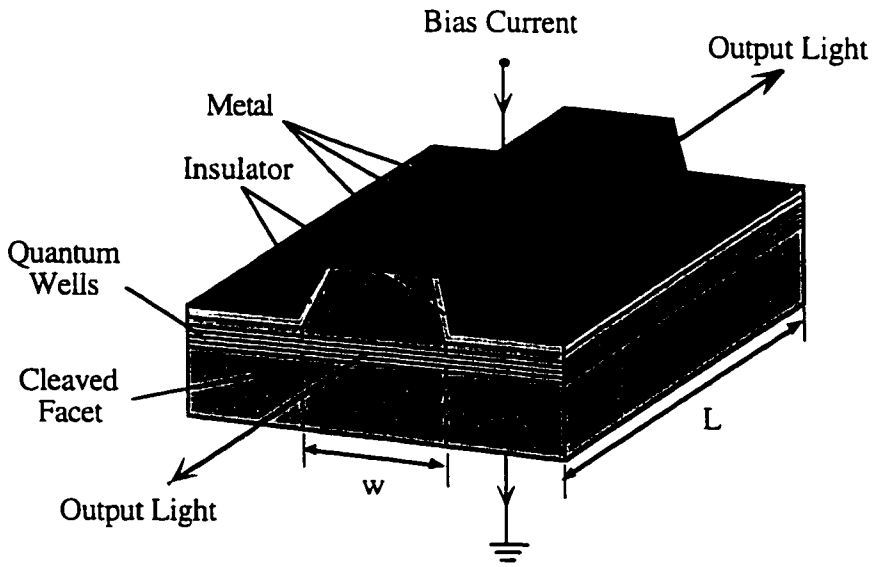

Figure 1.1 - The basic structure of a multi-quantum well ridge-waveguide semiconductor laser.

transmitter or repeater module can exceed 50°C [14], and typical industrial standards require an operating range of -40°C to 85°C. Presently, thermo-electric (TE) coolers are usually used to stabilized the temperature of the laser. However, TE coolers add significantly to the cost of packaging, increase package volume, require additional sensing and control circuitry, and can consume upwards of one hundred times the power needed to operate the lasers which they are cooling. Since TE coolers are inefficient, they generate excess heat and, furthermore, can often be unreliable.

The ultimate goal, therefore, of characterizing the temperature sensitivity of the threshold current is the development of a laser module which does not require a TE cooler. However, this is complicated since InGaAsP/InP lasers have a notoriously high sensitivity to temperature [15], the cause of which is not fully understood. At the time of this writing there appears to be a consensus forming around changes in the gain as the primary contributor [16], [17] but there is still much controversy. In addition, while the theoretical temperature dependence of the gain due to softening of the Fermi distribution can be used to successfully predict the temperature sensitivity in GaAs/AlGaAs ($T_0 \approx 200 - 400$ K) [18], this is not the case for InGaAsP/InP. Although the theoretical calculation for quaternary lasers yields approximately the same result as the ternaries [1], the observed temperature sensitivity is much higher ($T_0 \approx 40 - 70$ K [1]), and does not improve as much as predicted with the introduction of quantum wells [19]. If gain is the main culprit, further investigation is required into what material property makes it so.

One complicating factor from the experimental point of view has been the concise description of the temperature dependence of threshold. Since 1968 [20], the threshold current density, J_{th}, has been associated with an exponential temperature dependence:

$$J_{th} = J_p e^{T/T_0} \qquad (1.1)$$

where T_0 and J_p are the characteristic temperature and current density, respectively.

Unfortunately, the observed J_{th} does not follow this behaviour and T_0 and J_p depend on temperature. This has led to the custom of dividing the observed temperature range into arbitrary sub-ranges over which T_0 and J_p are relatively constant, which unnecessarily complicates the analysis. In 1995, it was noted that a strong correlation existed between J_{th} and its temperature derivative, $\nabla_T J_{th}$, given by [15]

$$\frac{J_{th}^m}{\nabla_T J_{th}} = D \qquad (1.2)$$

where D and m are constants, and m was found to have a value of close to 3/2. Equation (1.2) was found to be valid for a wide temperature range (-50°C to 100°C) and a variety of laser designs.

1.2.3 Efficiency Characterization

Characterization of the laser efficiency is usually treated separately from the threshold current. This is accomplished by measuring the slope of the light output *vs.* current (L-I) curve above threshold. Less work has been done directly on the slope efficiency than on threshold, with the assumption being that the two are affected by similar mechanisms.

The external differential quantum efficiency, η_d, is defined as

$$\eta_d = \frac{\text{change in rate of photons escaping from cavity}}{\text{change in rate of carriers injected into cavity}}$$

and the internal differential quantum efficiency, η_i, is

$$\eta_i = \frac{\text{change in rate of photons produced in cavity}}{\text{change in rate of carriers injected into cavity}}$$

The efficiencies η_d and η_i can be related by [1], [21], [22]

$$\eta_d^{-1} = \eta_i^{-1}\left(1 + \frac{\alpha L}{\ln(1/R)}\right) \qquad (1.3)$$

where α is the optical loss per unit length, L is the cavity length, and R is the facet reflectivity. The standard characterization technique involves plotting η_d^{-1} as a function of L and extracting η_i and α from the slope and intercept.

Both η_i and α have been examined periodically and, at various times, one or the other has been ascribed the temperature and structural behaviour of η_d. An early detailed study in quaternary lasers was given by Adams *et. al.* [23] in 1980, who attributed the temperature dependence of η_d primarily to inter-valence band absorption (IVBA) affecting α. In 1987, Koren *et. al.* [24] noted a weak length dependence of η_d, and similarly attributed it to IVBA. They pointed out that an IVBA contribution to α would impart to it an implicit length dependence which would give rise to a difference between the actual and measured values of η_i and α, as obtained from (1.3). Studies by other groups investigated IVBA with regard to departures from the linear length dependence in (1.3) [25], and changes of η_d with changes in the band structure [26], [27]. In contrast, others have attributed the temperature dependence of η_d to changes in η_i induced by hetero-barrier leakage [28].

1.2.4 Gain Characterization

The fraction per unit length by which light is increased as it travels down the cavity is called the gain, and it is a fundamental quantity affecting the threshold current. It has the advantage that, for Fabry-Perot lasers, measurement requires fairly straightforward spectroscopy, and the calculation of the gain from the spectrum relies on reasonable assumptions. As a result, it is one of the most common CW diagnostic techniques after measuring the L-I curve.

The original method for extracting the gain from the below-threshold spectrum was

proposed by Hakki and Paoli in 1975 [29]. It was discovered, however, that the finite spectral resolution of monochromators used for the measurement could introduce significant systematic errors in the gain, particularly near threshold. This was pointed in 1984 by Cassidy [30], who also introduced a modified "mode sum/min" method which greatly improved the accuracy of the technique. Unfortunately, it is still possible to find publications basing conclusions on the Hakki-Paoli technique.

Since it is difficult to know the carrier concentration in the active region of a device, the gain is usually plotted as a function of current density, J. The gain also has a dependence on wavelength. Since the laser typically lases at the peak of the wavelength curve, it is this peak value, g, which is tracked as a function of J. In 1985, McIlroy *et. al.* [31] noticed that the theoretical g vs. J curve for $g > 0$ could be described by a logarithm,

$$g = \Gamma G_0 \ln(J / N_W J_{tr}) \tag{1.4}$$

where Γ is the optical confinement factor, N_W is the number of quantum wells, G_0 is the logarithmic gain coefficient, and J_{tr} is the transparency current density. The logarithmic dependence is observed experimentally, for example, by Osinski *et. al.* [32].

The logarithmic dependence can be used to predict the length dependence of the threshold current, or, alternatively, the length dependence of the threshold current can be used to infer ΓG_0 and J_{tr}. The latter is a common practice since it is often easier to cleave samples of different lengths and perform L-I measurements than it is to set up the spectroscopic and computational apparatus to measure the gain directly. At threshold, the gain is equal to the mirror losses, given by

$$g_{th} = \ln(1 / R) / L \tag{1.5}$$

Equations (1.4) and (1.5) can be combined to give

$$J_{th} = N_W J_{tr} \exp\{\ln(1 / R) / \Gamma G_0 L\}. \tag{1.6}$$

Equation (1.6) has been used to compare experimental ΓG_0 values with ones calculated theoretically at room temperature. Close agreement is often found, after some adjusting of unknown parameters [33]. However, large inexplicable discrepancies have also been found, notably in quaternary materials [33], [34].

Note that from (1.6), there exists a length at which the threshold current is a minimum. The threshold current at this length, $I_{th,min}$, is [31]

$$I_{th,min} = \frac{ew\ln(1/R)}{C}\frac{J_{tr}}{G_0} \qquad (1.7)$$

where w is the width of the contact supplying current to the laser. It is assumed that Γ is proportional to the number of quantum wells with a constant of proportionality C. Obviously, it is desirable to determine what mechanisms affect J_{tr} and G_0, and use this knowledge to increase G_0 and decrease J_{tr}.

1.2.5 Linewidth Measurements

Laser linewidth is of interest both for an understanding of the fundamental physics of lasers and from potential applications demanding pure (i. e., narrow linewidth) spectral sources. In terms of communications, analogue networks (such as cable television) require very narrow sources to reduce FM-to-AM noise conversion in optical fibre [35], [36].

Perhaps the most commonly used, simplest and highest resolution technique is laser self-homodyning and the closely related self-heterodyne technique. Self-homodyning was first proposed in 1980 [37], and has been used to investigate a variety of linewidth-related properties. Among these are the existence of a non-Lorentzian component in the lineshape [38], 1/f noise in the laser output [39], and departures from the Schawlow-Townes formula in the form of linewidth flooring, residual linewidth, and linewidth re-broadening [38], [40].

1.3 MATERIAL COVERED IN THIS THESIS

Continuous wave (CW) operation of semiconductor lasers is important for long-haul, high bit-rate communications where speed and dispersion considerations require external modulation. This thesis primarily deals with the CW *characterization* of semiconductor lasers, as opposed to the CW *characteristics*. In many cases, the two are inextricably bound together: the presence of certain characteristics requires the re-interpretation of some of the basic characterization techniques outlined in Section 1.2. The hope is that, in addition to providing an improved experimental methodology, some useful information regarding fundamental physical processes affecting the power and spectral properties of the lasers studied in this thesis will also be imparted. The lasers used for the various studies are compressively strained, multi-quantum well ridge waveguide InGaAsP/InP lasers. The lasers studied in Chapters 3 through 5 are Fabry-Perot type, while the one used in the linewidth study in Chapter 6 is a gain-coupled distributed-feedback laser.

The body of this thesis begins in Chapter 2 with a model of Fabry-Perot multi-quantum well lasers. The cavity is assumed defect-free and carriers are assumed to be evenly distributed along the length of the cavity. The underlying concepts behind the various models used in the subsequent chapters are presented in a coherent manner, and it shown that they can be used to reproduce some of the most fundamental properties of the laser: the optical spectrum, the L-I curve, gain saturation, and the Schawlow-Townes linewidth dependence on the output power.

In Chapter 3, a systematic study of the well number, length and temperature dependence of the efficiency and optical loss is presented. The study relies on data collected from a large set of 175 lasers. A model which includes IVBA is used to describe

the trends, and areas in parameter space where changes in the internal efficiency become significant are outlined. The consequences of the model and the measured parameters are examined.

In Chapter 4, the same set of lasers is examined for the temperature dependence of the threshold current. A modified version of (1.2) is derived from phenomenological considerations and used to give physical meaning to the shape of the J_{th} *vs.* temperature curve. The gain and loss coefficients measured in Chapter 3 are used to make predictions of the characteristic temperature, T_{max}, which are then compared to experiment.

A room-temperature investigation into the gain of lasers having 5 quantum wells is given in Chapter 5. The gain is calculated by four independent methods. The source of the occasionally observed discrepancy between the theoretical and experimental gain coefficients discussed in Section 1.2.4 is explored and identified, and possible root causes are discussed.

The effect of laser bias current noise on the self-homodyne (and self-heterodyne) technique for measuring laser linewidth is presented in Chapter 6. A mathematical description of the measurement apparatus is derived and extended to incorporate the presence of a single noise tone. The model is compared with experiment and further extended to describe a band of white current noise. Guidelines for filtering the current source to ensure accurate linewidth measurements are given.

REFERENCES

[1] G. P. Agrawal, N. K. Dutta, *Semiconductor Lasers*, 2nd ed., Van Nostrand Reinhold, 1993.

[2] R. N. Hall, G. E. Fenner, J. D. Kingsley, T. J. Soltys, R. O. Carlson, "Coherent light emission from GaAs junctions", *Phys. Rev. Lett.*, vol. 9, pp. 366-368, 1962.

[3] M. I. Nathan, W. P. Dumke, G. Burns, F. H. Dill Jr., G. Lasher, "Stimulated

emission of radiation from GaAs p-n junctions", *Appl. Phys. Lett.*, vol. 1, pp. 62-64, 1962.

[4] T. M. Quist, R. H. Rediker, R. J. Keyes, W. E. Krag, B. Lax, A. L. McWhorter, H. J. Zeiger, "Semiconductor maser of GaAs", *Appl. Phys. Lett.*, vol. 1, pp. 91-92, 1962.

[5] N. Holonyak Jr., S. F. Bevacqua, "Coherent (visible) light emissions from $Ga(As_{1-x}P_x)$ junctions", *Appl. Phys. Lett.*, vol. 1, pp. 82-83, 1962.

[6] I. Hayashi, M. B. Panish, P. W. Foy, "A low-threshold room-temperature injection laser", *IEEE J. Quantum, Electron.*, vol. QE-5, pp. 211-212, 1969.

[7] I. Hayashi, M. B. Panish, P. W. Foy, S. Sumski, "Junction lasers which operate continuously at room temperature", *Appl. Phys. Lett.*, vol. 17, pp. 109-111, 1970.

[8] K. Oe, S. Ando, K. Sugiyama, "1.3 μm CW operation of GaInAsP/InP DH diode lasers at room temperature", *Jpn. J. Appl. Phys.*, vol. 16, pp. 1273-1274, 1977.

[9] P. K. Runge, P. R. Trischitta, "The SL undersea lightwave system", *J. Lightwave Technol.*, vol. LT-2, pp. 744-753, 1984.

[10] G. H. B. Thompson, *Physics of Semiconductor Lasers*, John Wiley & Sons, 1980.

[11] R. D. Dupuis, P. D. Dapkus, R. Chin, N. Holonyak Jr., S. W. Kirchoefer, "Continuous 300 K operation of single-quantum-well $Al_xGa_{1-x}As$-GaAs heterostructure diodes grown by metalorganic chemical vapor deposition, *Appl. Phys. Lett.*, vol. 34, pp. 265-268, 1979.

[12] R. D. Dupuis, P. D. Dapkus, N. Holonyak Jr., R. M. Kolban, "Continuous room-temperature operation of multiple-quantum-well $Al_xGa_{1-x}As$-GaAs heterostructure diodes grown by metalorganic chemical vapor deposition", *Appl. Phys. Lett.*, vol. 35, pp. 487-490, 1979.

[13] J. D. Evans, T. Makino, N. Puetz, J. G. Simmons, D. A. Thompson, "Strain-induced performance improvements in long-wavelength, multiple-quantum-well ridge-waveguide lasers with all quaternary active regions", *IEEE Photon. Technol. Lett.*, vol. 4, pp. 299-301.

[14] T. P. Pearsall, ed., *GaInAsP Alloy Semiconductors*, Wiley & Sons, 1982.

[15] J. D. Evans, J. G. Simmons, D. A. Thompson, N. Puetz, T. Makino, G. Chik, "An investigation into the temperature sensitivity of strained and unstrained multiple quantum-well, long wavelength lasers: new insight and methods of characterization", *IEEE J. Select. Topics Quantum Electron.*, vol. 1, pp. 275-283, 1995.

[16] D. A. Ackerman, G. E. Shtengel, M. S. Hybersten, P. A. Morton, R. F. Kazarinov, T. Tanbun-Ek, R. A. Logan, "Analysis of gain in determining T_0 of 1.3 μm

semiconductor lasers", *IEEE J. Select. Topics Quantum Electron.*, vol. 1, pp. 250-262, 1995.

[17] H. J. Yi, J. Diaz, I. Eliashevich, M. Stanton, M. Erdtmann, X. He, L. J. Wang, M. Razeghi, "Temperature dependence of threshold current density J_{th} and differential efficiency η_d of high-power InGaAsP/GaAs ($\lambda = 0.8\,\mu m$) lasers", *Appl. Phys. Lett.*, vol. 66, pp. 253-255, 1995.

[18] N. K. Dutta, "Calculated threshold current of GaAs quantum well lasers", *J. Appl. Phys.*, vol. 53, pp. 7211-7214, 1982.

[19] W. T. Tsang, R. Kapre, M. C. Wu, Y. K. Chen, "Low-threshold InGaAs strained-layer quantum well lasers ($\lambda = 0.98\,\mu m$) with GaInP cladding layers prepared by chemical beam epitaxy", *Appl. Phys. Lett.*, vol. 61, pp. 755-757, 1992.

[20] J. I. Pankove, "Temperature dependence of emission efficiency and lasing threshold in laser diodes", *IEEE Photon. Technol. Lett.*, vol. 4, pp. 10-13, 1968.

[21] J. R. Biard, W. N Carr, B. S. Reed, "Analysis of a GaAs Laser", *Trans. Metallurgical Soc. AIME*, vol. 230, pp. 286-290, 1964.

[22] W. Streifer, D. R. Scifres, R. D. Burnham, "Analysis of diode laser properties", *IEEE J. Quantum Electron.*, vol. QE-18, pp. 1918-1929, 1982.

[23] A. R. Adams, M. Asada, Y. Suematsu, S. Arai, "The temperature dependence of the efficiency and threshold current of $In_{1-x}Ga_xAs_yP_{1-y}$ lasers related to intervalence band absorption", *Japn. J. Appl. Phys.*, vol. 19, pp. L621-L624, 1980.

[24] U. Koren, B. I. Miller, Y. K. Su, T. L. Koch, J. E. Bowers, "Low internal loss separate confinement heterostructure InGaAs/InGaAsP quantum well laser", *Appl. Phys. Lett.*, vol. 51, pp. 1744-1746, 1987.

[25] J. Z. Wilcox, S. Ou, J. J. Yang, M. Jansen, G. L. Peterson, "Dependence of external differential efficiency on laser length and reflectivities in multiple quantum well lasers", *Appl. Phys. Lett.*, vol. 55, pp. 825-827, 1989.

[26] K. Tanaka, K. Wakao, T. Yamamoto, H. Nobuhara, T. Fujii, "Dependence of differential quantum efficiency on the confinement structure in InGaAs/InGaAsP strained-layer multiple quantum-well lasers", *IEEE Photon. Tech. Lett.*, vol. 5, pp. 602-605, 1993.

[27] A. Kasukawa, T. Namegaya, N. Iwai, N. Yamanaka, Y. Ikegami, N. Tsukji, "Extremely high power 1.48 μm GaInAsP/InP GRIN-SCH strained MQW Lasers", *IEEE Photon. Tech. Lett.*, vol. 6, pp. 4-6, 1994.

[28] J. Diaz, I. Eliashevich, H. Yi, X. He, M. Stanton, M. Erdtmann, L. Wang, M. Razeghi, "Theoretical investigation of minority carrier leakage of high-power 0.8 μm InGaAsP/InGaP/GaAs laser diodes", *Appl. Phys. Lett.*, vol. 65, pp. 2260-2262,

1994.

[29] B. W. Hakki, T. L. Paoli, "Gain spectra in GaAs double-heterostructure injection lasers", *J. Appl. Phys.*, vol. 46, pp. 1299-1306, 1975.

[30] D. T. Cassidy, "Technique for measurement of the gain spectra of semiconductor diode lasers", *J. Appl. Phys.*, vol. 56, pp. 3096-3098, 1984.

[31] P. W. A. McIlroy, A. Kurobe, Y. Uematsu, "Analysis and application of theoretical gain curves to the design of multi-quantum-well lasers", *IEEE J. Quantum Electron.*, vol. QE-21, pp. 1958-1963, 1985.

[32] J. S. Osinski, P. Grodzinski, Y. Zou, P. D. Dapkus, "Threshold current analysis of compressive strain (0-1.8%) in low-threshold, long-wavelength quantum well lasers", *IEEE J. Quantum Electron.*, vol. 29, pp. 1576-1585, 1993.

[33] T. A. DeTemple, C. M. Herzinger, "On the semiconductor laser logarithmic gain-current density relation", *IEEE J. Quantum Electron.*, vol. 29, pp. 1246-1252, 1993.

[34] J. E. A. Whiteaway, G. H. B. Thompson, P. D. Greene, R. W. Glew, "Logarithmic gain/current density characteristic of InGaAs/InGaAlAs/InP multi-quantum-well separate-confinement-heterostructure lasers", *Electron. Lett.*, vol. 27, pp. 340-342, 1991.

[35] S. Yamamoto, N. Edagawa, H. Taga, Y. Yoshida, H. Wakabayashi, "Analysis of laser phase noise to intensity noise conversion by chromatic dispersion in intensity modulation and direct detection optical-fibre transmission", *J. Lightwav. Technol.*, vol. 8, pp. 1716-1722, 1990.

[36] K. Petermann, "FM-AM noise conversion in dispersive single-mode fibre transmission lines", *Electron. Lett.*, vol. 26, pp. 2097-2098, 1990.

[37] T. Okoshi, K. Kikuchi, A. Nakayama, "Novel method for high resolution measurement of laser output spectrum", *Electron. Lett.*, vol. 16, pp. 630-631, 1980.

[38] L. B. Mercer, "1/f frequency noise effects on self-heterodyne linewidth measurements", *J. Lightwav. Technol.*, vol. 9, pp. 485-492, 1991.

[39] K. Kikuchi, T. Okoshi, "Dependence of semiconductor laser linewidth on measurement time: evidence of the predominance of 1/f noise", *Electron. Lett.*, vol. 21, pp. 1011-1012, 1985.

[40] H. Yasaka, M. Fukuda, T. Ikegami, "Current tailoring for lowering linewidth floor", *Electron. Lett.*, vol. 24, pp. 760-762, 1988.

CHAPTER TWO

THEORETICAL FOUNDATIONS

2.0 INTRODUCTION

IN this chapter, the ground work is laid for analyses used later. The individual models presented in other chapters are brought together to illustrate that it is possible to use them in a cohesive manner. A trade-off is required between practicality and detail. At one extreme, numerical simulation of all known phenomena could be done by computer. This approach makes it difficult to perform quantitative fits to experimental data to determine unknown parameters. It also has the disadvantage that the interaction of various mechanisms can be obscured. At the other extreme, there is the danger of oversimplification. For example, many rate equation models ignore the variation in optical power along the length of the laser cavity, in favour of keeping a count of the total number of photons present in the cavity. Although this is simpler, it gives an incorrect relationship between gain and power output [1].

The model presented in this chapter is similar to that of Cassidy [2] and Gordon [3]. Modifications have been made to include quantum-well gain effects, inter-valence band absorption and current loss mechanisms. The carrier density along the length of the

laser cavity is assumed to be constant. This sacrifice is necessary to maintain tractable solutions when performing later quantitative analysis. More complicated models indicate that this assumption is not likely to introduce significant inaccuracies under CW conditions [4].

In Section 2.1 it is shown how the three-dimensional optical wave equation can be reduced to two separate problems: a two-dimensional bound problem in the transverse-lateral plane, and a one-dimensional traveling wave problem in the longitudinal direction. The spectral and optical power properties are derived in the longitudinal direction in Section 2.2. In Section 2.3, an alternative derivation for the optical power is presented using Poynting's theorem, and it is shown that the power in each cavity mode is separately conserved. The single-mode power equation is explored in Section 2.4, and a graphical example of the power spectral density is given in Section 2.5. In Section 2.6, a carrier equation for the net gain and a phenomenological relationship between current and carrier density is introduced. It is demonstrated that the model is capable of reproducing light output *vs.* current curves in Section 2.7. Section 2.8 contains a discussion of gain saturation, and Section 2.9 contains a derivation of the above-threshold spectral lineshape expected from this model.

2.1 THE OPTICAL MODE

The solution of the electromagnetic field in a semiconductor laser is inherently a three-dimensional problem. However, the field is generally bound in one or more low-order modes in two orthogonal directions and approximates a slowly varying traveling wave in the third. Considerable simplification takes place if the bound and traveling wave solutions are considered separately. In materials with complex indices of refraction, this cannot be done with an exact treatment. Fortunately, the problems can be decoupled if the real part of the refractive index is primarily responsible for the confinement of the bound

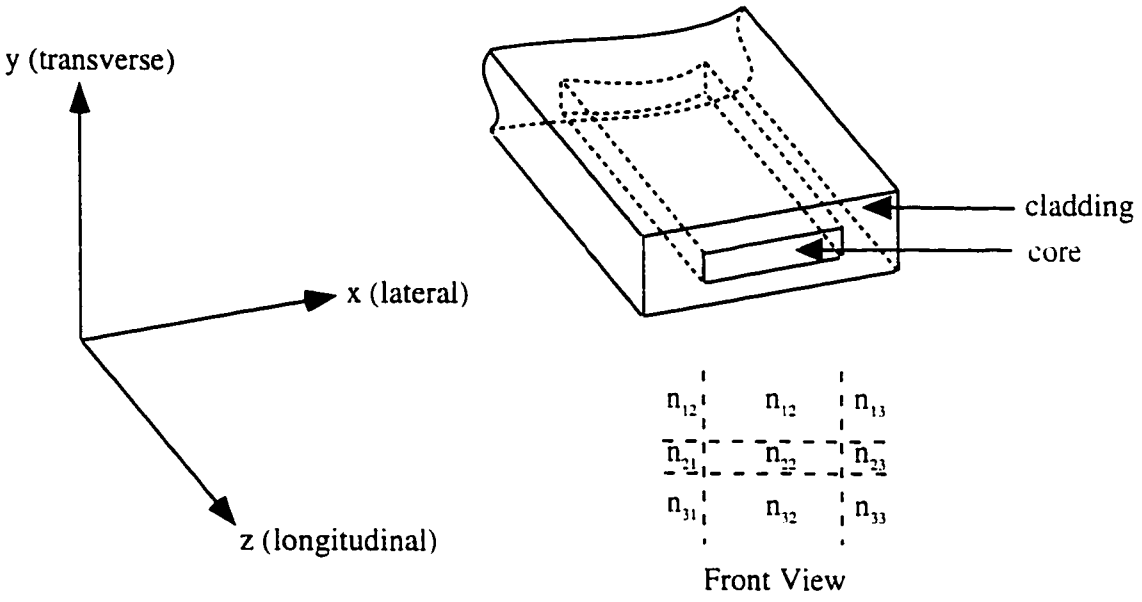

Figure 2.1 - Geometry of the optical waveguide in a laser, and the division into sections of the indices of refraction for the example of a 3x3 section laser. The transverse direction is the direction of growth on the wafer.

solutions. The contribution of the imaginary part of the refractive index is treated as perturbation in the following derivation based on Chuang [5], and Agrawal and Dutta [6].

Consider a waveguide as depicted in Figure 2.1 with a mode confined in the x (lateral) and y (transverse) directions, and free to propagate in the z (longitudinal) direction. Assuming that each material constituting the core and the cladding is linear, isotropic, homogeneous, non-magnetic and charge-neutral, the harmonic time-independent wave equation is

$$\nabla^2 E + [n(x,y)]^2 k_0^2 E = 0 \qquad (2.1)$$

where E is the electric field vector, n(x,y) is the complex index of refraction of each section and k_0 is 2π divided by the free space wavelength. One common approximate approach to solving (2.1) is called the effective index method [6]. In this approach, the waveguide is divided into sections where the refractive index is assumed constant. Each transverse

column of sections shown in Figure 2.1 is treated as a separate slab waveguide problem. A solution can be found for each of these ($\phi(y;x)$) and used to solve for the mode in the lateral direction $\psi(x)$. The electric field is therefore written as

$$\mathbf{E} \equiv \hat{\mathbf{e}}\phi(y;x)\psi(x)e^{i\beta z} \tag{2.2}$$

where β is the modal propagation constant and $\hat{\mathbf{e}}$ is the unit vector in the direction of polarization. Substituting (2.2) into (2.1) and performing a separation of variables gives differential equations for each of the transverse and lateral directions:

$$\frac{\partial^2\phi(y;x)}{\partial y^2} + \left[n^2(x,y)k_0^2 - \beta_{eff}^2(x)\right]\phi(y;x) = 0 \tag{2.3a}$$

$$\frac{\partial^2\psi(x)}{\partial x^2} + \left[\beta_{eff}^2(x) - \beta^2\right]\psi(x) = 0 \tag{2.3b}$$

where $\beta_{eff}^2(x)$ is the constant of separation.

Equation (2.3a) is solved for each transverse column with $\beta_{eff}(x)$ acting as the effective propagation constant. The β_{eff} for the k^{th} column ($\beta_{eff,k}$) can, in principle, be related to the power distribution by multiplying (2.3a) by the complex conjugate $\phi^*(y;x)$ and $\mathrm{Re}\{n_{jk}\}$, and integrating over all y:

$$\beta_{eff,k}^2 = \frac{\int_{-\infty}^{\infty} \mathrm{Re}\{n_{jk}\}\phi_k^*(y)\left[\frac{\partial^2\phi_k(y)}{\partial^2 y} + n_{jk}^2 k_0^2 \phi_k(y)\right]dy}{\int_{-\infty}^{\infty} \mathrm{Re}\{n_{jk}\}\phi_k^*(y)\phi_k(y)dy}. \tag{2.4}$$

In (2.4), the x dependence of ϕ and β_{eff} has been replaced with the column index and the (x,y) dependence of n has been replaced with row and column indices.

As mentioned, (2.1) can be solved in closed form if all n_{jk} are real ($n_{jk}^{(0)}$). This is treated as the unperturbed equation and has solutions $\phi^{(0)}$ and an effective propagation given by

$$\left(\beta_{eff,k}^{(0)}\right)^2 = \frac{\int_{-\infty}^{\infty} n_{jk}^{(0)}\phi_k^{(0)*}(y)\left[\frac{\partial^2\phi_k^{(0)}(y)}{\partial^2 y} + \left(n_{jk}^{(0)}\right)^2 k_0^2\phi_k^{(0)}(y)\right]dy}{\int_{-\infty}^{\infty} n_{jk}^{(0)}\phi_k^{(0)*}(y)\phi_k^{(0)}(y)dy} \quad . \tag{2.5}$$

Now consider a perturbative imaginary component to n_{jk}, denoted Δn_{jk}, so that

$$n_{jk} = n_{jk}^{(0)} + i\Delta n_{jk} \tag{2.6}$$

giving rise to a change in the propagation constant of $\Delta\beta_{eff,k}$ so

$$\beta_{eff,k} = \beta_{eff,k}^{(0)} + i\Delta\beta_{eff,k} \quad . \tag{2.7}$$

Since Δn_{jk} and $\Delta\beta_{eff,k}$ are considered to be small, n_{jk}^2 and $\beta_{eff,k}^2$ can be approximated by

$$n_{jk}^2 \approx \left(n_{jk}^{(0)}\right)^2 + 2i\Delta n_{jk} n_{jk}^{(0)} \quad , \tag{2.8a}$$

$$\beta_{eff,k}^2 \approx \left(\beta_{eff,k}^{(0)}\right)^2 + 2i\Delta\beta_{eff,k}\beta_{eff,k}^{(0)} \quad . \tag{2.8b}$$

At this point, something of a leap of faith is required. It is assumed appropriate to replace $\phi_k(y)$ with $\phi_k^{(0)}(y)$, without adding a $\Delta\phi_k(y)$ term as has been done in (2.6) and (2.7) with n_{jk} and $\beta_{eff,k}$, thereby eliminating unwanted cross-products in what follows. Unfortunately, this is not rigorously true. However, comparisons of approximate methods based on this assumption and exact numerical simulations agree favourably (a careful quantitative comparison between the two is given in [7]). Therefore, this *ad hoc* step is introduced as an inelegant but evidently practical part of the solution.

Substituting (2.8) and $\phi_k(y) \approx \phi_k^{(0)}(y)$ into (2.4), and canceling unperturbed terms using (2.5), $\Delta\beta_{eff,k}$ can be calculated as

$$\Delta\beta_{eff,k} = i\sum_j \Gamma_{jk}^T \Delta n_{jk} \frac{n_{jk}^{(0)} k_0^2}{\beta_{eff,k}} \tag{2.9}$$

where

$$\Gamma_{jk}^{T} \equiv \frac{n_{jk}^{(0)} \int_{\text{section j}} \phi_k^{(0)*} \phi_k^{(0)} dy}{\int_{-\infty}^{\infty} n_{jk}^{(0)} \phi_k^{(0)*} \phi_k^{(0)} dy}$$

is referred to as the transverse optical confinement factor, and represents the fraction of power of the transverse solution ϕ_k overlapping section j. The summation in (2.9) was obtained by breaking the infinite limits on the integral in the numerator of (2.4) into a series of integrations over each section j.

A similar procedure can now be carried out for $\psi(x)$. As in (2.4), the propagation constant can be written

$$\beta^2 = \frac{\int_{-\infty}^{\infty} \psi^*(x) \left[\frac{\partial^2 \psi(x)}{\partial y^2} + \beta_{\text{eff},k}^2 \psi(x) \right] dx}{\int_{-\infty}^{\infty} \psi^*(x) \psi(x) dx} . \qquad (2.10)$$

Note that (2.3b) has been multiplied only by $\psi^*(x)$ before integration, without the added factor of a refractive index used previously. One might be tempted to relate (2.10) more closely to the power distribution by multiplying by $n_{\text{eff},k} \equiv \beta_{\text{eff},k} / k_0$. However, it must be remembered that $\beta_{\text{eff},k}$ is merely a constant of separation and is not necessarily so easily used to obtain the optical power. Equation (2.10) is therefore used as given. In the lasers discussed in this thesis, the lateral confinement factor introduced below is nearly unity for the waveguide core and zero for the cladding, so that not having (2.10) easily expressible in terms of power is not a great inconvenience.

The presence of a Δn_{jk} will introduce a modification to the unperturbed propagation constant, k, given by

$$\beta = k + \Delta\beta \ . \qquad (2.11)$$

The symbol k is used instead of $\beta^{(0)}$ since it is a more conventional notation. Substituting (2.9) and (2.11) into (2.10), and once again canceling unperturbed terms, the change in propagation constant is found to be

$$\Delta\beta = \frac{-i}{2}\sum_{j,k}\Gamma_{jk}^{T}\Gamma_{k}^{L}g_{ij} \tag{2.12}$$

where

$$\Gamma_{k}^{L} \equiv \frac{\int_{\text{section j}}\psi^{*}(x)\psi(x)dx}{\int_{-\infty}^{\infty}\psi^{*}(x)\psi(x)dx}$$

and

$$g_{ij} \equiv \Delta n_{jk} n_{jk}^{(0)} \frac{k_0^2}{k} .$$

Note that it follows from the definitions of the confinement factors that

$$\sum_{j,k}\Gamma_{jk}^{T}\Gamma_{k}^{L} = 1 .$$

The parameter g_{ij} is the net gain per unit length of each section of the waveguide. A net modal gain can be defined as $g \equiv 2i\Delta\beta$. While the active region of the waveguide is often described in terms of gain, it is customary to discuss the passive sections in terms of their loss per unit length, $\alpha_{pass,ij} = -g_{ij}$. Finally, the gain/losses are usually lumped into active and passive terms so that

$$g = \Gamma g_{act} - (1-\Gamma)\alpha_{pass} \tag{2.13}$$

where Γ is the active region confinement factor, g_{act} is the net gain in the active region, and α_{pass} is the loss in the passive sections.

Equation (2.13) is the simple result of the rather involved derivation given above. Analysis is now greatly simplified since the non-axial distribution of the optical mode and the evolution of the wave as it travels down the axis are conveniently grouped into separate variables. The utility of this will become evident particularly in Chapters 3 and 5, where the gain and losses are examined in detail. Although a more sophisticated method for calculating Γ will be used, the principle outlined in this section is still valid.

2.2 LASER OPTICS I - FIELD SOLUTION

In Section 2.1, it was demonstrated that the three-dimensional problem of the electromagnetic field inside a dielectric waveguide with complex indices of refraction can be reduced to three one-dimensional problems in the presence of strong guiding by the real parts of the refractive indices. Attention can now be focused on the axial dimension where the field has an unbound, wavelike character with a wavelength much smaller than the length of the cavity. It is assumed that the gain is small enough that the wave can be treated as having a slowly varying amplitude.

Other than the presence of optical gain, two aspects make this problem particularly interesting: spontaneous emission and feedback from the ends of the cavity. The calculation of the longitudinal optical field starts by consideration of the spontaneous emission from a thin sheet of semiconductor centred about a point z_0 on the longitudinal axis. Since each photon has a random initial phase, they will be uncorrelated, as depicted in Fig. 2.2. There is an equal likelihood of a photon being emitted in the positive- or negative-going directions.

As discussed in Section 2.1, the propagation of the field will be described by $u = e^{-i\beta(z-z_0)}$ where $\beta = k - ig/2$, k is the propagation constant and g/2 is the amplitude gain of the field per unit length (so that g is the gain of the power). To be exact, a random phase angle should be added to the exponent. However, it does not affect the final result as

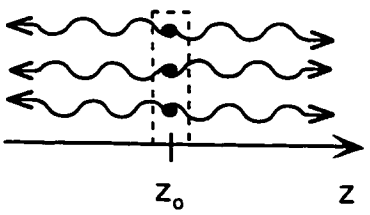

Figure 2.2 - Spontaneous emission from a sheet of material at z_0

long as it is remembered that adding this field to other ones which are not correlated must be done after squaring each to get the average power rather than adding them first.

The field induced by a spontaneous emission event will also have an amplitude, a(t). The amplitude contains a time dependence to account for broadening effects such as the finite transition lifetime. In this chapter, only the time-averaged power spectrum is considered and intensity noise is ignored, so the explicit time dependence of a(t) is dropped.

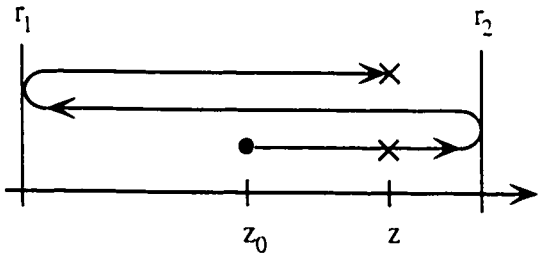

Figure 2.3 - The positive-going field at point z after two passes, emitted from point z_0 in the positive direction.

Now consider what happens when the source sheet and its accompanying gain medium are placed inside a Fabry-Perot etalon as shown in Fig. 2.3. Following the course of a single photon after emission, its amplitude and phase will progress as given by u(z) as it moves in the positive direction. After reflecting from the right hand mirror with reflection coefficient r_2, the amplitude inside the cavity will decrease and the wave will continue in the negative-going direction until it reflects off mirror r_1 and returns to propagating in the positive direction. Each round trip has a total travel length of 2L and will therefore contribute an additional factor of $r_1 r_2 e^{2i\beta L}$ to the field. The positive-going field at point $z > z_0$ after an infinite number of passes will be

$$a_+ u_+^+(z > z_0) = a_+ e^{i\beta(z-z_0)}\left(1 + r_1 r_2 e^{2i\beta L} + (r_1 r_2)^2 e^{4i\beta L} + \ldots\right)$$

$$= \frac{a_+ e^{i\beta(z-z_0)}}{1 - r_1 r_2 e^{2i\beta L}} \tag{2.14}$$

where the following notation has been used:

$$u^{\pm \text{ direction of propagation}}_{\pm \text{ direction of emission}}$$

and the subscript on the amplitude a indicates the direction of emission. Expressions similar to (2.14) can be easily derived for other combinations of propagation direction, direction of emission, and field point ($z > z_0$ or $z < z_0$). All of the eight possible combinations are summarized in Table 2.1.

Since it is the power and not the photon field that will be physically observed, it is that quantity which is of the greatest interest to calculate. The field amplitude is related to the amount of spontaneously emitted energy in both directions per unit length per unit time per unit frequency (e.g. - $J/(m \cdot s \cdot Hz)$). The average power spectral density (defined as the power per unit frequency, see [8] and [9]) of positive-going light at field point z due to a thin sheet of semiconductor of width dz centred at source point z_0 ($z > z_0$) is the sum of the contributions of the left and right emitted photons:

$$dP_v^+(z > z_0) = \frac{\gamma_{sp} u_{sp}(v)}{2} \left(\left| u_+^+(z > z_0) \right|^2 + \left| u_-^+(z > z_0) \right|^2 \right) dz_0 \tag{2.15}$$

with

$$|a_+|^2 = |a_-|^2 = \frac{\gamma_{sp} u_{sp}(v)}{2}$$

where γ_{sp} is the fraction of the spontaneous emission power coupled into the cavity and $u_{sp}(v)$ is the spontaneous emission power spectral density. The parameters $a_\pm$, γ_{sp}, and u_{sp} are assumed to be independent of z_0, or it is assumed that a suitable average γ_{sp} can

First Pass Configuration	Optical Field $u_{\pm}^{\pm}(z <> z_0)$	Power per Unit Source Length	Total Power
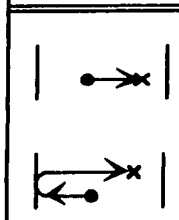	$\frac{a_+ e^{i\beta(z-z_0)}}{1-r_1r_2e^{2i\beta L}}$ $\frac{a_- r_1 e^{i\beta(z+z_0)}}{1-r_1r_2e^{2i\beta L}}$	$dP^+(z>z_0)/dz_0 =$ $Q\left(e^{g(z-z_0)} + R_1 e^{g(z+z_0)}\right)$	$P^+(z) =$ $\frac{Q}{g}\left\{\left[1-R_1+(1-R_2)R_1G\right]e^{gz} + R_1R_2G^2 - 1\right\}$
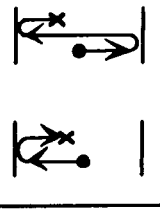	$\frac{a_+ r_1 r_2 e^{i\beta(2L-z_0+z)}}{1-r_1r_2e^{2i\beta L}}$ $\frac{a_- r_2 e^{i\beta(z+z_0)}}{1-r_1r_2e^{2i\beta L}}$	$dP^+(z<z_0)/dz_0 =$ $Q\left(R_1R_2G^2e^{g(z-z_0)} + R_1e^{g(z+z_0)}\right)$	
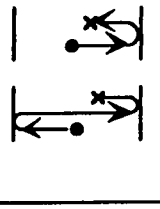	$\frac{a_+ r_2 e^{i\beta(2L-z_0-z)}}{1-r_1r_2e^{2i\beta L}}$ $\frac{a_- r_1 r_2 e^{i\beta(2L+z_0-z)}}{1-r_1r_2e^{2i\beta L}}$	$dP^-(z>z_0)/dz_0 =$ $Q\left(R_2Ge^{g(2L-z_0-z)} + R_1R_2Ge^{g(2L+z_0-z)}\right)$	$P^-(z) =$ $\frac{Q}{g}\left\{\left[1-R_2+(1-R_1)R_2G\right]e^{g(L-z)} + R_1R_2G^2 - 1\right\}$
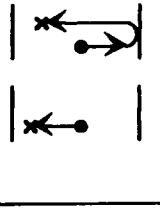	$\frac{a_+ r_2 e^{i\beta(2L-z_0-z)}}{1-r_1r_2e^{2i\beta L}}$ $\frac{a_- e^{i\beta(z_0-z)}}{1-r_1r_2e^{2i\beta L}}$	$dP^-(z<z_0)/dz_0 =$ $Q\left(R_2G^2e^{-g(z_0+z)} + e^{g(z_0-z)}\right)$	

Table 2.1 - Summary of optical field and intensity equations for a point source and a series of point sources inside a Fabry-Perot cavity. Variables are defined in the text. $Q \equiv \gamma_{sp} u_{sp}(\nu) / 2[(1-r_1r_2G)^2 + 4r_1r_2G\sin^2(kL)]$

be found for the integration that follows. The factor of 1/2 arises from the assumption that half of the spontaneously emitted energy will be coupled into each direction. There are four possible combinations of propagation direction and position relative to z_0 for dP/dz_0 and they are also summarized in Table 2.1. Equation (2.15) can be integrated over all source sheets along the length of the cavity to obtain the power spectral density along the cavity in the positive z direction,

$$\begin{aligned} P_\nu^+(z) &= \frac{\gamma_{sp}u_{sp}(\nu)}{2}\left\{\int_0^z \left|u_+^+(z>z_0)\right|^2 dz_0 + \int_z^L \left|u_-^+(z<z_0)\right|^2 dz_0\right\} \\ &= \frac{\gamma_{sp}u_{sp}(\nu)}{2g(\nu)} \cdot \frac{\left[1-R_1+(1-R_2)R_1G(\nu)\right]e^{gz} + R_1R_2[G(\nu)]^2 - 1}{\left(1-\sqrt{R_1R_2}G(\nu)\right)^2 + 4\sqrt{R_1R_2}G(\nu)\sin^2(\pi\nu/\nu_{FSR})} \end{aligned} \tag{2.16}$$

where $\nu_{FSR} = v_g / 2L$ is the free spectral range, v_g is the group velocity of the optical mode, $R_i = r_i^2$, and $G(\nu) = e^{g(\nu)L}$ is the single pass gain. $P_\nu^-(z)$ can be obtained by exchanging $R_1 \leftrightarrow R_2$ and $z \leftrightarrow L - z$. The output of the right facet, $P_{out}(\nu)$, according to (2.16) can be easily obtained as

$$\begin{aligned} P_{out}(\nu) &= (1-R_2)P_\nu^+(L) \\ &= \frac{\gamma_{sp}u_{sp}(\nu)(1-R_2)(G(\nu)-1)(1+R_1G(\nu))}{2g(\nu)\left[\left(1-\sqrt{R_1R_2}G(\nu)\right)^2 + 4\sqrt{R_1R_2}G(\nu)\sin^2(\pi\nu/\nu_{FSR})\right]}. \end{aligned} \tag{2.17}$$

Equation (2.17) is similar to the output of a Fabry-Perot etalon with an input beam of power $\gamma_{sp}u_{sp}(\nu)(G(\nu)-1)(1+R_1G(\nu))/2g(\nu)$ and a finesse which is calculated from the RG product rather than the reflectivity.

One further useful quantity is the power spectral density integrated over one cavity mode, P_m. As will be seen in section 2.3, while the power $P_\nu d\nu$ is not in general conserved, P_m is. The frequency dependence of the spontaneous emission and the gain are both assumed to be reasonably constant over one mode. New variables are defined: the spontaneous emission into mode m ($\gamma_{sp}u_{sp,m} = \gamma_{sp}u_{sp}(\nu)v_g / 2L$), the net gain of mode m, g_m, and the single-pass gain of m, G_m. Integrating (2.16) with respect to ν over

limits corresponding to the consecutive minima of one Fabry-Perot mode ($\nu / \nu_{FSR} = -1/2 \rightarrow 1/2$) gives

$$P_m^+(z) = \frac{\gamma_{sp} u_{sp,m}}{2} \frac{\left[1 - R_1 + (1 - R_2) R_1 G_m\right] e^{gz} + R_1 R_2 G_m^2 - 1}{g_m \left(1 - R_1 R_2 G_m^2\right)} \qquad (2.18)$$

It should be mentioned that the method of determining the field resulting from a single spontaneous emission event and integrating over all such events has been used in a more general form to determine the spectra of distributed feedback lasers [10]. This could be considered a closed form applicable to the special case of Fabry-Perot lasers.

2.3 LASER OPTICS II - CONSERVATION OF ENERGY†

Consider a thin closed surface pierced by the active material of the laser waveguide in the direction of propagation as shown in Fig. 2.4. The net rate of optical energy leaving this surface can be found by integrating the Poynting vector S over the entire area [11]. This will be equal to the net rate at which optical energy is created, less the rate at which it is stored or dissipated within the volume.

$$\oiint \mathbf{S} \cdot d\mathbf{a} = \iiint_V \left(r_r - \frac{\partial \rho}{\partial t} \right) dv \qquad (2.19)$$

where r_r is the net emission rate per unit volume and ρ is the energy density. The surface integral on the left side of (2.19) can be related to the volume it encloses by Gauss' theorem

$$\oiint \mathbf{S} \cdot d\mathbf{a} = \iiint_V (\nabla \cdot \mathbf{S}) dv \ . \qquad (2.20)$$

Equating the integrands of the volume integrals in (2.19) and (2.20) gives

$$\nabla \cdot \mathbf{S} = r_r - \frac{\partial \rho}{\partial t} . \qquad (2.21)$$

† This section is based on a derivation given by J. G. Simmons, "On the spatial and temporal dependence of photons and free carriers in a semiconductor medium", *EP727 Course Notes*, McMaster University, Canada. There, the energy flow is described in terms of photon continuity rather than the Poynting vector.

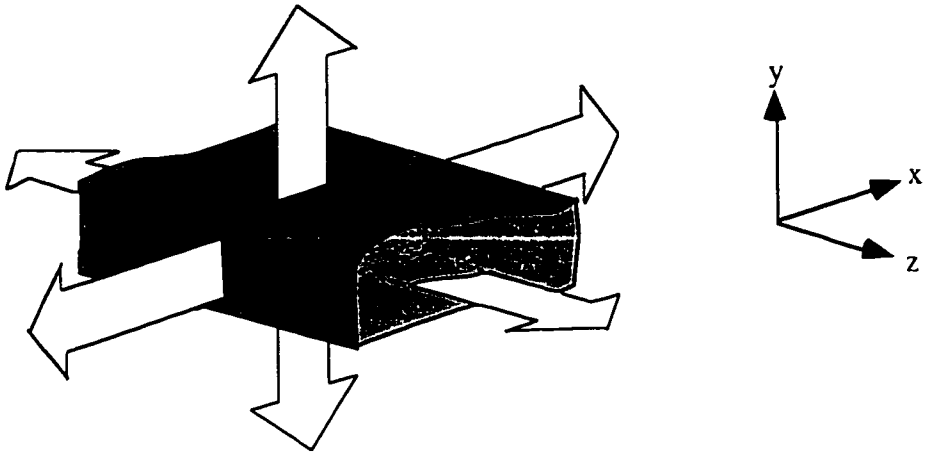

Figure 2.4 - A section of the laser waveguide showing the Gaussian surface (dashed) used in (2.19). The arrows indicate optical energy flow through the surfaces in the axial and perpendicular directions.

The components of **S** in the x and y directions represent an energy flow perpendicular to the direction of propagation and, hence, lost from the cavity. These losses can be lumped together as the energy loss rate per unit volume, $r_L = \partial S_x / \partial x + \partial S_y / \partial y$. The radiative rate r_r can be separated into a component representing the net rate of stimulated transitions (emission minus absorption), r_{st}, and the rate of spontaneous transitions, r_{sp}, so that $r_r = r_{st} + r_{sp}$. Under steady state conditions, $\partial \rho / \partial t = 0$ and (2.21) becomes

$$\frac{\partial S_z}{\partial z} = r_{st} + r_{sp} - r_L \qquad (2.22)$$

The stimulated emission rate is proportional to the energy density (Fermi's rule). For reasons which will become obvious, the constant of proportionality between the stimulated emission rate and the energy density is written as $v_g B$, where v_g is the group velocity in the z direction, and B is a proportionality factor so that $r_{st} = v_g B \rho$. Two main mechanisms contribute to r_L: light scattered from defects in the cavity and spontaneous emission which is not directed axially. The former will be proportional to ρ and is written

$v_g\alpha_{scat}\rho$, where α_{scat} is the proportionality factor, and the latter is a fraction of r_{sp}, given as $(1-\gamma_{sp})r_{sp}$, where $(1-\gamma_{sp})$ is the proportionality. Applying these modifications to (2.22) gives

$$\frac{\partial S_z}{\partial z} = v_g B\rho - v_g\alpha_{scat}\rho + \gamma_{sp}r_{sp} \tag{2.23}$$

Since S_z is the power per unit area propagating axially, it is related to ρ simply by $S_z = v_g\rho$. Things are simplified if S_z is considered to be a constant function of x and y (or it is assumed that a suitable average is found by the method outlined in Section 2.1) and written in terms of the power, $P = \Lambda S_z$, where Λ is the area of the active material. With the further definition of the net gain $g = B - \alpha_{scat}$ and $u_{sp} = \Lambda r_{sp}$, (2.23) can be written as a differential equation for the power as a function of z:

$$\frac{\partial P}{\partial z} = gP + \gamma_{sp}u_{sp} \tag{2.24}$$

where $\gamma_{sp}u_{sp}$ is considered independent of z.

Finally, P consists two independent populations of non-interacting photons propagating in the negative- (P^-) and positive- (P^+) going directions so that

$$P = P^+ + P^-,$$
$$\partial P/\partial z = \partial P^+/\partial z - \partial P^-/\partial z .$$

A separation of variables can be performed on (2.24) with the spontaneous emission divided equally between the two directions,

$$\frac{\partial P^+}{\partial z} - \frac{\partial P^-}{\partial z} = g\left(P^+ + P^-\right) + \gamma_{sp}u_{sp};$$

$$\Rightarrow \quad \frac{\partial P^+}{\partial z} = gP^+ + \frac{\gamma_{sp}u_{sp}}{2}, \tag{2.25a}$$

$$-\frac{\partial P^-}{\partial z} = gP^- + \frac{\gamma_{sp}u_{sp}}{2}. \tag{2.25b}$$

In order to solve the simultaneous differential equations in (2.25), boundary

conditions are required. For mirror reflectivities R_1 at z=0 and R_2 at z=L the boundary conditions are

$$P^+(0) = R_1 P^-(0)\,, \tag{2.26a}$$

$$P^-(L) = R_2 P^+(L)\,. \tag{2.26b}$$

Integrating the positive-going power in (2.25) from 0 to z and the negative-going power from (L-z) to z gives

$$P^+(z) = P^+(0)e^{gz} + \frac{\gamma_{sp} u_{sp}}{2}\frac{\left(e^{gz}-1\right)}{g}\,, \tag{2.27a}$$

$$P^-(z) = P^-(L)e^{g(L-z)} + \frac{\gamma_{sp} u_{sp}}{2}\frac{\left(e^{g(L-z)}-1\right)}{g}\,. \tag{2.27b}$$

In the form shown in (2.27), it is easy to see the first term as a pure amplification term resulting in an exponential increase in power progressing along the cavity from the facet, and the second term as an amplified spontaneous emission term. Solving for z=0 and z=L,

$$P^+(L) = GP^+(0) + \frac{\gamma_{sp} u_{sp}}{2}\frac{(G-1)}{g}\,, \tag{2.28a}$$

$$P^-(0) = GP^-(L) + \frac{\gamma_{sp} u_{sp}}{2}\frac{(G-1)}{g}\,, \tag{2.28b}$$

where $G = e^{gL}$ is the single pass gain as defined in section 2.2. Combining (2.28) and (2.26), the power at the facets in both directions is found to be

$$P^+(0) = R_1\frac{\gamma_{sp} u_{sp}}{2}\frac{(G-1)(R_2G+1)}{g\left(1-R_1R_2G^2\right)}\,, \tag{2.29a}$$

$$P^+(L) = \frac{\gamma_{sp} u_{sp}}{2}\frac{(G-1)(R_1G+1)}{g\left(1-R_1R_2G^2\right)}\,, \tag{2.29b}$$

$$P^-(0) = \frac{\gamma_{sp} u_{sp}}{2}\frac{(G-1)(R_2G+1)}{g\left(1-R_1R_2G^2\right)}\,, \tag{2.29c}$$

$$P^+(L) = R_2\frac{\gamma_{sp} u_{sp}}{2}\frac{(G-1)(R_1G+1)}{g\left(1-R_1R_2G^2\right)}\,, \tag{2.29d}$$

which can be used with (2.27) to provide an explicit description for the power distribution

along the cavity,

$$P^{+}(z) = \frac{\gamma_{sp} u_{sp}}{2} \frac{\left[1 - R_1 + (1 - R_2) R_1 G\right] e^{gz} + R_1 R_2 G^2 - 1}{g\left(1 - R_1 R_2 G^2\right)} . \qquad (2.30)$$

Equation (2.30) is exactly the same as (2.18) for the cavity modes obtained from the tracing the optical field. Therefore, not only is the total energy conserved but the energy in each cavity mode is also separately conserved. This remarkable fact has been previously demonstrated classically using a current element equivalent to represent spontaneous emission and solving the resulting inhomogeneous Maxwell's equations [12], as well as a transmission line equivalent circuit method [3].

2.4 SINGLE-MODE POWER

In this section, some of the properties of the power integrated over a single mode are discussed. For simplicity, the $z = L$ facet will be considered when examining the output power and the mirror reflectivities are set to $R_1 = R_2 = R$. The extension to opposing facet power, general R, and multimode is straightforward.

The single-mode power, P_m, emitted outside the facet at $z > L$ will simply be the power at the inside of the facet times the transmittivity ($T = 1 - R$) of the facet. From (2.29d),

$$\begin{aligned} P_m &= (1 - R) P_m^{+}(L) \\ &= \frac{\gamma_{sp,m} u_{sp,m}}{2} \frac{(1 - R)(G_m - 1)}{g_m (1 - R G_m)} . \end{aligned} \qquad (2.31)$$

There are several interesting aspects of the simple expression given by (2.31). First, it can be seen that the spontaneous emission coupled into the mode is a factor, so that if there is no spontaneous emission, no power can be emitted. This may seem to be a simple and obvious fact, but there are treatments of lasers for which this is not the case. Second, after a quick inspection it might be concluded that (2.31) is singular at the

transparency condition, $g_m = 0$, since g_m appears in the denominator. However, $G_m - 1$ also approaches zero on the same order. L'Hôpital's rule can be applied to show

$$P_m(g_m = 0) = \frac{\gamma_{sp,m} u_{sp,m}}{2} L$$

which makes sense intuitively. When the gain is such that the material is perfectly transparent to the mode, spontaneous emission is the only source of power in the mode. Since energy has to be conserved and the cavity is in steady state, the rate of energy leaving the facets must be equal to the energy being produced. Half the spontaneous emission must be leaving by each facet.

Finally, there is a real singularity, referred to as the high-gain limit [13], at the point where the round trip gain, RG_m, is unity. The term "threshold" is sometimes used instead of high-gain limit, but here threshold will be reserved for describing the knee in the light *vs.* current curve separating lasing and non-lasing regimes. Usually there is little point in discriminating between the two, since either a model is being used which neglects to properly account for spontaneous emission, which means threshold and high-gain limit are identical, or it is assumed that the difference is negligible. Nevertheless, to avoid confusion and minimize assumptions, a distinction will be drawn herein.

The high-gain limit can be understood by realizing that a unity round-trip gain means that the optical power lost from the cavity (either through the facets or non-axially) is totally compensated for by the gain of the medium. However, spontaneous emission is still pumping energy into the optical mode. The resulting steady-state modal power is infinite. Figure 2.5 shows the asymptotic approach of the output power to the high-gain limit as a function of $g_m L$. In steady state, the high gain limit can never be reached or surpassed. Dynamically, of course, it is possible. The output power in Fig. 2.5 has been normalized to unity at transparency.

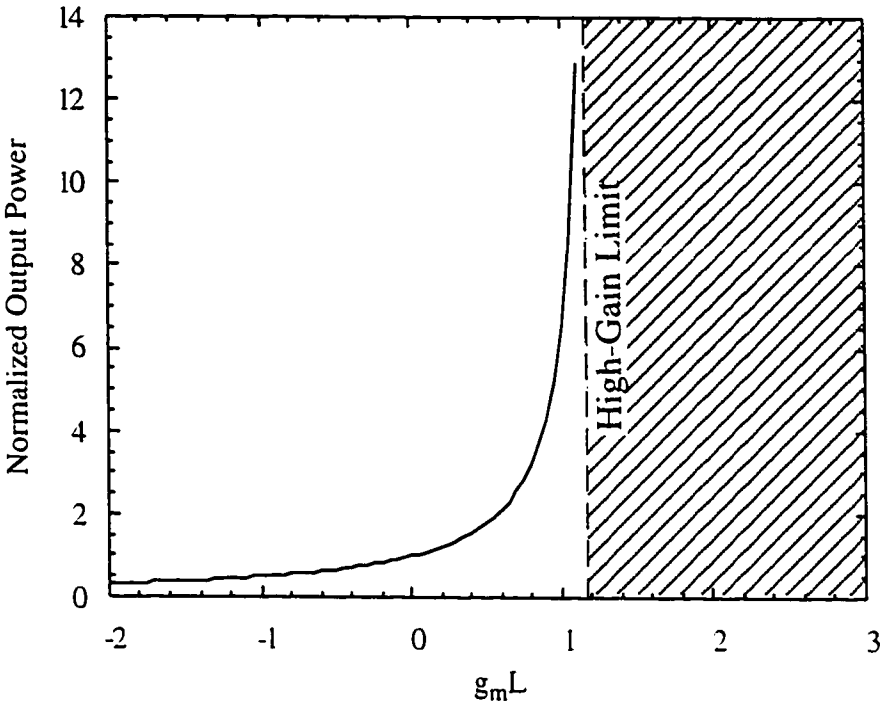

Figure 2.5 - Output power as a function of g_mL, illustrating the high-gain limit and the statically forbidden regime. $R = 0.3$ has been used giving a high-gain limit of $g_mL = \ln(1/0.3)$ and the power has been normalized to unity at $g_mL = 0$.

Inside the cavity, (2.30) can also be simplified for $R_1 = R_2 = R$ to give

$$P_m^+(z) = \frac{\gamma_{sp,m} u_{sp,m}}{2g_m}\left[\frac{(1-R)e^{g_m z}}{1-RG_m} - 1\right] \tag{2.32a}$$

and for the negative-going direction

$$P_m^-(z) = \frac{\gamma_{sp,m} u_{sp,m}}{2g_m}\left[\frac{(1-R)e^{g_m (L-z)}}{1-RG_m} - 1\right] \tag{2.32b}$$

and at transparency

$$P_m^+(z; g_m = 0) = \frac{\gamma_{sp,m} u_{sp,m}}{2}\left(z + \frac{R}{1-R}L\right). \tag{2.33a}$$

$$P_m^-(z; g_m = 0) = \frac{\gamma_{sp,m} u_{sp,m}}{2}\left(\frac{1}{1-R}L - z\right). \tag{2.33b}$$

Equations (2.32) and (2.33) are plotted as a function of position in the cavity for various values of the gain in Figure 2.6. Above transparency, the power increases exponentially as the optical wave travels along the length of the cavity. At transparency, the increase is linear and under lossy conditions the power increases as a constant minus a negative exponential. When the optical wave reaches a facet, a fraction, (1-R), of the energy is dumped from the cavity. The remainder of the wave is reflected and propagates in the opposite direction, increasing exponentially. When the wave reflects again from the other facet and reaches the starting position, it is the same power as it was originally.

The total power distribution (the sum of both the positive- and negative- going waves) is not uniform; for $g_m > 0$, it will be a maximum at the mirrors and a minimum in the centre. A large power difference between two sections of the waveguide can possibly lead to such highly differing local rates of stimulated recombination that a significant

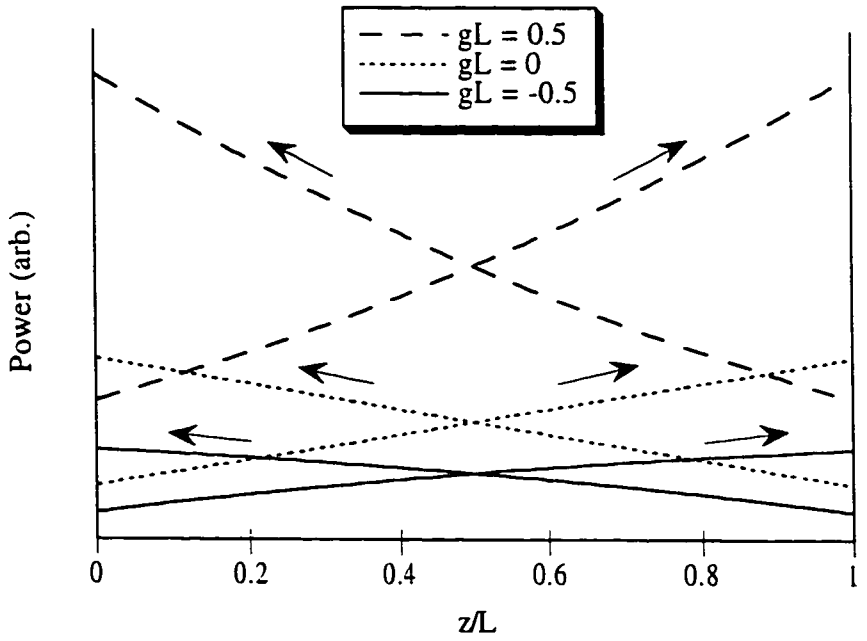

Figure 2.6 - Power distribution as a function of position for various values of the gain-length product. Arrows indicate the direction of propagation.

difference in the carrier populations is induced. The assumption that the gain and spontaneous emission are constant along the length of the cavity would then break down.

The ratio of total power between the middle of the cavity (at $P_m(L/2) = P_m^+(L/2) + P_m^-(L/2)$) and the end of the cavity ($P_m(L) = P_m^+(L) + P_m^-(L)$) is approximately constant near the high gain limit and can be calculated. Forming the ratio using (2.31) and taking the limit as $RG \to 1$ ($\Rightarrow g \to \ln(1/R)/L$) gives

$$\lim_{RG \to 1} \{P_m(L/2)/P_m(L)\} = \frac{2\sqrt{R}}{1+R} \tag{2.34}$$

which is about 0.84 for R = 0.3. Although the relative difference does not seem overly large, a high power density could mean a large absolute difference. This would result in a reduced differential electrical-to-optical conversion efficiency and a roll-off in the L-I curve. Analyses in this thesis are restricted to the sub-roll-off regime. Note (2.34) indicates that increasing the facet reflectivity (for example, by coating the facets with a highly reflective dielectric stack) would delay the onset of this effect.

2.5 Power Spectral Density

The power spectral density given by (2.17) can be illustrated graphically. As an example, the gain as a function of wavelength was measured on a 7 quantum well, L = 250 μm laser (see chapter 5). It was found that the dependence of the gain on mode number m (where m = 0 is the peak of the gain curve) could be well described by a parabola over a limited range of wavelengths and currents:

$$g_m \approx g_0\left(1 + 0.010m - 0.0025m^2\right) \tag{2.35}$$

where g_0 is the peak gain.

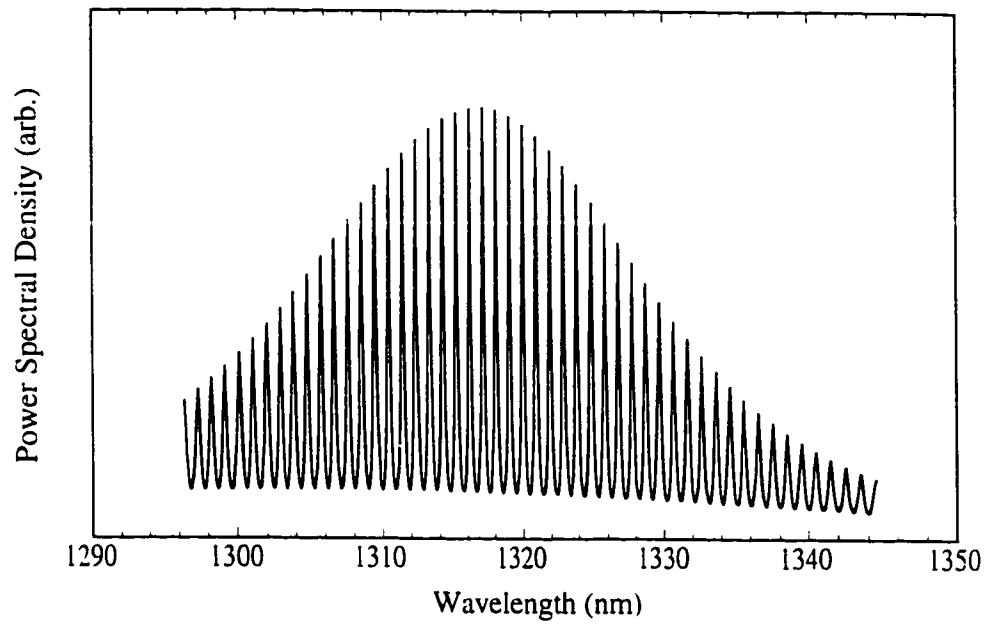

Figure 2.7 - Calculated power spectral density from the laser facet for $RG_0 = 0.5$ and $L = 250\ \mu m$ ($g_0 = \ln(0.5 / R) / 0.0250\ cm^{-1}$ and $R = 0.3$).

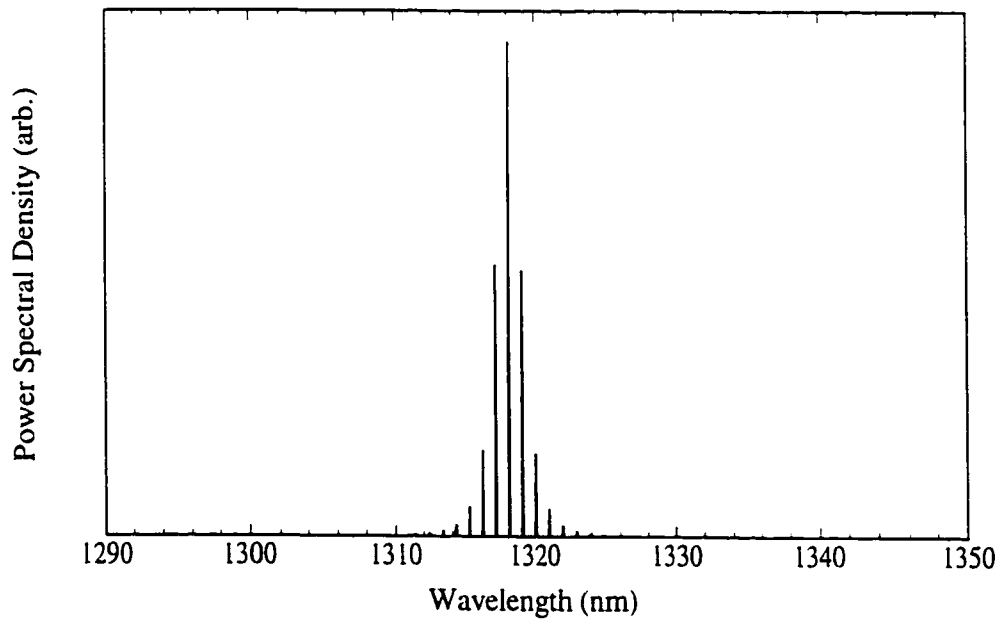

Figure 2.8 - Calculated power spectral density under high gain conditions, $RG_0 = 0.98$ ($g_0 = \ln(0.98 / R) / 0.0250\ cm^{-1}$ and $R = 0.3$).

It is also necessary to obtain an approximate curve for the spontaneous emission. To do this, the magnitudes of the spectral peaks (ν / ν_{FSR} = integer) were calculated using (2.35) and (2.17) with $R = 0.3$, and $\gamma_{sp,m} u_{sp,m}$ set to unity. The experimentally measured spectral peaks were then divided by the calculated peaks. The result is a function proportional to $\gamma_{sp,m} u_{sp,m}$. Assuming $\gamma_{sp,m}$ is a weak function of m, it is found that the spontaneous emission power per unit length per mode is approximately described by a linear function of m:

$$u_{sp,m} \approx u_{sp,0}(1 + 0.012m). \tag{2.36}$$

The power spectral density is plotted as a function of frequency in Figure 2.7 for a low gain value of $RG_0 = 0.5$. As the gain increases, small differences in the gain between adjacent modes make a larger difference in the spectrum. As the peak gain approaches the high gain limit, the central mode begins to dominate, as can be seen in Figure 2.8 with $RG_0 = 0.98$.

Although, in principle, the mode at the peak of the gain curve should always lase, crystal defects within the cavity can cause small amounts of feedback due to Rayleigh scattering [14]. This can cause a departure from the idealized spectra in Figure 2.7 and Figure 2.8.

2.6 Carriers and Current

Under CW conditions, the laser is usually driven by a constant current source. The current flow is caused by a voltage drop across the laser and results in electrons being promoted from the valence band to the conduction band. The usual strategy, which is followed here, is to use the carrier density as a kernel quantity and calculate both the gain and current from it. Once that is done, the output power can be calculated using the equations derived in the previous sections and the light output *vs.* current characteristic can

be obtained.

In 1986, McIlroy *et. al.* [15] noticed that the calculated gain (at the peak of the gain *vs.* wavelength curve) for a quantum well laser had a carrier density dependence which was approximately logarithmic above transparency. In Chapter 5, an example of such a calculation will be given and it will be shown that the net peak material gain (that is, at mode m=0) for transitions across the bandgap, B_0, can be described by

$$B_0 = \beta_0 \ln(n / n_0) \tag{2.37}$$

where β_0 and n_0 are the parameters which give the best fit to the numerical calculation. The symbol "n" is used to refer to the carrier density. For charge neutral, intrinsically doped wells, the excess electron and hole populations will be equal. This assumption is often used in the literature to avoid detailed calculations of carrier distributions in the active region. It is adopted here with the caveat that non-uniform densities from well to well is a potential source of inaccuracy.

Among the optical loss mechanisms, inter-valence band absorption (IVBA) plays a large role as will be discussed in detail in Chapter 3. IVBA is considered to be approximately proportional to the hole density [16]-[18] in the quantum wells:

$$\alpha_{IVBA,0} = \gamma n . \tag{2.38}$$

Optical power will also be scattered from the waveguide from defects both in the core and the cladding of the waveguide. These are labeled with the single, carrier-independent loss coefficient α_0. Putting the above terms together, the peak net modal gain can be written

$$g_0 = \Gamma\beta_0 \ln(n / n_0) - \Gamma\gamma n - \alpha_0 . \tag{2.39}$$

Calculating the current from the carrier density (or any other quantity e. g. voltage) is a difficult task. There are many mechanisms responsible for current flow in a laser, including radiative recombination, non-radiative recombination through localized bandgap

states, current leakage laterally outside the ridge, leakage over the p-i-n heterobarrier, and Auger recombination. To incorporate a full treatment of any one of these is complicated and would introduce large uncertainties in terms of unknown or poorly known material parameters. Furthermore, there still remains much controversy over the relative influence of these mechanisms.

The carrier density is usually related phenomenologically to the rate of recombination per unit volume, r, by [6]

$$r = an + bn^2 + cn^3 \tag{2.40}$$

where each term is associated with a separate mechanism: the first with non-radiative recombination; the second with radiative recombination; and the final with Auger recombination. However, there is no clear experimental confirmation that the different current mechanisms can be so easily separated and (2.40) is nothing more than a three parameter polynomial fit to the r *vs.* n data. In fact, there is direct experimental evidence to the contrary [19]. Spontaneous emission from the laser has been observed to increase linearly with carrier density, indicating that it is more closely related to the first term to than to the second. In addition, theoretical calculations show that carrier degeneracy, and phonon- and trap-assisted processes tend to change the power law dependence of the Auger recombination rate [20].

In Chapters 4 and 5, different approximations to (2.40) will be used for convenience. For the purposes of calculating the L-I curve in the next section, the following approach is used. Both the spontaneous emission and non-radiative recombination rate are assumed proportional to n. The stimulated recombination rate is calculated using the optical power equations and dividing by the hν of each mode to convert the power to a quantum rate. The contribution of Auger recombination is ignored. Finally, it was discovered that, although the above assumptions are adequate to describe the

magnitude of the above-threshold slope of the L-I curve for a variety of lengths, well numbers and temperatures (see Chapter 3) and to partially predict the relative change of threshold with length, well number and temperature (see Chapter 4), a length-independent contribution to the threshold current is required to account for changes in the gain with cavity length. This is examined further in Chapter 5, with possible sources being non-uniform carrier injection into the quantum wells and changes in lateral leakage current. For the purposes of this chapter, the length independent current is left as an adjustable parameter, I_b=qtbn, where q is the electron charge, t is the active area thickness and b is the carrier proportionality constant.

2.7 THE L-I CURVE

In this section the light output *vs.* current (L-I) characteristic of a free running semiconductor laser will be reproduced. It is stressed that the following is not being submitted as evidence that the model is an accurate description of the laser, since at this point no quantitative evidence has been offered that the numerous adjustable parameters introduced so far have any physical significance. The purpose of this section is merely to show that L-I curves with appropriate shapes, threshold currents, efficiencies, and output powers can be calculated. The real test of a theory lies in the ability to describe changes in the L-I curve under different design and operating conditions, as will be done in later chapters.

From Section 2.6, the current density passing through the laser contact, J, can be written as a function of carrier density given by

$$J = qt\left(a_{sp}n + a_{nr}n + bn/(wL) + \bar{r}_{st}\right) \tag{2.41}$$

where a_{sp} and a_{nr} are the coefficients of the spontaneous emission and non-radiative recombination rates, respectively, $\bar{r}_{st}$ is the average rate of stimulated recombination per

unit volume, b is the constant for the length-independent current discussed in Section 2.6, q is the electron charge, w is the ridge width, and L is the cavity length as before.

The parameter a_{sp}, once chosen, can be related to peak of the spontaneous emission curve at any carrier density. The spontaneous emission power of each mode is converted to a quantum rate by dividing (2.36) by the quantum energy of the mode, $h\nu_m$. This rate is then summed over all significant modes and divided by the lateral width and transverse thickness of the active region, to give the quantum rate per unit volume, which is equal to $a_{sp}n$. In equation form,

$$u_{sp,0} = \frac{a_{sp} nwt}{\sum_{m=-M}^{M} (1 + 0.012m) / h\nu_m} . \tag{2.42}$$

The range of modes that contribute significantly the total emission rate is given by M.

The parameter $\bar{r}_{st}$ can be calculated by integrating the modal stimulated emission power per unit length in both directions over the length of the cavity, dividing by the photon energy of the mode, summing over all modes, and finally dividing by L to get the average:

$$\bar{r}_{st} = \frac{1}{L} \sum_{m=-M}^{M} \frac{1}{h\nu_m} \left\{ \int_0^L B_m P_m^+(z) dz + \int_L^0 B_m P_m^-(z) dz \right\}. \tag{2.43}$$

For the power distribution with equal facet reflectivities given by (2.31), (2.43) becomes

$$\begin{aligned} \bar{r}_{st} &= \frac{2}{L} \sum_{m=-M}^{M} \frac{1}{h\nu_m} \int_0^L B_m P_m^+(z) dz \\ &= \frac{2}{L} \sum_{m=-M}^{M} \frac{1}{h\nu_m} \left[P_m - \frac{\gamma_{sp} u_{sp,m} L}{2} \right] \frac{B_m}{g_m} \end{aligned} \tag{2.44}$$

where P_m is the output power of the m^{th} mode given by (2.31). There is an assumption required in applying (2.44). Although the relationship between B_0 and g_0 is known from

(2.39) if $\alpha_{IVBA,0}$ and α_0 are known, this is not true for other values of m. A spectrum for the *net* gain is given by (2.35), but this is the result of combined spectra of B_m and $\alpha_{IVBA,m}$; neither is known individually. In later chapters, this will not be a problem since either g_m or B_0 will be the quantities of concern. For the purposes of this section and the sake of simplicity, however, it will be assumed that B_m , $\alpha_{IVBA,m}$, and $\alpha_{0,m}$ all have the same spectrum given by (2.35). The result of this assumption is that the spectral information in the ratio B_m / g_m cancels, and (2.43) can be written

$$\bar{r}_{st} = \frac{2B_0}{g_0 L} \sum_{m=-M}^{M} \frac{1}{h\nu_m} \left[P_m - \frac{\gamma_{sp} u_{sp,m} L}{2} \right] . \qquad (2.45)$$

Under high loss conditions (both B_0 and g_0 negative and $P_m < \gamma_{sp} u_{sp} L / 2$), $\bar{r}_{st}$ can become negative. In this situation, $|\bar{r}_{st}|$ is the rate of *absorption* transitions across the bandgap.

We are now in a position to illustrate the light output and gain as a function of current. The method is as follows:

1. Step the carrier density to the next value, or choose a start value if this is the first iteration.
2. Calculate the associated peak net gain using (2.39), and determine the net gain and spontaneous emission for the remainder of the modes using (2.35), (2.36) and (2.42).
3. Calculate the single facet output power for each of the modes using (2.31) and the total output power by the sum over all modes.
4. Calculate the current density using (2.45) and (2.41). The current can be obtained by multiplying J by wL.
5. Repeat the above steps as necessary.

For convenience, the equations used in the above algorithm are summarized with the corresponding step number.

1. Choose n

2. $$g_0 = \Gamma\beta \ln(n / n_0) - \Gamma\gamma n - \alpha_0 \qquad (2.39)$$

$$g_m \approx g_0\left(1 + 0.010m - 0.0025m^2\right) \qquad (2.35)$$

$$u_{sp,0} = \frac{a_{sp} nwt}{\sum_{m=-M}^{M} (1 + 0.012m) / hv_m} \qquad (2.42)$$

$$u_{sp,m} \approx u_{sp,0}(1 + 0.012m) \qquad (2.36)$$

3. $$P_m = \frac{\gamma_{sp,m} u_{sp,m}}{2} \frac{(1-R)(G_m - 1)}{g_m(1 - RG_m)} \qquad (2.31)$$

$$P_{out} = \sum_{m=-M}^{M} P_m$$

4. $$\bar{r}_{st} = \frac{2B_0}{g_0 L} \sum_{m=-M}^{M} \frac{1}{hv_m}\left[P_m - \frac{\gamma_{sp} u_{sp,m} L}{2}\right] \qquad (2.45)$$

$$J = qt\left(a_{sp} n + a_{nr} n + bn / (wL) + \bar{r}_{st}\right) \qquad (2.41)$$

The adjustable input parameters are β, γ, n_0, α_0, γ_{sp}, a_{sp}, a_{nr} and b, and the design parameters are Γ, L, t and w. Even for this simple model there is a large number of parameters (eight) which can be adjusted to give agreement with experimental results. It is for this reason that the following is considered a numerical example for illustration only. L-I curves with appropriate thresholds, efficiencies, output powers, and associated properties such as gain saturation can be reproduced for reasonable values of the input parameters. Models are often put forward which agree with experiment remarkably well, but little discussion of the number input parameters or corresponding confidence intervals is offered. This is usually because the output of the model is sensitive enough to the input

parameters that nearly any experimental result can be explained by judiciously altering the values. In such cases taking the match between experiment and theory as verification of the theory is highly suspect. In later chapters, specific aspects of the model are used to characterize lasers and frank discussions of confidence intervals and degrees of freedom are given.

L-I curves produced by the model for a 7 quantum well device are shown in Fig. 2.9. The input parameters were kept constant, except for the length, and are summarized in Table 2.2. Sources for comparison of the values used are included in the Table. All parameters are within reasonable proximity of published experimental values. Also shown in Figure 2.9 are experimentally measured L-I curves for devices with the same cavity lengths and well number. It can be seen that, once the input parameters are fixed, the variation in the threshold current and above-threshold efficiency are faithfully reproduced.

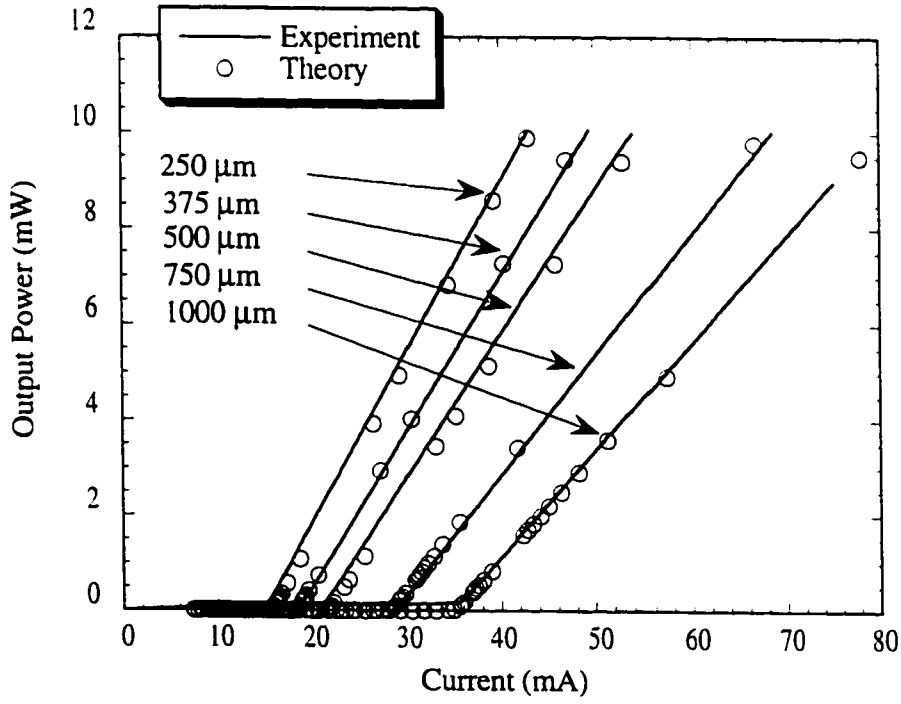

Figure 2.9 - Experimental and theoretical L-I curves for a seven quantum well laser at 20°C. The theoretical points above threshold have a non-constant spacing because of the computer algorithm used to search for valid points near the high gain limit.

Parameter	Value	Units	Comments
β_0	8904	cm^{-1}	measured directly; see chapter 3
γn_{tr}	333	cm^{-1}	measured directly; see chapter 3
α_0	1.6	cm^{-1}	measured directly; see chapter 3
n_{tr}	$2x10^{18}$	cm^{-3}	measured value of $2.5x10^{18}$ in [16]
a_{sp}	10^9	s^{-1}	combined sp and nr value of $5x10^8$ in [19]
a_{nr}	$6.5x10^8$	s^{-1}	see above
b	8000	cm^2s^{-1}	see section 2.6 for discussion
γ_{sp}	$2x10^{-3}$	natural	values range from 10^{-4} to 10^{-2}; see for example [2]
Γ	0.0336	natural	calculated; see chapter 3
t	7x3.5=24.5	nm	physical value of device used for experiment
w	2	μm	physical value of device used for experiment

Table 2.2 - Values of input parameters used in producing the theoretical L-I curves in Fig. 2.9.

2.8 GAIN SATURATION

When the laser is above threshold, the modal gain is close to the high gain limit in Fig. 2.5; i. e.,

$$g = \ln(1/R)/L - \delta$$

where δ is small. The increase in output power is driven by a decrease in δ. Since the change in carrier density required to produce these changes is also small, all carrier-density-dependent processes in the wells such as spontaneous emission and non-radiative recombination are essentially clamped at the threshold value. Due to the high power density in the cavity, carriers that make it into the wells are immediately stimulated to

recombine radiatively and do not contribute to an increase in the gain. Thus, as the current density increases above threshold, the gain *vs.* current density curve saturates and becomes constant, as depicted in Fig. 2.10 for a 7 quantum well, 500 μm device calculated using the model in Section 2.7.

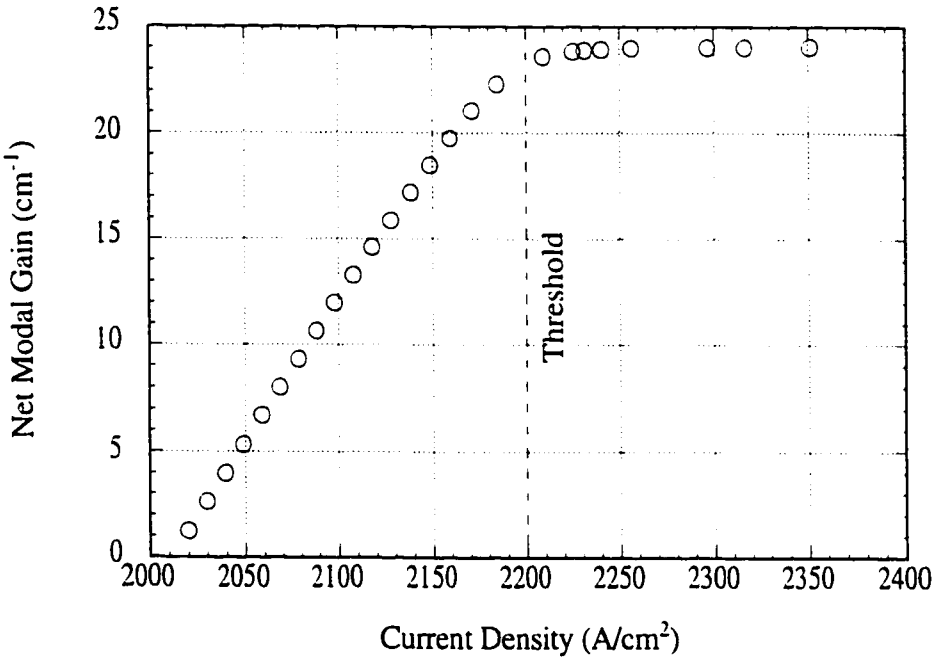

Figure 2.10 - Net modal gain as a function of current density for a 7 well, 500 μm device, as calculated from the model in Section 2.7. The gain curve saturates at the threshold current density.

2.9 THE ABOVE-THRESHOLD SPECTRAL LINE

In Section 2.2, it was found that the finesse of the laser cavity is determined by the product of the reflectivity and single-pass gain. The coefficient of finesse, $\Im$, is given by

$$\Im = \frac{4RG}{1-RG}$$

where $R = \sqrt{R_1 R_2}$. When RG is close to unity, as is the case above threshold, the finesse

is very high. In this section, the spectrum of a single mode near the high-gain limit is investigated.

The output spectrum of a laser was found to be

$$P_{out}(\nu) = \frac{\gamma_{sp} u_{sp}(\nu)(1-R_2)(G(\nu)-1)(1+R_1 G(\nu))}{2g(\nu)\left[(1-RG(\nu))^2 + 4RG(\nu)\sin^2(\pi\nu/\nu_{FSR})\right]} . \qquad (2.17)$$

Let ν_0 be the centre of lasing resonance m (i. e. - $\nu_0 / \nu_{FSR} = m$). For frequencies near this resonance, $\sin(\pi(\nu-\nu_0)/\nu_{FSR}) \approx \pi(\nu-\nu_0)/\nu_{FSR}$ and (2.17) becomes

$$P_{out}(\nu) \approx \frac{\gamma_{sp} u_{sp,m}(1-R_2)(G_m-1)(1+R_1 G_m)}{2g_m(1-RG_m)^2\left[1+\frac{4RG_m\pi^2}{(1-RG_m)^2}\frac{(\nu-\nu_0)^2}{\nu_{FSR}^2}\right]} \qquad (2.46)$$

which is a Lorentzian function of frequency with a full width at half maximum (FWHM), $\Delta\nu$, of

$$\Delta\nu = \frac{(1-RG)\nu_{FSR}}{\pi\sqrt{RG}} . \qquad (2.47)$$

Equation (2.47) can be made somewhat more meaningful with the help of a few substitutions. The RG under the radical can be eliminated in the limit as $RG \to 1$. With the help of (2.31), the factor of (1-RG) in the numerator can be solved for in terms of the output power of that mode:

$$(1-RG_m) = \frac{\gamma_{sp} u_{sp,m}}{2}\frac{(1-R_2)(G_m-1)}{g_m P_m} \qquad (2.48)$$

where the facet number 2 (at $z=L$) has been designated as the output facet. Substitution of (2.48) and $\nu_{FSR} = c/2n_g L$ into (2.47) gives

$$\Delta\nu = \frac{\gamma_{sp} u_{sp}(1-R_2)(G_m-1)c}{2\pi g_m n_g L P_m} \qquad (2.49)$$

n_g is the modal group index defined by $n_g = k / k_0$. Since this is the lasing resonance, $g_m \approx \ln(1/R)/L$ and $G_m \approx 1/R$,

$$\Delta\nu = \frac{cK\gamma_{sp}u_{sp}}{2\pi n_g P_m} \tag{2.50}$$

where

$$K \equiv \frac{(1-R_2)\left(1-\sqrt{R_1R_2}\right)}{\sqrt{R_1R_2}\,\ln\left(1/\sqrt{R_1R_2}\right)}\,.$$

Equation (2.50) exhibits the inverse power dependence obtained in other treatments [21]. The derivation given here is very simple. It does not include noise in the centre frequency ν_0 due to refractive index fluctuations, which can act to broaden the linewidth [21].

A number of factors can be modified to reduce the linewidth at a constant output power. Lowering the fraction of spontaneous emission coupled into the mode, γ_{sp}, and reducing $u_{sp,m}$ by lowering the carrier density required to reach threshold are two examples. The threshold carrier density can be lowered by increasing the length of the device, increasing the reflectivity of the facets, or by engineering the band structure to improve the amount of gain at a given carrier density. A further reduction can be realized in the K factor. Figure 2.11 shows a plot of K. For typical as-cleaved facets, the reflectivity is about $R = 0.3$ which gives K = 1.4. If the facets are coated to have a reflectivity of $R = 0.9$, K is reduced to 0.11, which amounts to over a factor of 10 reduction in linewidth. Often, for high power devices, the output facet is left as-cleaved and the other coated for high reflectivity. In this case, a much smaller reduction in linewidth is expected between $R_1 = 0.3$ and $R_1 = 0.9$, as shown in Figure 2.11.

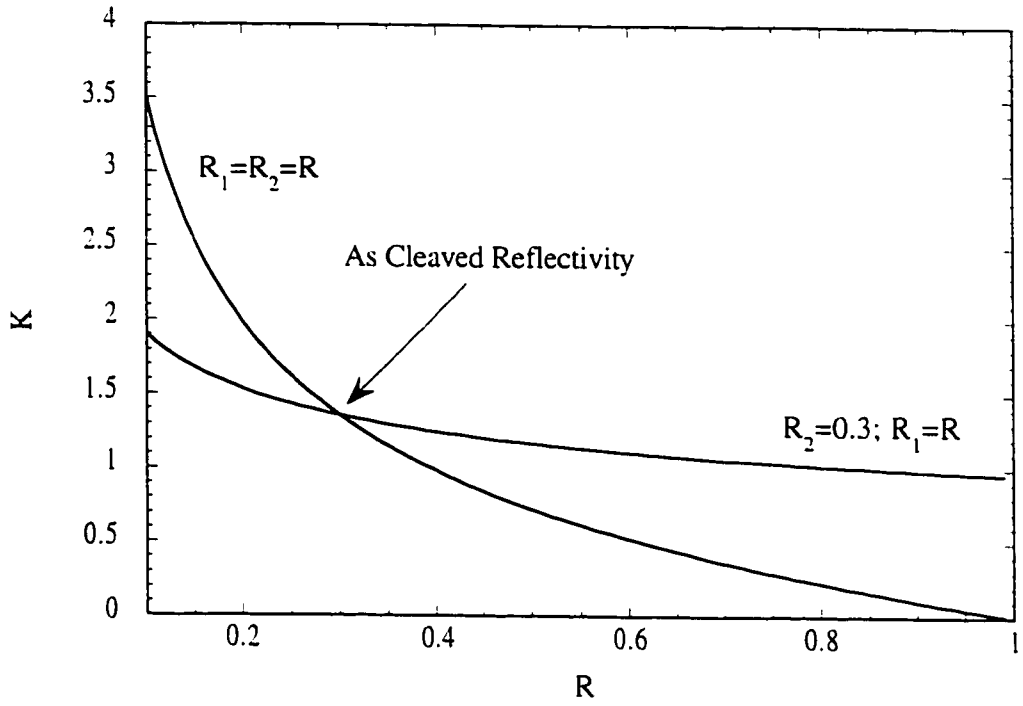

Figure 2.11 - The K factor in (2.49) plotted as a function of reflectivity. One case is for identical facet reflectivities, the other for one facet fixed at the as-cleaved value of 0.3.

REFERENCES

[1] D. T. Cassidy, "Comparison of rate-equation and Fabry-Perot approaches to modeling a diode laser", *Appl. Opt.*, vol. 22, pp. 3321-3326, 1986.

[2] D. T. Cassidy, "Analytic description of a homogeneously broadened injection laser", *IEEE J. Quantum Electron.*, vol. QE-20, pp. 913-918, 1984.

[3] E. I. Gordon, "Optical maser oscillators and noise", *Bell Syst. Tech. J.*, pp. 507-539, Jan. 1964.

[4] J. Swoger, *On Non-uniform Pumping Effects in Semiconductor Lasers*, Ph. D. Thesis, McMaster University, 1997.

[5] S. L. Chuang, *Physics of Optoelectronic Devices*, John Wiley & Sons Inc., 1995.

[6] G. P. Agrawal, N. K. Dutta, *Semiconductor Lasers*, 2nd ed., VanNostrand Reinhold, 1993.

[7] K. S. Chiang, "Analysis of rectangular dielectric waveguides: effective-index method with built-in perturbation correction", *Electron. Lett.*, vol. 28, pp. 388-389, 1992.

[8] G. R. Fowles, *Introduction to Modern Optics*, 2nd ed., Dover Publications, 1968.

[9] S. Haykin, *Introduction to Analog and Digital Communications*, John Wiley & Sons Inc., 1989.

[10] H. Soda, H. Imai, "Analysis of the spectrum behaviour below the threshold in DFB lasers", *IEEE J. Quantum Electron.*, Vol. QE-22, pp. 637-641, 1986.

[11] P. Lorrain, D. P. Corson, F. Lorrain, *Electromagnetic Fields and Waves*, third ed., W. H. Freeman and Company NY, pp. 528-529, 1988.

[12] D. Marcuse, "Classical derivation of the laser rate equation", *IEEE J. Quantum Electron.*, vol. QE-19, pp. 1228-1230, 1983.

[13] A. E. Seigman, *Lasers*, University Science Books, 1986.

[14] F. H. Peters, D. T. Cassidy, "Strain and scattering related spectral output of 1.3-μm InGaAsP semiconductor diode lasers", *Appl. Opt.*, vol. 30, pp. 1036-1041, 1991.

[15] P. W. A. McIlroy, A. Kurobe, Y. Uematsu, "Analysis and application of theoretical gain curves to the design of multi-quantum-well lasers", *IEEE J. Quantum Electron.*, vol. QE-21, pp. 1958-1963, 1985.

[16] D. A. Ackerman, P. A. Morton, G. E. Shtengel, M. S. Hybertsen, R. F. Kazarinov, T. Tanbun-Ek, R. A. Logan, "Analysis of To in 1.3 μm multi-quantum-well and bulk active lasers", *Appl. Phys. Lett.*, vol. 66, pp. 2613-2615, 1995.

[17] M. Asada, A. Kameyama, Y. Suematsu, "Gain and intervalence band absorption in quantum-well lasers", *IEEE J. Quantum Electron.*, vol. QE-20, pp. 745-753,. 1984.

[18] G. Fuchs, J. Horer, A. Hangleiter, V. Harle, F. Scholz, "Intervalence band absorption in strained and unstrained InGaAs multiple quantum well structures", *Appl. Phys. Lett.*, vol. 60, pp. 231-233, 1992.

[19] Y. Zou, J. S. Osinski, P. Grodzinski, P. D. Dapkus, W. C. Rideout, W. F. Sharfin, J. Schlafer, F. D. Crawford, "Experimental study of Auger recombination, gain, and temperature sensitivity of 1.5 μm compressively strained semiconductor lasers", *IEEE J. Quantum Electron.*, Vol. 29, pp. 1565-1575, 1993.

[20] P. T. Landsberg, "The band-band Auger effect in semiconductors", *Solid State Electron.*, vol. 30, pp. 1107-1115, 1987.

[21] C. H. Henry, "Theory of the linewidth of semiconductor lasers", *IEEE J. Quantum Electron.*, vol. QE-18, pp. 259-264, 1982.

CHAPTER THREE

QUANTUM EFFICIENCY AND OPTICAL LOSS[†]

3.0 INTRODUCTION

THE slope of the L-I curve above threshold is of interest from a practical standpoint since an increase in this slope means a higher output power can be obtained for a lower rate of current flow. This is especially important in applications where CW operation with a minimum of current consumption is desired, such as high-power externally modulated sources for use as transmitters in optical fibre communications systems. Measuring the slope as a function of length can be used to obtain the optical losses, and, as will be seen, the variations in the slope as a function of well number provides further insight into the gain and inter-valence band absorption.

It is convenient to introduce a unitless quantity to represent the slope. The differential quantum efficiency, η_d, (also sometimes called the external quantum efficiency), is defined as

---

[†]The majority of this chapter has been published in [1]

$$\eta_d = \frac{2q}{h\nu}\frac{dP}{dI} \tag{3.1}$$

where P is the power output of one facet, I is the input current, and $h\nu$ is the photon energy in the lasing mode. The factor of 2 is included to account for light leaving both facets. The cavity is assumed symmetric.

In Section 3.1, an expression for η_d is derived from the power equations of Chapter 2. The remainder of this chapter is dedicated to a large-scale study of multi-quantum well lasers, where the number of wells, length, and temperature are systematically altered. Section 3.2 contains a description of the devices and the experimental apparatus used to measure the L-I characteristics. A detailed analysis of the results is given in Section 3.3, and a discussion of the results is provided in Section 3.4.

3.1 Differential Quantum Efficiency

It is useful for characterization purposes to derive a formula for η_d in terms of the internal quantum efficiency, η_i, which is defined as

$$\eta_i = \frac{2q}{h\nu}\frac{dP_{in}}{dI} \tag{3.2}$$

where P_{in} is the power traveling in one direction produced inside the cavity by the lasing mode. The maximum possible value of η_i is unity, which means that as the rate of carrier injection is increased, the rate of photon production increases by the same amount. Because the carrier density is clamped above threshold, spontaneous emission from the cavity and non-radiative processes do not contribute directly to η_i (they would, of course, contribute if η_i were defined as proportional to P_{in} / I instead of being a differential quantity). Stimulated emission is considered to be coupled into the cavity with approximately 100% efficiency [2]. Therefore, the only contribution to a non-unity η_i is leakage around the active area, either laterally outside the ridge or transversally, without

being captured by the quantum wells.

From (3.1) and (3.2)

$$\eta_d = \eta_i \frac{dP / dg}{dP_{in} / dg} \tag{3.3}$$

where g is the net modal gain.

The power produced inside the cavity will be the sum of the contributions from stimulated and spontaneous emission along the length of the cavity,

$$P_{in} = \int_0^L \left[BP^+(z) + \frac{\gamma_{sp} u_{sp}}{2} \right] dz \tag{3.4}$$

where $P^+(z)$ is given by (2.32a), B is the modal gain (excluding losses), and $\gamma_{sp} u_{sp} / 2$ is the spontaneous emission in one direction coupled into the mode, as defined in Chapter 2. The mode number subscript, m, has been dropped from the notation. It is recognized that only the lasing mode is being considered since the non-lasing modes should be essentially clamped by the constant carrier density. Performing the integration in (3.4) gives

$$P_{in} = \frac{B}{g} P + \frac{\gamma_{sp} u_{sp} L}{2} \left[1 - \frac{B}{g} \right] \tag{3.5}$$

where (2.31) has been used to identify P. The fact that the spontaneous emission and the gain are only changing by small amounts above threshold is used to note that

$$\frac{dP}{dg} >> \frac{d}{dg}\left[\frac{B}{g}\right],$$
$$\frac{dP}{dg} >> \frac{d\gamma_{sp} u_{sp}}{dg},$$

so that the derivative of (3.5) becomes

$$\frac{dP_{in}}{dg} = \frac{B}{g}\frac{dP}{dg} \tag{3.6}$$

which, upon substitution into (3.3) yields

$$\eta_d = \eta_i \frac{g}{B}. \tag{3.7}$$

Since $B = g + \alpha$, where α is the loss coefficient as discussed in Chapter 2, and g can now be approximated by the high gain value of $g = \ln(1/R)/L$, the end result of this section can be written by inverting (3.7),

$$\eta_d^{-1} = \eta_i^{-1}\left[1 + \frac{\alpha L}{\ln(1/R)}\right]. \tag{3.8}$$

Equation (3.8) will be used in the analysis that follows.

3.2 EXPERIMENT

Variations in η_d with thickness and composition of the graded-index region surrounding the active region have been observed in a variety of devices [3]-[5]. An anomalous length dependence of η_d^{-1} containing a minimum that shifts with well number in MQW lasers [6], [7] and with active volume in bulk double heterostructure lasers [8] has been attributed to inter-valence band absorption (IVBA) in the barrier regions in the former case [7], while the latter has been analyzed using a detailed numerical model including several mechanisms such as Auger recombination, leakage over the heterobarrier, free carrier absorption, and radiative recombination in the guiding layers [9]. The temperature dependence of η_d has similarly been modeled and attributed to increased thermal broadening of the gain spectrum due to changes in the momentum relaxation rate [10].

In this and the remaining sections, a systematic empirical investigation of the length, well number, and temperature dependence of η_d in strained InGaAsP/InP MQW lasers operating at 1.3 μm is presented. The devices studied in this investigation are multiquantum well (MQW) ridge waveguide lasers operating at 1.3 μm with the flat-band

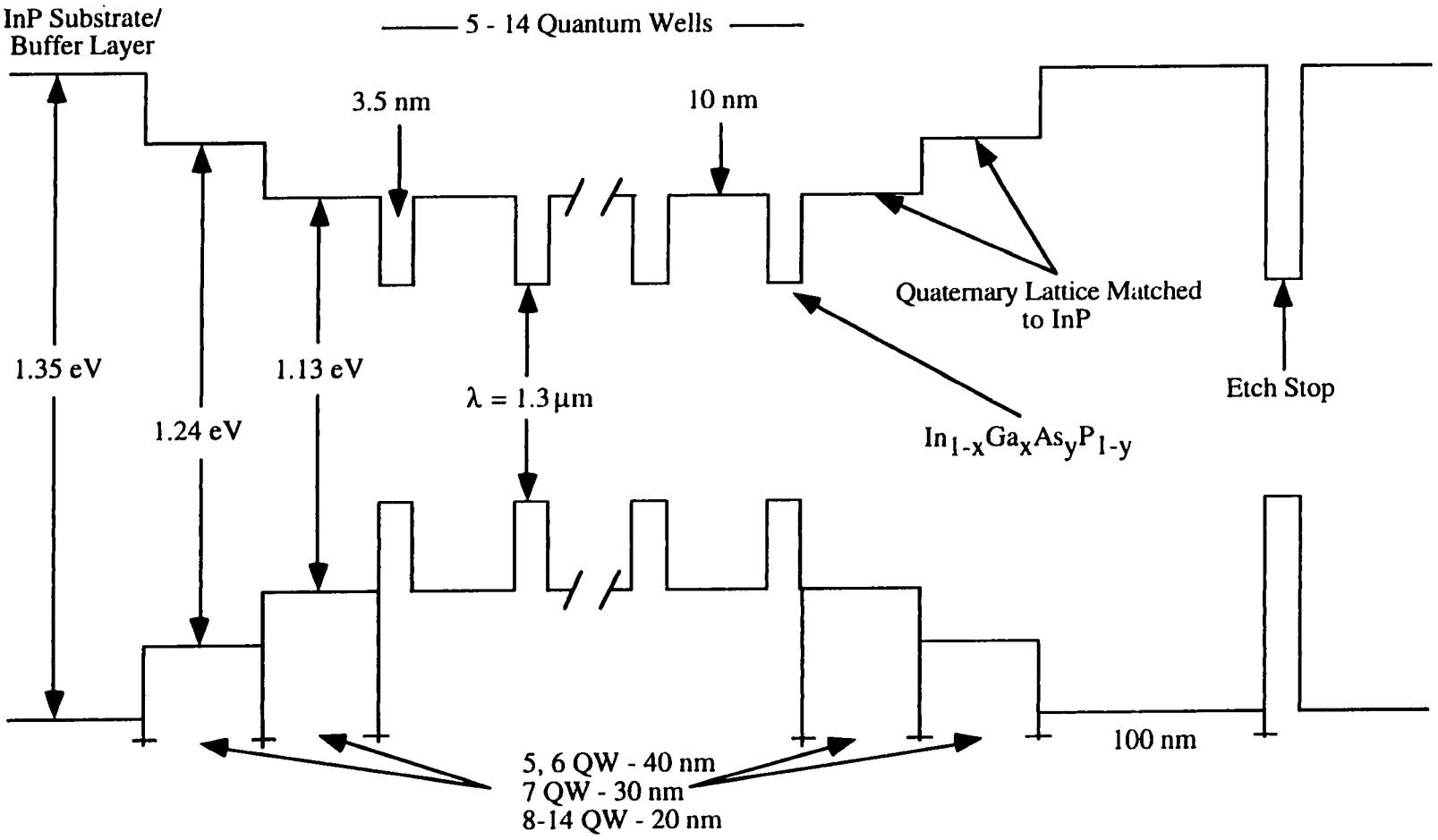

Figure 3.1 - Schematic diagram of the band structure of the lasers used for this study.

structure in the transverse direction given in Fig. 3.1. The wells were 0.7% compressively strained and contained in a stepped separate confinement heterostructure (SSCH). Seven structures were grown by low-pressure metalorganic vapor phase epitaxy (LP-MOVPE) on (100) oriented S-doped n-type InP substrates with well numbers ranging from 5 to 14. The SSCH region was varied in width from 80 to 40 nm on the n and p sides to maintain a more constant total core region width. Lasers were processed with 2 μm ridges, cleaved to five lengths of 250 μm to 1000 μm, and mounted on SiC/copper block heat sinks which in turn were mounted on alumina substrates. An average of five devices at each length and well number were prepared so that devices with outlying characteristics could be reasonably discarded, which accounted for about 20% of the 175 laser set. Figure 3.2 is a summary of the lasers in the set.

CW L-I measurements were made on all device structures with heat sink temperatures ranging from -50 to 90°C. Careful calibration of the photodetector was required for accurate determination of η_d. The peak wavelength of each laser spectrum was measured and the L-I signal was corrected for the wavelength-dependent responsivity of the detector. This was critical since, at the emission wavelength of the devices, the detector response can change by as much as 10% for only a 1.5% change in wavelength, which can easily occur should the device length and temperature change. Measurements were taken at a pressure of < 20 mTorr to prevent moisture condensation at low temperatures. The laser facet was situated ~ 2 mm from the large area anti-reflection coated SiGe detector.

The efficiency was extracted from the slopes of the above-threshold linear regions of the L-I curves. Plots of η_d^{-1} *vs.* L at -50°C and 20°C are given in Figs. 3.3a and 3.3b, and demonstrate the expected linear length dependence. At higher temperatures and lower well numbers, however, η_d^{-1} exhibits a non-linear length behaviour with a minimum which

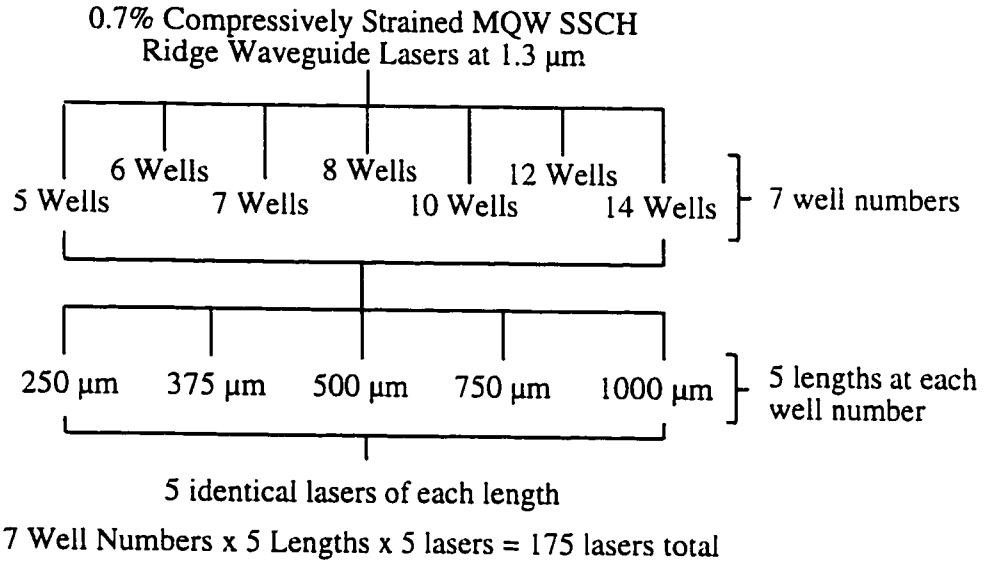

Figure 3.2 - Summary of the devices under study.

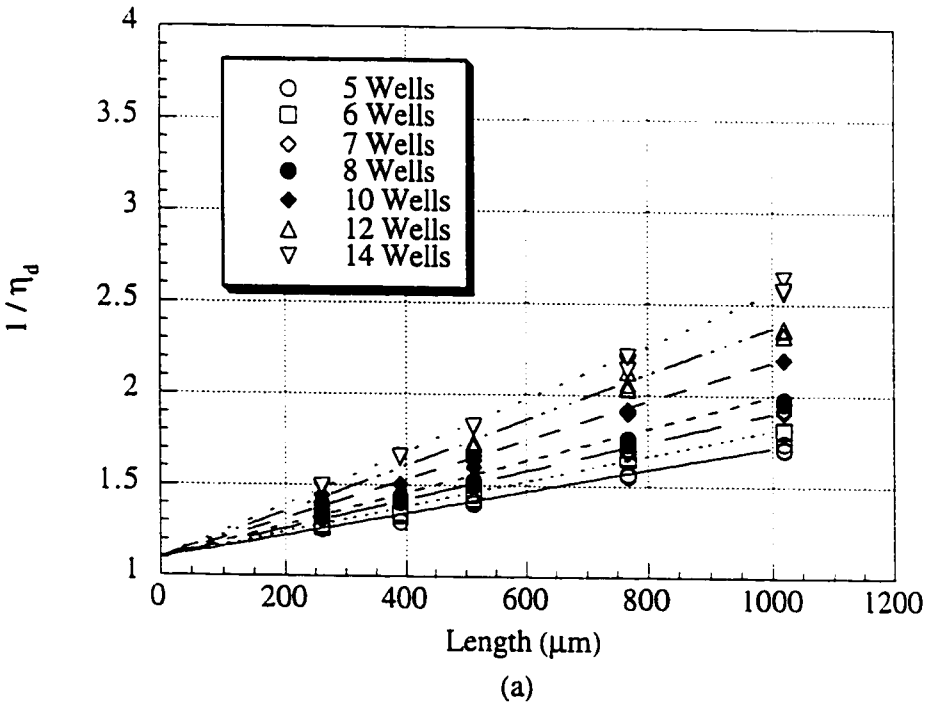

(a)

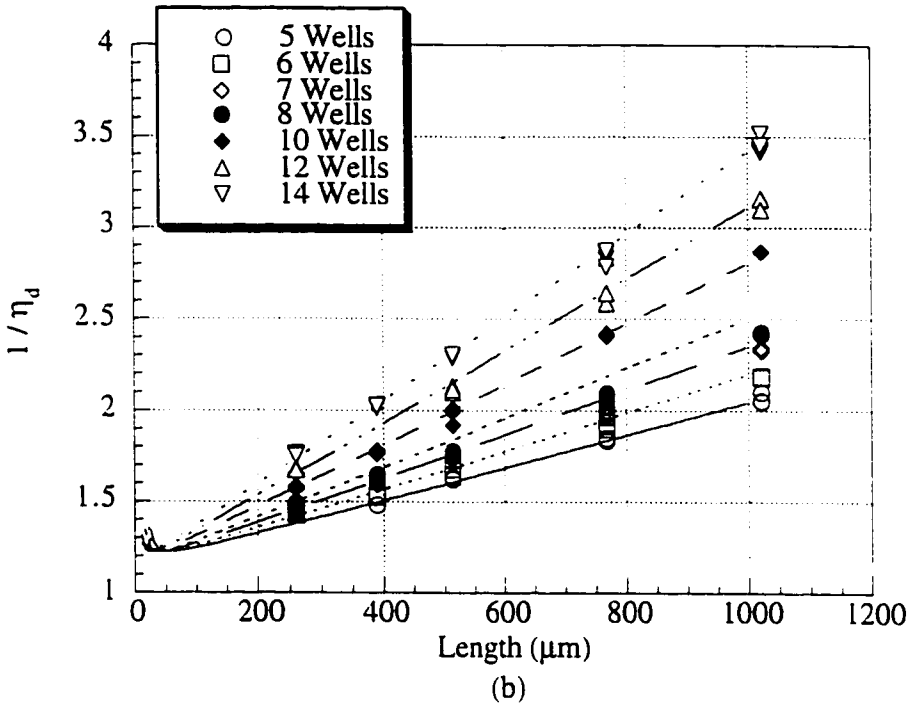

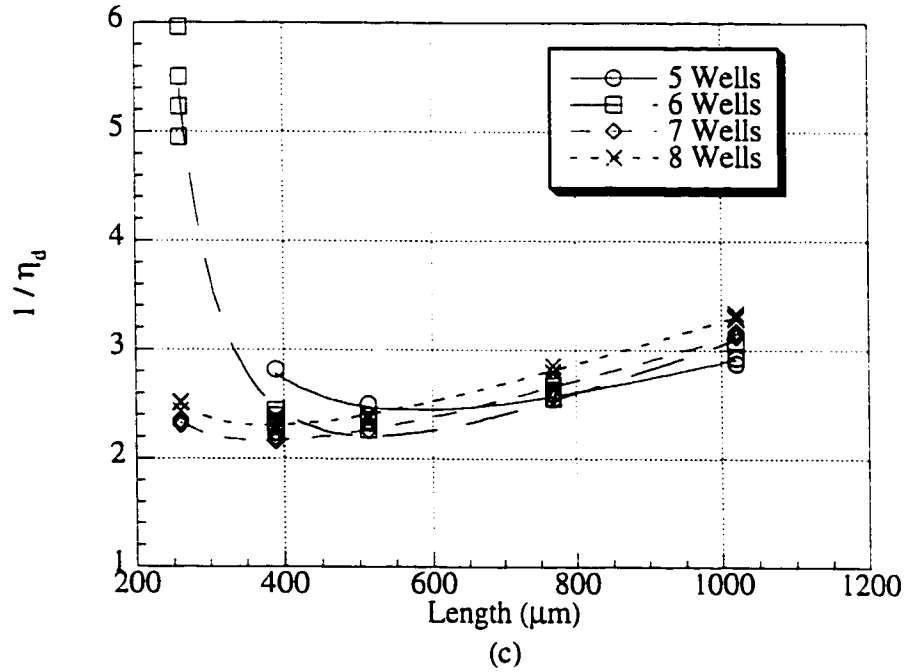

Figure 3.3 - Observed reciprocal differential quantum efficiency as a function of length. (a) -50°C and (b) 20°C are shown with the lines representing numerical fits from the model in Section 3.3. The fitted curves are extrapolated to low lengths and terminate where lasing theoretically ceases. (c) shows the anomalous length behaviour at 80°C for various well numbers with lines provided as guides to the eye.

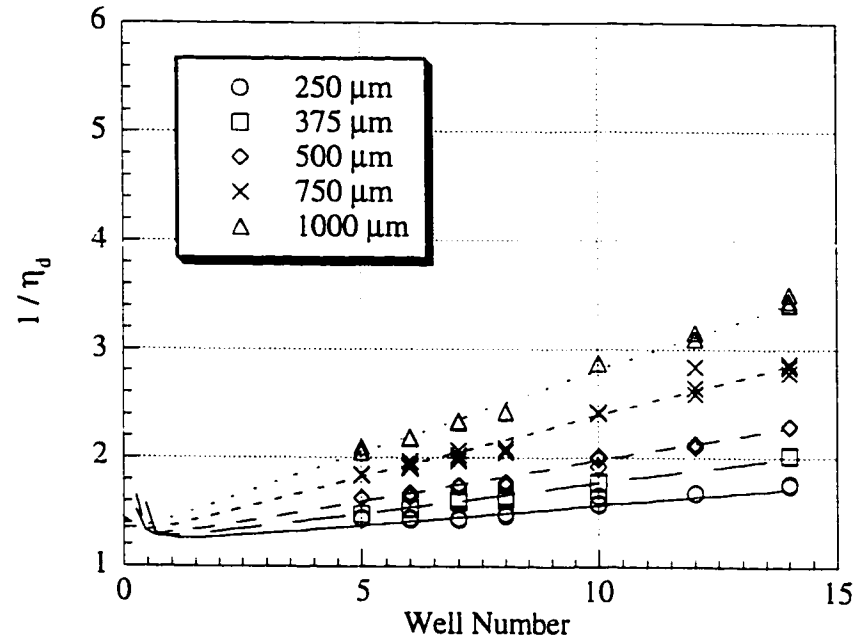

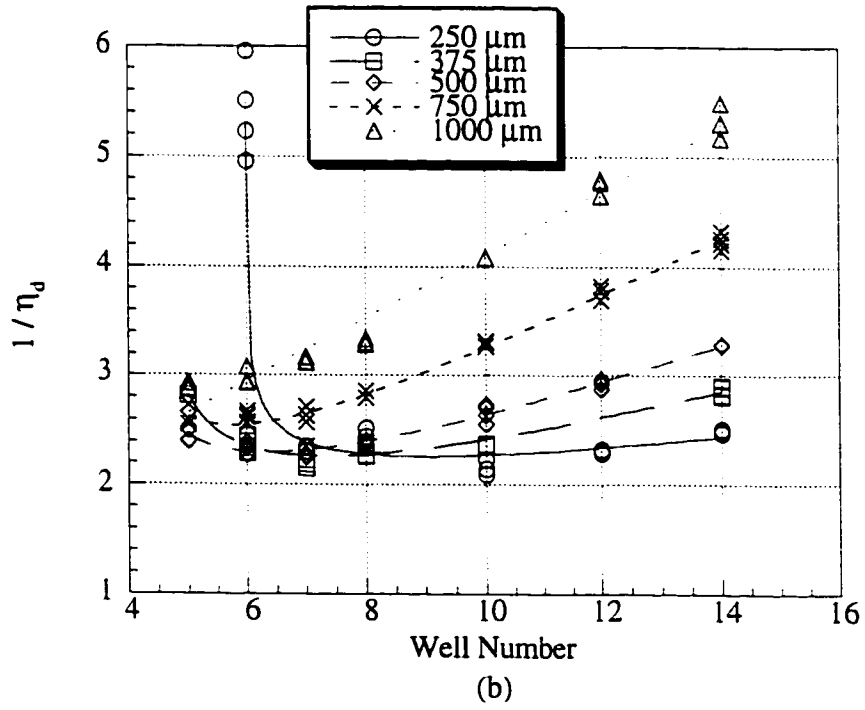

Figure 3.4 - Observed reciprocal of the differential external efficiency as a function of well number for (a) 20°C with the lines representing numerical fits and (b) 80°C where the lines are guides to the eye.

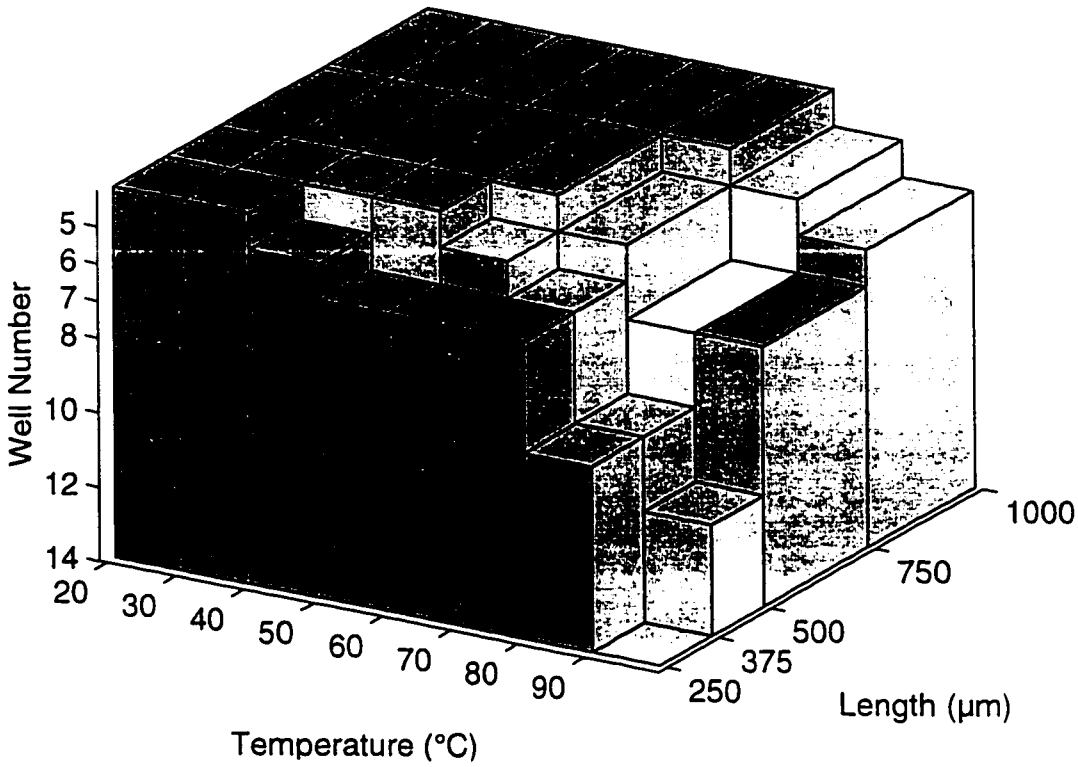

Figure 3.5 - Schematic representation of parameter space. The shaded regions indicate lasers which exhibited normal behaviour. Notches missing from the cube at high temperature, low length, and low well number indicate anomalous regions. η_d^{-1} values at all (N_W, L) below 40°C fell in the normal regime.

shifts with well number as shown in Fig. 3.3c for 80°C. Figure 3.4 shows that the corresponding dependence of η_d^{-1} on well number, N_W, is similarly linear at low temperatures and non-linear at higher temperatures and lower lengths.

The behaviour of η_d can be divided into two regimes: a *normal* region, where η_d^{-1} falls on a straight line as a function of N_W and L (hereafter referred to by the co-ordinates (N_W, L)), and an *anomalous* region where the (N_W, L) dependence of η_d^{-1} deviates significantly from linearity. Figure 3.5 illustrates the division of the three-dimensional parameter space of (N_W, L, T), where T is the heat sink temperature, into normal and anomalous efficiency regimes for the devices under study.

The standard method [2] for obtaining the loss coefficient in the normal regime at a given well number and temperature is by graphing η_d^{-1} *vs.* L and dividing the slope, $\eta_i^{-1}\alpha / \ln(1/R)$, by the observed intercept, η_i^{-1}, and multiplying by ln(1/R) where here R = 0.3 is assumed (see (3.8)). It will be shown in Section 3.3 that the observed value of η_i is not necessarily an accurate measure of the internal efficiency when the loss coefficient has an implicit length dependence. The reciprocal of the intercept for this laser set varies between 0.9 and 0.7 over the normal regime. Figure 3.6 contains a plot of the α obtained by this method as a function of well number for a variety of temperatures. As the temperature increases the optical loss per well increases. However, the intercept at $N_W = 0$ decreases with temperature and in fact becomes significantly negative at higher T. If the N_W dependence of α were caused by increased scattering losses at the additional interfaces introduced by added well and barrier layers, then the intercept would represent

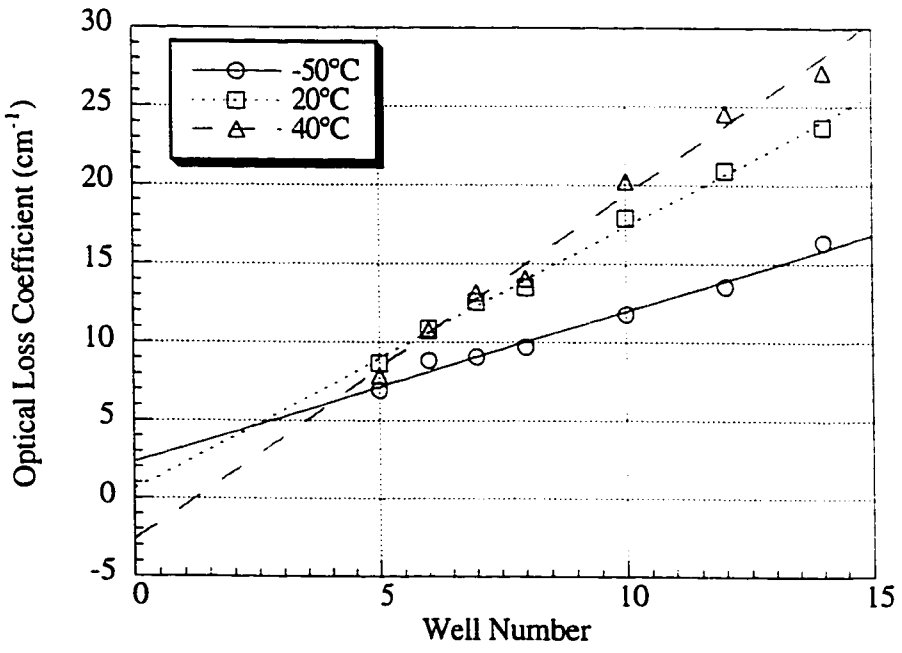

Figure 3.6 - The measured optical loss coefficient at -50°C, 20°C and 40°C. The intercept decreases with temperature. Note the negative intercept at 40°C which cannot be easily explained by scattering at the hetero-interfaces.

the residual losses. The fact that the intercept decreases and becomes negative implies that interfacial scattering losses cannot fully explain this behaviour.

3.3 ANALYSIS

Equation (3.8) for the differential efficiency is valid to zeroth order in δ, as defined in Section 2.8. Since δ is changing above threshold, it can be assumed that as long as the L-I characteristic above threshold is linear and the gain is constant along the length of the cavity, the contribution of first and higher-order terms are insignificant since the external efficiency would then be changing with drive current. Any deviation from a linear length dependence or a non-constant dependence on well number must therefore be due to implicit variations of η_i and α rather than a departure from (3.8) itself.

In light of the above observations and those in Section 3.2, a phenomenological model which includes inter-valence band absorption (IVBA) in the quantum wells is presented in Section 3.3.1. IVBA is the absorption of a photon resulting in a promotion of an electron from the split-off band to the heavy-hole or light hole band. It will be shown that the normal differential quantum efficiency can be accurately described with a minimum of fitting parameters by considering only the gain/loss contribution to η_d while keeping the internal efficiency constant. The apparent value of η_i given by the intercept of the η_d^{-1} *vs.* L graph will appear to change due to the length dependence of the IVBA. Although it has been suggested that IVBA is also responsible for the anomalous behaviour [7], it will be shown that this hypothesis is not quantitatively consistent with the analysis in the normal regime, so that changes in η_i becoming non-negligible must be partly responsible for the behaviour in the anomalous regime.

3.3.1 Inter-Valence Band Absorption

Inter-Valence Band Absorption (IVBA) is the absorption of a photon due to an electronic transition from the split-off band into holes in the heavy-hole band, as depicted in Fig. 3.7. The first investigation of IVBA as a mechanism for the temperature dependence of the optical losses in semiconductor lasers was by Adams *et. al.* [11]. A discussion is given in that reference about various possible mechanisms, including electron transitions from the conduction band minimum to higher minima, impurity-conduction band transitions, valence band transitions corresponding to these, and free carrier absorption due to plasma effects. The conclusion reached in [11] and invoked here is that IVBA is dominant.

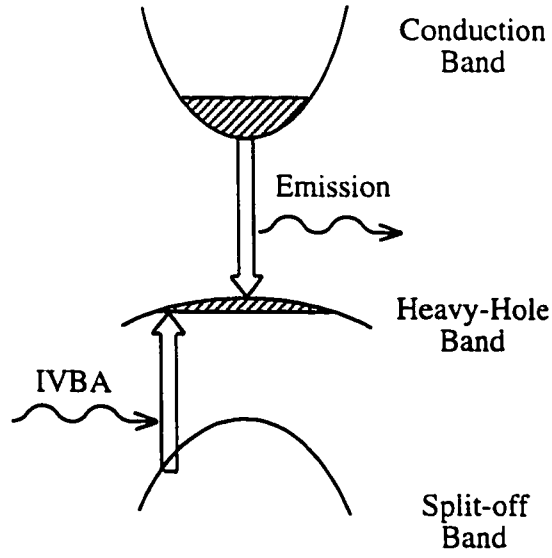

Figure 3.7 -Schematic diagram of the band structure indicating absorption via IVBA.

3.3.2 IVBA Model

In Section 2.6, the losses, α, were written as the sum of the contributions of IVBA and carrier-independent residual losses. At threshold this can be expressed as

$$\alpha_{th} = \Gamma\gamma n_{th} + \alpha_0. \tag{3.9}$$

Above threshold, the gain can be approximated by its value at the high-gain limit, $g_{th} = \ln(1/R)/L$, making the threshold condition:

$$\begin{aligned} g_{th} &= (B-\alpha)_{th}, \\ \Gamma\beta\ln(n_{th}/n_0) - \Gamma\gamma n_{th} - \alpha_0 &= \ln(1/R)/L. \end{aligned} \tag{3.10}$$

In Chapter 2, it was assumed that IVBA in the wells is dominant. However, there is actually some uncertainty as to whether IVBA in the well, barrier, or cladding regions is dominant and, hence, what value should be associated with the confinement factor and carrier density IVBA loss term in (3.9) and (3.10). IVBA in the cladding (outside the SSCH) is excluded from consideration since the carrier density in this region is expected to change with current and, if significant, would result in increasing IVBA losses and a non-linear L-I curve. Measurements in unstrained and strained MQW lasers [12] indicate that IVBA is suppressed in some compressively strained materials, while theoretical calculations [13] indicate that IVBA is dependent on the specific band structure and may, in fact, increase with compressive strain under certain conditions. This would suggest that the IVBA in both barrier and well states should be considered. Figure 3.8 is a plot of the results of cold cavity calculations of the optical confinement factor of the wells (Γ_W) and barriers (Γ_B) using the effective index [2] and transfer matrix method [14]. The calculation reveals that Γ_B is not a steadily increasing function of well number, because of the variation in the size of the stepped region. However, from Fig. 3.6 it is known that the losses vary linearly with well number. If IVBA is the source of the variation in losses, it must be present predominately in the wells, since only Γ_W exhibits the appropriate linear dependence on well number, $\Gamma_W = CN_W$, with $C \approx 0.0048$.

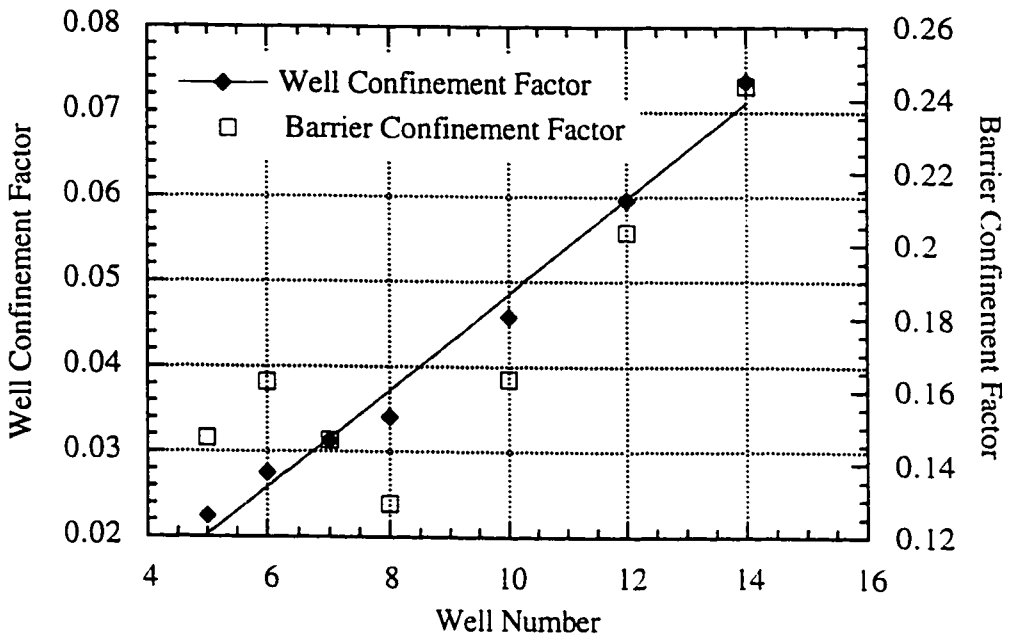

Figure 3.8 -Cold cavity calculations of the confinement factors in the well and barrier regions. The well confinement factor increases approximately linearly with well number ($\Gamma = 0.0048 \cdot N_W$) while the barrier confinement factor decreases appreciably for seven and eight wells.

3.3.3 Fitting Procedure

It was found that (3.8)-(3.10) could be used to describe the data in the normal regime with the following three assumptions:

i) at -50°C, β is large enough that n_{th} has a negligible dependence on (N_W, L),

ii) the actual internal efficiency in the normal regime is independent of well number and temperature, and

iii) α_o represents the residual optical losses due to scattering in the cladding and coupling into radiation modes, and is independent of well number and temperature.

At -50°C, the internal efficiency as measured from the intercept of the η_d^{-1} *vs.* L graph for all well numbers is essentially the same, $\eta_i = 0.909 \pm 0.005$. From assumption

(i) this is taken to be the true value of the internal efficiency, unaffected by the length dependence of IVBA losses. Since η_i for these lasers is constant from -50°C to -30°C, this is a valid assumption, as will be discussed in Section 3.4.4. According to assumption (ii), η_i is fixed at this value for all well numbers and temperatures greater than -50°C in the normal regime. Finally, if assumption (i) applies then the optical losses at -50°C can be plotted as a function of well number with the intercept being the residual losses, α_0. It is found to have a value of $\alpha_0 = 1.6\ cm^{-1}$ and is fixed at this value, according to assumption (iii).

Since the accuracy of the parameter values obtained from the fits depends upon the validity of the assumptions, some further discussion is required. At each temperature, η_d^{-1} is a function of two variables, (N_w, L). In the normal regime, the description of the variation of η_d^{-1} with each variable requires the knowledge of a slope and an intercept. It is therefore a bilinear surface which can be described in terms of a total of four independent parameters a, b, c, d:

$$\eta_d^{-1} = a + bN_w + cL + dN_wL. \qquad (3.11)$$

With the above assumptions, however, the model is able to successfully describe all four degrees of freedom of the normal efficiency with only two independent fitting parameters, as will be shown below. Although additional parameters could be introduced to describe, for example, changes in the internal efficiency with temperature due to leakage over the hetero-barrier, the fact that these changes can be predicted by the other two fitting parameters would have to be considered a coincidence. The principle of Occam's razor† is

---

†*Quia frustra fit per plura potest equaliter fieri per pauciona*: It is vain to do by more what can equally done by fewer. In other words, the explanation for an event which requires the least number of assumptions and coincidences is the correct one. This argument is often used in the field of fundamental theoretical physics. Although it is usually associated with Sir William of Occam, a 14th century philosopher, it had been previously used by others including, most notably, Aristotle [15].

applied by considering this a validation of the assumptions.

Although (3.10) will be used in the subsequent analysis, it is transcendental in n_{th} and its effect on (3.8) is not immediately obvious. It is instructive to approximate (3.10) so that n_{th} can be solved for explicitly. This is done by assuming that $\beta >> \gamma n_0$ and setting α_o to zero for clarity (it does not substantially alter the qualitative result). Solving for n_{th} and using (3.9) and (3.10),

$$\eta_d^{-1} = \eta_i^{-1}\left\{1 + \Gamma\gamma n_0 \exp\left[\frac{\ln(1/R)}{\beta\Gamma L}\right]\frac{L}{\ln(1/R)}\right\}. \tag{3.12}$$

Equation (3.12) depends linearly on length and well number when the exponent is small, such as at long lengths, high well number, and high β. When the length and well number decrease, the exponent becomes significant and a sharp increase should be observed in η_d^{-1}.

For the purposes of the fit, (3.8)-(3.10) may be re-written as

$$\eta_d^{-1} = \eta_i^{-1}\left[1 + \frac{a_2 X N_w + \alpha_0}{\ln(1/R)} L\right], \tag{3.13a}$$

$$a_1 N_w \ln(X) - a_2 X N_w - \alpha_0 = \frac{1}{L}\ln\left(\frac{1}{R}\right), \tag{3.13b}$$

where

$$X = n_{th} / n_0,$$
$$a_1 = \beta C,$$
$$a_2 = \gamma n_0 C$$

and $\eta_i = 0.909 \pm 0.005$ and $\alpha_o = 1.6 \pm 0.1\ cm^{-1}$ are fixed at the -50°C values. X is the threshold carrier density normalized by n_0, and γn_0 is referred to as the scaled IVBA coefficient. Note that the constant C from the proportionality fit to the Γ_W *vs.* N_W plot of Fig. 3.8 has been absorbed into the fitting parameters a_1 and a_2.

The parameters a_1 and a_2 were fitted to the data using (3.13a) in the normal regime at each temperature above -50°C using the least squares Marquardt method in two

dimensions (N_W, L) and manual searches of parameter space [16] with R = 0.3. At each iteration of the fit, (3.13b) was used to determine the magnitude of the scaled threshold carrier density, X. The curves in Figs. 3.3a, 3.3b, and 3.4a represent the best fits and terminate at low (N_W, L) where (3.13b) no longer has any roots. When the fits are extrapolated into the anomalous efficiency regime, the exponential curling up described qualitatively by (3.12) cannot explain the anomalous behaviour of the efficiency. Figure 3.9 contains plots of the gain and scaled IVBA coefficients as a function of heat-sink temperature. Since the data used for the fits was obtained under CW conditions, changes in the junction temperature with length and well number at a constant heat sink temperature are possible. In the normal regime, this would require the temperature change due to internal heating to be linear over a factor of four change in L and a factor of three change in N_W. This seems likely only for small changes in internal heating. The result would be an over-estimation in the IVBA coefficient. It is recognized, however, that even if the junction temperature does not change significantly with N_W and L, it may be significantly higher than the heat-sink temperature. Over the measured range of heat-sink temperatures, the gain coefficient is found to vary by an order of magnitude, while the scaled IVBA coefficient varies by a factor of about two. This supports the conclusion reached in [14] that it is the temperature dependence of the gain rather than IVBA that primarily affects the temperature sensitivity of InGaAsP/InP MQW lasers.

Although n_{th} and n_0 cannot be determined separately, the value $X = n_{th} / n_0$ can be found. Typical values obtained from the fits at 20°C ranged from 1.06 for (N_w, L) = (14, 1000 μm) and 1.32 for (5, 250 μm). At 80°C, n_{th} / n_0 increased to 1.38 at (14, 1000 μm) and (5, 250 μm) did not lase. The condition for lasing is discussed in Section 3.4.1. The optical losses due to IVBA are found to be 23.7 ± 0.3 cm^{-1} at (14, 1000 μm, 20°C), 10.6 ± 0.1 cm^{-1} at (5, 250 μm, 20°C), and 40.8 ± 0.6 cm^{-1} at (14, 1000 μm, 80°C).

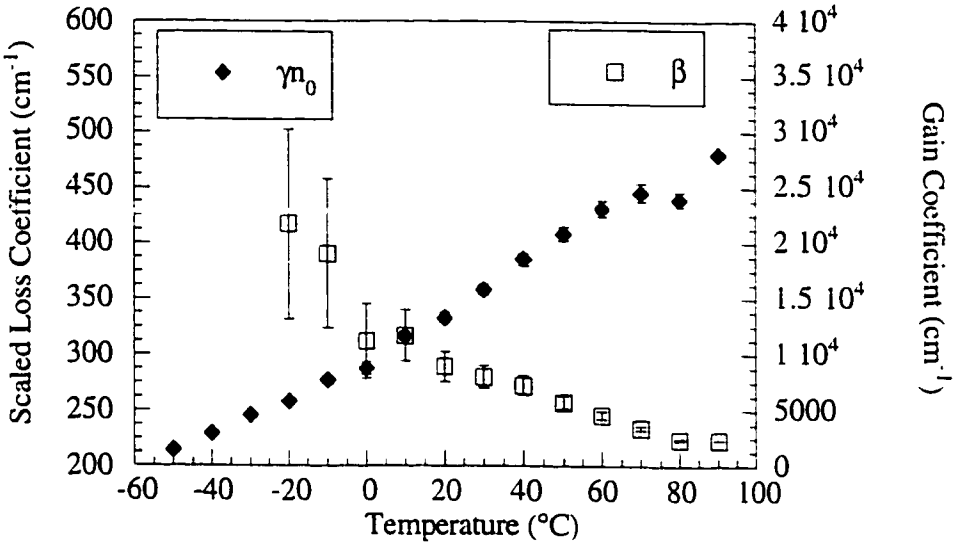

Figure 3.9 - β and γn_0 as a function of temperature obtained from fits to the data. The magnitude of β below -20°C is too large to obtain reasonably accurate values and they are omitted from the plot.

IVBA accounts for between 76% and 98% of the material losses in the measured parameter space.

The anomalous efficiency has been analyzed as a function of length and attributed to IVBA in the barriers caused by carriers overflowing from the wells but remaining in the SSCH under high inversion conditions [5]. We model the barrier IVBA with a method similar to [5]. To maintain an analytical expression, the carriers at the barrier are assumed to be non-degenerate. The hole carrier concentration in the wells, n_W, is given by

$$n_W = \int_{E_W}^{E_B} D_W f(E) dE \qquad (3.14)$$

where E_B the energy level of the barrier, and E_W the energy of the bottom of the QW subband. $f(E)$ and D_W are the Fermi function and 2-D density of states for a single QW subband, respectively:

$$D_W = \frac{4\pi m_W}{h^2 L_W} \quad ,$$

$$f(E) = \frac{1}{1+e^{(E-E_f)/kT}} \quad ,$$

where m_w is the effective mass in the well, L_w is the well width, E_f is the energy of the Fermi level, and k is Boltzman's constant. Performing the integration of (3.14) gives

$$n_W = kTD_W \ln\left[\frac{1+e^{-(E_W-E_f)/kT}}{1+e^{-(E_B-E_f)/kT}}\right]. \tag{3.15}$$

Similarly, the barrier concentration is

$$n_B = \int_{E_B}^{\infty} D_B E^{3/2} f(E) dE \tag{3.16}$$

where

$$D_B = 4\pi\left[\frac{2m_B}{h^2}\right]^{3/2}.$$

Using $f(E) \approx e^{-(E-E_f)/kT}$, (3.16) becomes

$$n_B = D_B e^{-(E_B-E_f)/kT}. \tag{3.17}$$

Equations (3.15) and (3.17) can be used to relate the well- and barrier- carrier densities

$$n_B = D_B \frac{e^{n_W/D_W kT} - 1}{e^{\Delta E/kT} - e^{n_W/D_W kT}} \tag{3.18}$$

where $\Delta E = E_B - E_W$ is the valence band offset. If the barrier is non-degenerate and the well is degenerate, $e^{\Delta E/kT} >> e^{n_W/D_W kT}$ and (3.18) simplifies to

$$n_B = D_B e^{-\Delta E/kT}\left(e^{n_W/D_W kT} - 1\right). \tag{3.19}$$

Also, if the IVBA in the barrier, α_B, is assumed to be proportional to the hole density, then it can be added to the expression for the total loss in (3.9) and expressed in terms of the scaled threshold carrier density as

$$\alpha_B = a_3[e^{a_4 X} - 1] \tag{3.20}$$

with $a_3 = \Gamma_B \gamma_B D_B e^{-\Delta E/kT}$ and $a_4 = n_0 / D_W kT$ where γ_B is the IVBA coefficient in the barrier. This was done for the data at 60°C and 5 wells. Values of $a_1 = 0.0048 \cdot 4580 = 22.0\ cm^{-1}$ and $a_2 = 0.0048 \cdot 431 = 2.07\ cm^{-1}$ were obtained from the η_d^{-1} data in the normal regime at this temperature as given by Fig. 3.9, and a_3 and a_4 were used as fitting parameters. From the best fit shown in Fig. 3.10, it can be seen that it is not possible to have high enough losses at the lower lengths to give the correct η_d^{-1} and still have a lasing device. Therefore, if IVBA in the barrier is included while accounting for IVBA in the wells, the anomalous efficiency still cannot be quantitatively described. It is concluded that in the anomalous regime, changes in η_i caused by changes in the leakage currents must become significant.

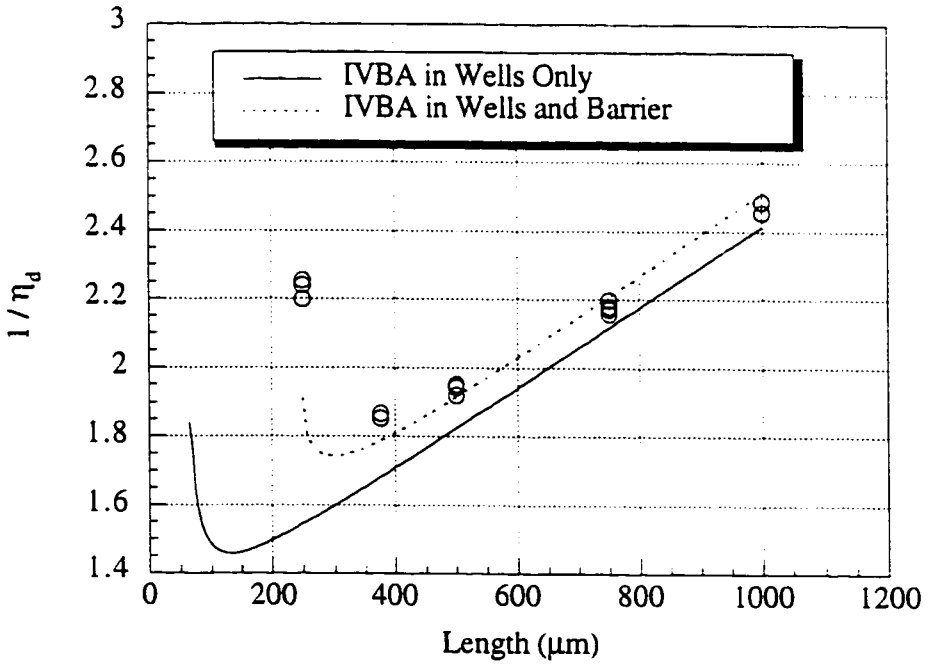

Figure 3.10 - Reciprocal differential efficiency extended to the anomalous regime of 5 wells at 60°C, with the values for β and γn_0 obtained from the normal regime at this temperature. The solid line represents the best fit when IVBA in the barriers is added. Both curves terminate at low lengths where lasing theoretically ceases.

3.4 CONSEQUENCES OF IVBA

3.4.1 Minimum Lasing Condition

Equation (3.10) can be pictured as the intersection between a logarithmic gain curve and a straight loss line as depicted schematically in Fig. 3.11. The intercept of the loss line is determined by the mirror losses, $\alpha_m = \ln(1/R)/L$, and the residual losses α_o. The slope is given by the value of $\Gamma_w\gamma$. As β decreases and the slope or intercept of the loss line increases, a point will be reached where the loss line is tangent to the gain curve. Lasing will not occur for any further decrease in gain or increase in loss. In contradistinction, if the losses were a constant function of carrier density, then the two curves would always cross unless some other mechanism interfered. The tangential condition gives a locus of (Γ_w, L) values at a given β and γn_0 that are the minimum values required for lasing to occur. Of course, lasing may cease before this boundary due to other effects.

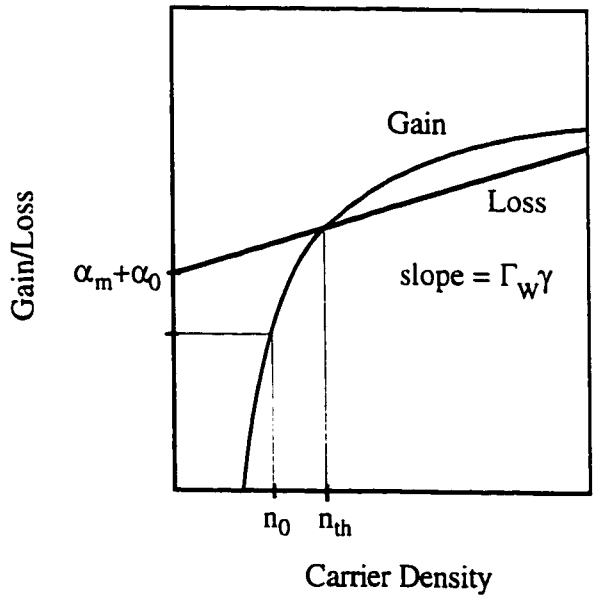

Figure 3.11 - Schematic representation of gain and losses as a function of carrier density in the IVBA model.

From (3.10) it can be shown that the gain curve and the loss line are tangential when $n_{th} = \beta / \gamma$. Substitution into (3.10) gives the minimum lasing criterion:

$$\Gamma_W \beta \ln\left(\frac{\beta}{e\gamma n_0}\right) = \frac{\ln(1/R)}{L} + \alpha_o . \qquad (3.21)$$

The contour obtained from (3.21) separating lasing from non-lasing values of (N_W, L) for the values of β and γn_0 obtained from the normal regime at 90°C is shown in Fig. 3.12, where Γ_w has been normalized to N_W by the constant C. Lasers from this experiment which did not lase are indicated by open circles, while the closed circles represent successful lasing. In all cases, all of the identical lasers exhibited the same behaviour.

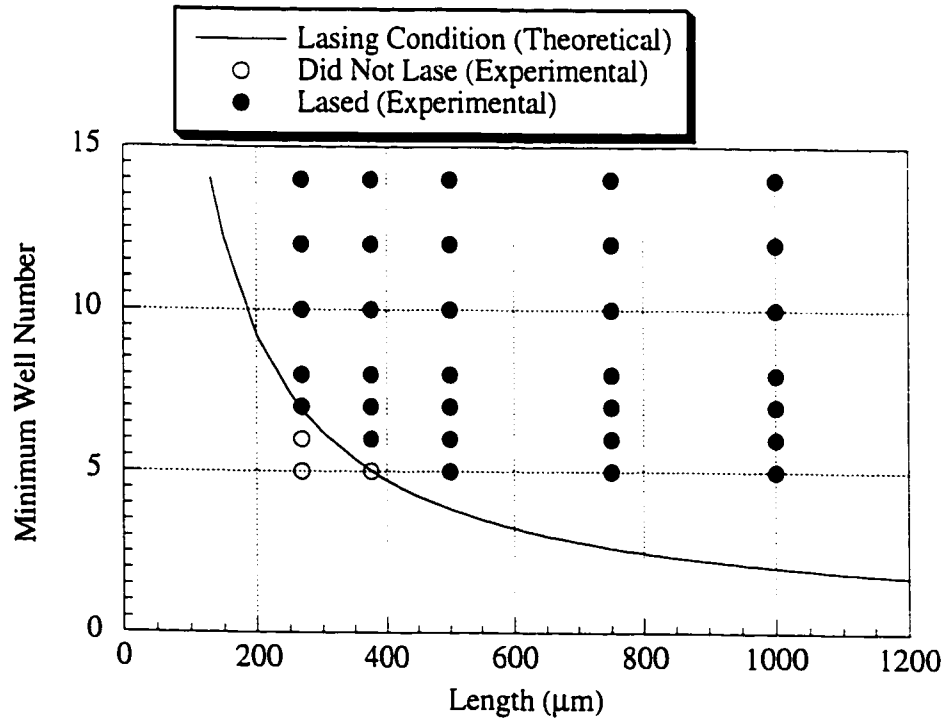

Figure 3.12 - The minimum lasing condition. The solid line represents the theoretical contour separating non-lasing devices on the low side and lasing devices on the high side. Open circles represent lasers which failed to lase experimentally while the closed circles represent successful lasing.

3.4.2 Minimum in the Gain/Loss Reduction of η_d

From Fig. 3.10, it can be seen that the IVBA model presented here predicts a maximum η_d in (Γ_w, L). Actual devices exhibit a maximum at (Γ_w, L) values somewhat higher than this, as discussed in Section 3.3, due to changes in η_i becoming significant. The maximum from gain and losses in the IVBA model cannot therefore be used to fully optimize a laser design in this case, but may help to provide an estimate of the optimal value, how it changes under various conditions, and to what extent η_i modifies it. The partial derivative of (3.8) can be taken with respect to Γ_w with the help of (3.9) and (3.10) to obtain the value of the optical confinement factor required to achieve a maximum in η_d at a given length,

$$\Gamma_{max} = \frac{\alpha_o + \frac{1}{L}\ln(1/R)}{\beta - e\gamma n_0}. \tag{3.22}$$

Substituting (3.22) into (3.10) yields a scaled threshold carrier density of $n_{th}/n_0\big|_{\Gamma_w=\Gamma_{max}} = e$. combining (3.22), (3.8) and (3.9) gives

$$\eta_d^{-1}\big|_{\Gamma_w=\Gamma_{max}} = \eta_i^{-1}\left[\frac{\beta}{\beta - e\gamma n_0}\right]\left[1+\alpha_o L\right]. \tag{3.23}$$

It can be seen from (3.23) that at Γ_{max} the gain/loss component of the efficiency has a length dependence due only to the scattering losses.

3.4.3 Physical Significance of the Measured η_i

The value of η_i measured using the standard method of extrapolating η_d^{-1} to zero length will be affected by the length-dependent inter-valence band absorption losses. This can be illustrated in closed form in the normal regime by approximating the logarithmic gain curve by a linear function, $\Gamma\beta\ln(n_{th}/n_0) \approx \Gamma\beta'(n_{th} - n_0')$. Equation (3.10) can then be used to solve for n_{th}, similar to reference [1], to give

$$n_{th} = \frac{\Gamma_W \beta' n_0' + \alpha_o + \ln(1/R)/L}{\Gamma_W(\beta' - \gamma)}. \tag{3.24}$$

Combining (3.8)-(3.10) and (3.24), one obtains

$$\eta_d^{-1} = \eta_{iM}^{-1}\left[1 + \frac{\alpha_M}{\ln(1/R)}L\right] \tag{3.25a}$$

where

$$\eta_{iM} = \eta_i(1 - \gamma/\beta'), \tag{3.25b}$$

$$\alpha_M = \alpha_o + \Gamma_W \gamma n_0'. \tag{3.25c}$$

From (3.25b) it can be seen that actual internal efficiency is underestimated unless $\gamma/\beta' << 1$.

Therefore, care must be taken when measuring η_i to ensure that the design and operating conditions are such that the intercept of η_d^{-1} *vs.* L is not affected by IVBA losses. From Fig. 3.9 it can be seen that $\gamma n_0/\beta$ (and by inference $\gamma n_0'/\beta'$) has a strong temperature dependence. If the internal efficiency is measured at a few temperatures near the temperature of interest, values of η_{iM} which are constant over the temperature range are likely to have a small $\gamma n_0'/\beta'$ and hence be an accurate reflection of η_i. Otherwise, the physical meaning of the parameter extracted is questionable.

3.5. Chapter Summary

A study of external differential quantum efficiency and optical loss has been performed where the three variable parameters of well number, length, and temperature were altered systematically on otherwise similar devices. A phenomenological model based on widely accepted expressions for gain and inter-valence band absorption and a constant internal efficiency was used to successfully describe the linear variations of the reciprocal external efficiency with well number and length with a minimum number of fitting parameters. This

model predicts a minimum condition for lasing, a maximum in the gain/loss contribution to the external efficiency as a function of well number and length at a given temperature, and a potential to cause an underestimation of the measured internal efficiency. Quantitative measurements of the gain coefficient, β, and scaled IVBA loss, γn_0, support the conclusion that the gain has a higher temperature sensitivity than does IVBA.

The range over which the IVBA model accurately describes the external efficiency for the devices measured was up to 40°C for fewer wells and shorter cavity lengths (~5 wells, 250 μm length) up to 90°C for more wells and longer cavities (> 8 wells, > 500 μm length). It was found that points outside this normal region could be identified by their anomalous behaviour in that their η_d^{-1} values did not fall on a straight line when plotted as a function of L. In this anomalous regime, the external efficiency could not be explained entirely by the IVBA model, even when it was extended to include IVBA in the barrier states within the SSCH. It is concluded that in the anomalous regime, the internal efficiency must be changing non-negligibly due to increased current leakage out of the SSCH and/or laterally outside the ridge. The uncertainty in input parameters required to calculate the band structure under bias and the amount of scatter present in the anomalous data in this study prevent any conclusive quantitative analysis of η_i in this regime.

REFERENCES

[1] K. Prosyk, J. G. Simmons, J. D. Evans, "Well number, length, and temperature dependence of efficiency and loss in InGaAsP-InP compressively strained MQW ridge waveguide lasers at 1.3 μm", *IEEE J. Quantum Electron.*, vol. 33, pp. 1360-1368, 1997.

[2] G. P. Agrawal, N. K. Dutta, *Semiconductor Lasers*, 2nd ed., Van Nostrand Reinhold, 1993.

[3] U. Koren, B. I. Miller, Y.K. Su, T.L. Koch, J.E. Bowers, "Low internal loss separate confinement heterostructure InGaAs/InGaAsP quantum well laser", *Appl. Phys. Lett.*, vol. 51, pp. 1744-1746, Nov. 1987.

[4] A. Kasukawa, T. Namegaya, N. Iwai, N. Yamanaka, Y. Ikegami, N. Tsukiji, "Extremely high power 1.48 μm GaInAsP/InP GRIN-SCH strained MQW lasers", *IEEE Photon. Tech. Lett.*, vol. 6, pp. 4-6, Jan. 1994.

[5] K. Tanaka, K. Wakao, T. Yamamoto, H. Nobuhara, T. Fuji, "Dependence of the differential quantum efficiency on the confinement structure in InGaAs/InGaAsP strained-layer multiple quantum-well lasers", *IEEE Photon. Tech. Lett.*, vol. 5, pp. 602-605, Jun. 1993.

[6] H. Asano, S. Takano, M. Kawaradani, M. Kitamura, I. Mito, "1.48-μm high-power InGaAs/InGaAsP MQW LD's for Er-doped fiber amplifiers", *IEEE Photon. Tech. Lett.*, vol. 3, pp. 415-417, May 1991.

[7] J. Z. Wilcox, S. Ou, J. J. Yang, M. Jansen, G. L. Peterson, "Dependence of external efficiency on laser length and reflectivities in multiple quantum well lasers", *Appl. Phys. Lett.*, vol. 55 , pp. 825-827, Aug. 1989.

[8] J. Diaz, I. Eliashevich, X. He, H. Yi, L. Wang, E. Kolev, D. Garbuzov, and M. Razeghi, "High-power InGaAsP/GaAs 0.8-μm laser diodes and peculiarities of operational characteristics", *Appl. Phys. Lett.*, vol. 65, p. 1004-1005, Aug. 1994.

[9] J. Diaz, I. Eliashevich, X. He, M. Stanton, M. Erdtmann, L. Wang, M. Razeghi, "Theoretical investigation of minority Carrier leakage of high-power 0.8 μm InGaAsP/InGaP/GaAs laser diodes", *Appl. Phys. Lett*, vol. 65, p. 2260-2262, Oct. 1994.

[10] H. J. Yi, J. Diaz, I. Eliashevich, M. Stanton, M. Erdtmann, X. He, L. J. Wang, and M. Razeghi, "Temperature dependence of threshold current density J_{th} and differential efficiency η_d of high-power InGaAsP/GaAs ($\lambda = 0.8\mu m$) lasers", *Appl. Phys. Lett.*, vol. 66, pp. 253-255, Jan. 1995.

[11] A. R. Adams, M. Asada, Y. Suematsu, S. Arai, "The temperature dependence of the efficiency and threshold current of $In_{1-x}Ga_xAs_yP_{1-y}$ lasers related to intervalence band absorption", *Japan. J. Appl. Phys.*, vol. 19, pp. L621-L624, Oct. 1980.

[12] G. Fuchs, J. Horer, A. Hangleiter, V. Harle, F. Scholz, "Intervalence band absorption in strained and unstrained InGaAs multiple quantum well structures", *Appl. Phys. Lett.*, vol. 60, pp. 231-233, Jan. 1992.

[13] T. Cho, H. Kim, Y. Kwon, S. Hong, "Theoretical study on intervalence band absorption in InP-based quantum-well laser structures", *Appl. Phys. Lett.*, vol. 68, pp. 2183-2185, Apr. 1996.

[14] L. M. Walpita, "Solutions for planar optical waveguide equations by selecting zero elements in a characteristic matrix", *J. Opt. Soc. Am. A*, vol. 2, p. 595-602, April 1985.

[15] G. Leff, *William of Ockham*, Manchester University Press, p. 35, 1975.

[16] P. R. Bevington, D. Keith Robinson, *Data Reduction and Error Analysis for the Physical Sciences*, 2nd ed., McGraw-Hill Inc., p. 161, 1992.

CHAPTER FOUR

TEMPERATURE SENSITIVITY OF THRESHOLD[†]

4.0 INTRODUCTION

THE temperature sensitivity of the threshold current has been the subject of a great deal of study (see [2] for a long list of references on the subject). The motivation from the practical standpoint is the variability of environmental conditions when a laser transmitter is placed in the field in an optical fibre network. Internal temperatures in a module box can range from -40°C to 85°C. Presently, thermo-electric coolers are used in the packaging of semiconductor lasers to stabilize the temperature. The coolers, associated circuitry, and added power consumption all contribute to a significant increase in the cost of the module. Aside from a deeper understanding of device physics, the ultimate goal of these studies is to develop a laser which can be operated over a wide temperature range without the need for actively controlling the temperature.

There have been a number of conflicting opinions as to the source of the highly sensitive threshold current in InP-based lasers [2]. At the time of this writing, a consensus

---

[†]The majority of this chapter has been published in [1].

appears to be forming in favour of a large temperature dependence of the gain (see Chapter 3 for further evidence supporting this hypothesis), although adherents to other mechanisms, such as Auger recombination and hetero-barrier leakage, still exist.

In this chapter, the results of a large scale study of the temperature sensitivity of the CW threshold current are presented. In Section 4.1, the method of characterization is discussed. Experimental results are presented in Section 4.2 and analyzed in Section 4.3. A summary of conclusions is given in Section 4.4.

4.1 CHARACTERIZATION METHODOLOGY

Traditionally, the temperature (T) dependence of the threshold current density, J_{th}, has been described by the Pankove relation [3]

$$J_{th} = J_P e^{T/T_0} \tag{4.1}$$

where J_P is the threshold current density extrapolated to $T=0$ and T_0 is the temperature sensitivity parameter. Equation (4.1) has the advantage that T_0 gives an intuitive feel for the change of threshold current with temperature. A difficulty arises in actually using (4.1) for characterizing lasers, however, since both J_P and T_0 are typically functions of temperature. This poses a problem for studies such as presented here which compare devices with different structures over a wide temperature range. Dividing the temperature range into arbitrary small segments over which T_0 is constant unnecessarily complicates the analysis.

An alternative relationship for the temperature dependence of semiconductor lasers has been derived from purely empirical considerations, and shown to be valid for a variety of devices over a temperature range of -50°C to 100°C [2], [4]:

$$\frac{\partial J_{th}}{\partial T} = D J_{th}^{n+1} \tag{4.2}$$

which, upon integration becomes

$$J_{th} = \left[\frac{n}{D}(T_{max} - T)\right]^{-1/n} \tag{4.3}$$

where n has been found to have a value near 1/2. The parameters n, D, and T_{max} are empirical parameters that are essentially independent of temperature, which makes meaningful comparisons between different device structures much easier. A more convenient form of (4.3) is

$$J_{th} = J_0\left(1 - \frac{T}{T_{max}}\right)^{-\zeta} \tag{4.4}$$

where: J_0 is the low T extrapolation of the threshold current density; T_{max} is the temperature at which J_{th} approaches infinity asymptotically when extrapolated to higher T, and acts as a scaling factor for the temperature axis; and ζ (= 1/n) is a dimensionless parameter describing the rapidity with which J_{th} increases as the temperature approaches T_{max}, a higher ζ indicating a greater sensitivity at the same temperature ratio, T / T_{max}.

4.2 Experiment and Results

The devices studied in this investigation are the same as in Chapter 3 (see Fig. 3.2 for the summary of devices), and the CW L-I curves from Section 3.1 were used. The threshold currents were obtained from linear fits to the above- and below-threshold portions of the L-I curve. The current at which the extrapolations of the two curves met was identified as threshold.

A three-parameter least-squares fit was used to determine the values of J_0, ζ, and T_{max} in (4.4) at each well number and length (again referred to by the parametric co-ordinates (N_W, L)). The fit was carried out simultaneously for all devices with similar (N_W, L) in order to get an average value for the fitting parameters, as well as an estimate of

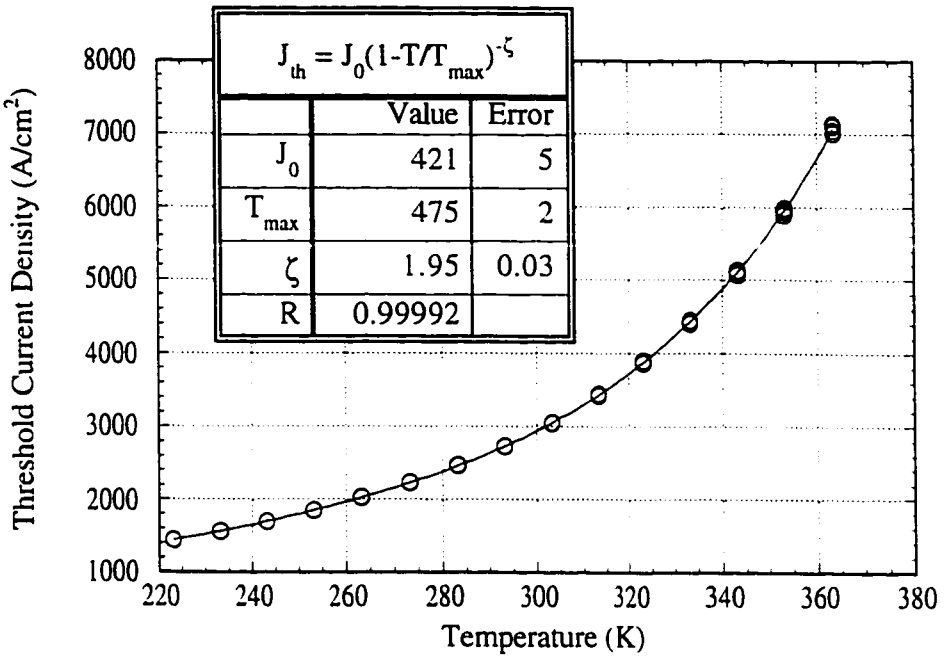

Figure 4.1 - Example of least squares fit of (4.4) to the threshold current data of devices with $(N_W, L) = (8, 500\mu m)$. R is the correlation factor.

the expected device-to-device variation. An example of such a fit for the five devices with $(N_W, L) = (8, 500\ \mu m)$ is shown in Fig. 4.1.

The variation of T_{max} with well number and length is shown in Figs. 4.2a and 4.2b, respectively. It is observed in Fig. 4.2b that T_{max} increases with length as has been previously reported [4]. The N_W dependence in Fig. 4.2a shows a similar trend, with T_{max} increasing for larger well numbers but in a less systematic manner than for the cavity length. Since devices with different well numbers are from different wafers and growth runs, we attribute these erratic variations to small, uncontrollable variations in structure.

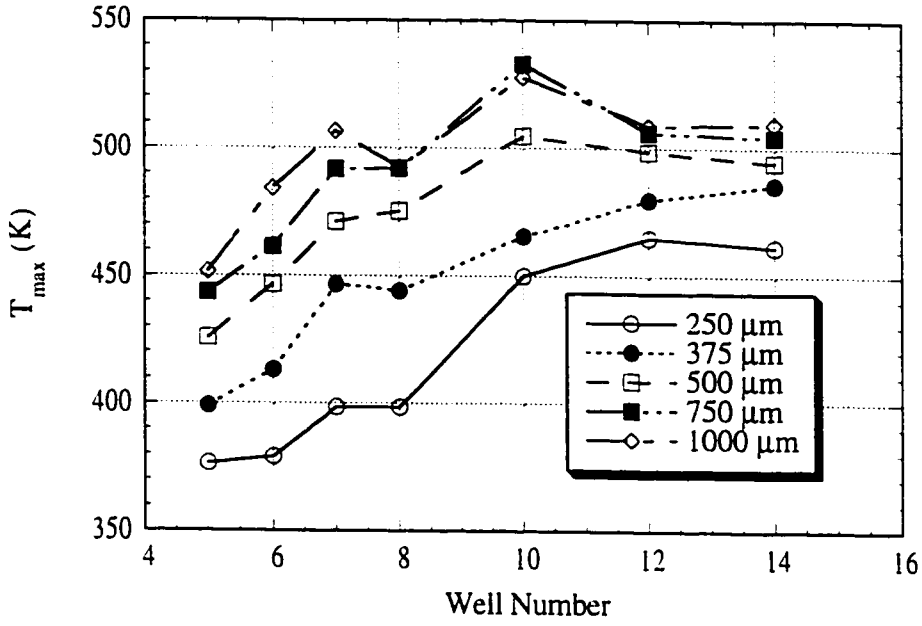

(a)

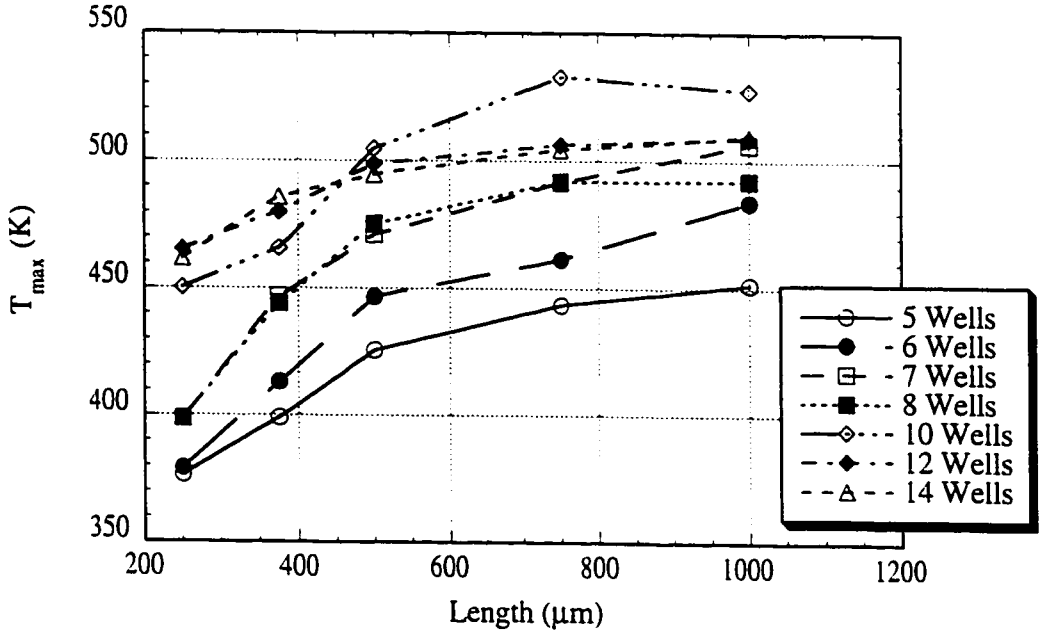

(b)

Figure 4.2 - The dependence of T_{max} on (a) well number and (b) length.

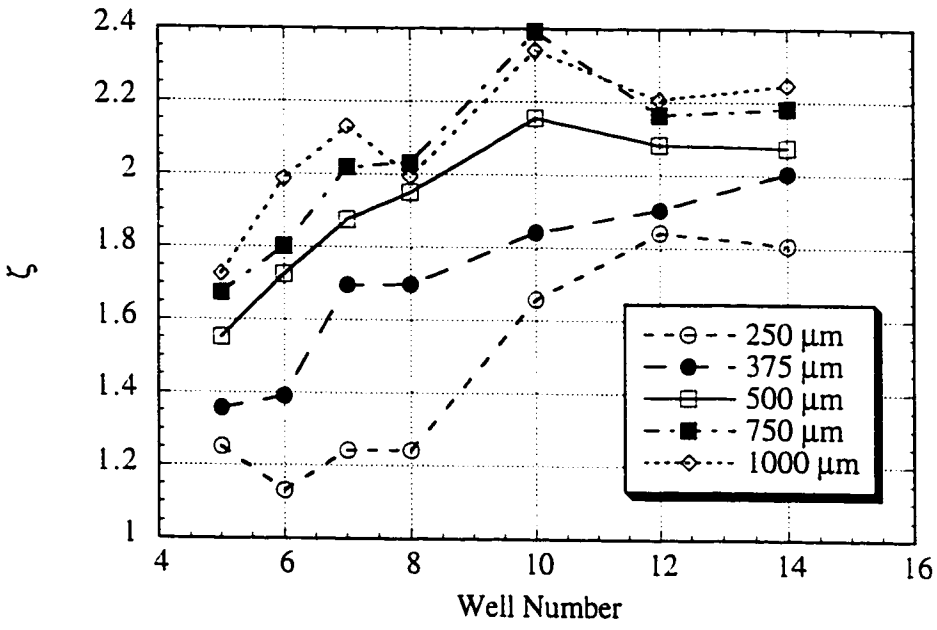

(a)

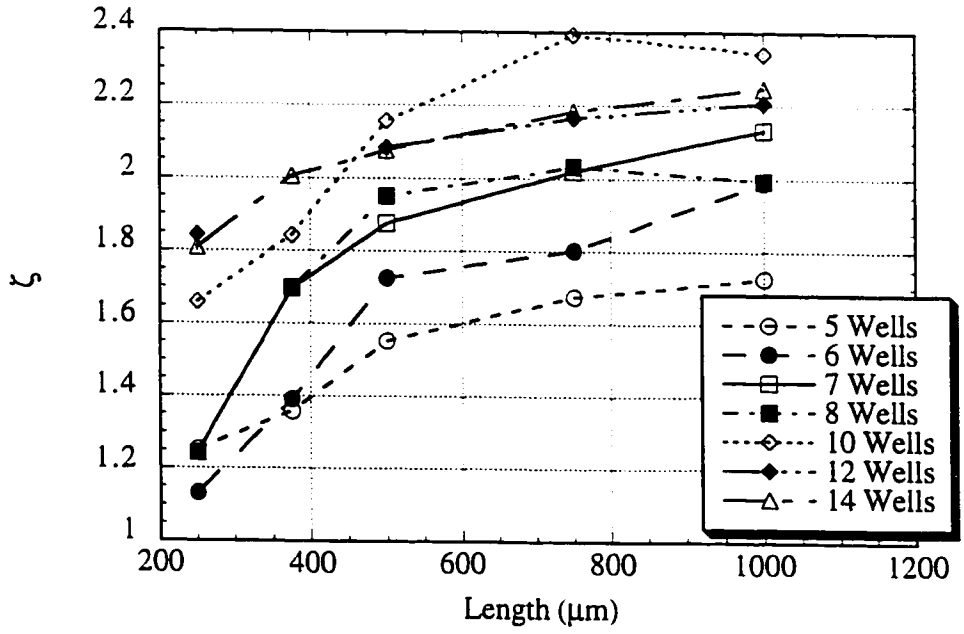

(b)

Figure 4.3 - The dependence of ζ on (a) well number and (b) length.

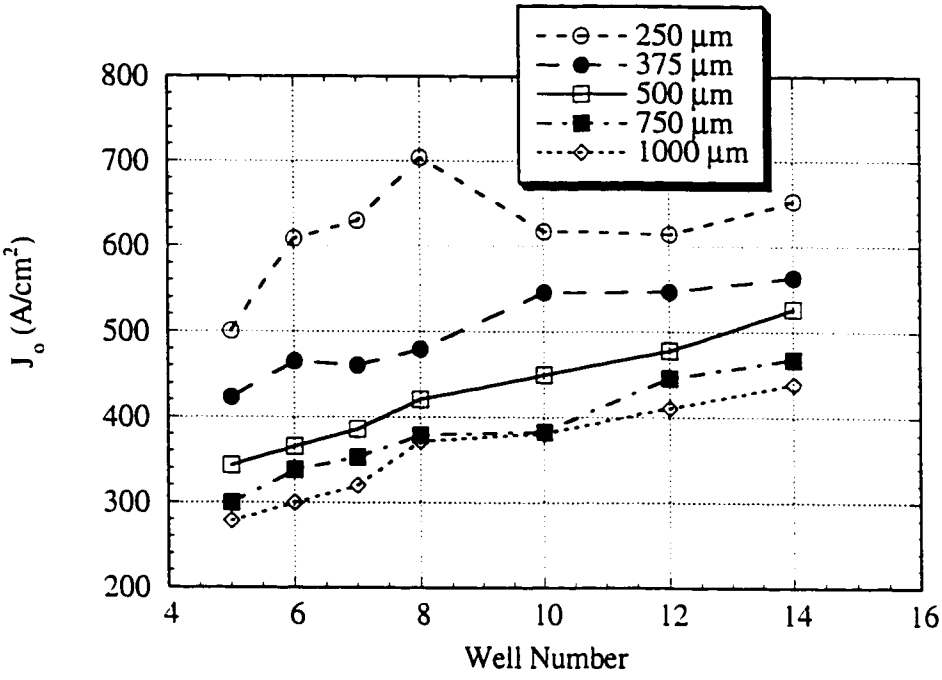

(a)

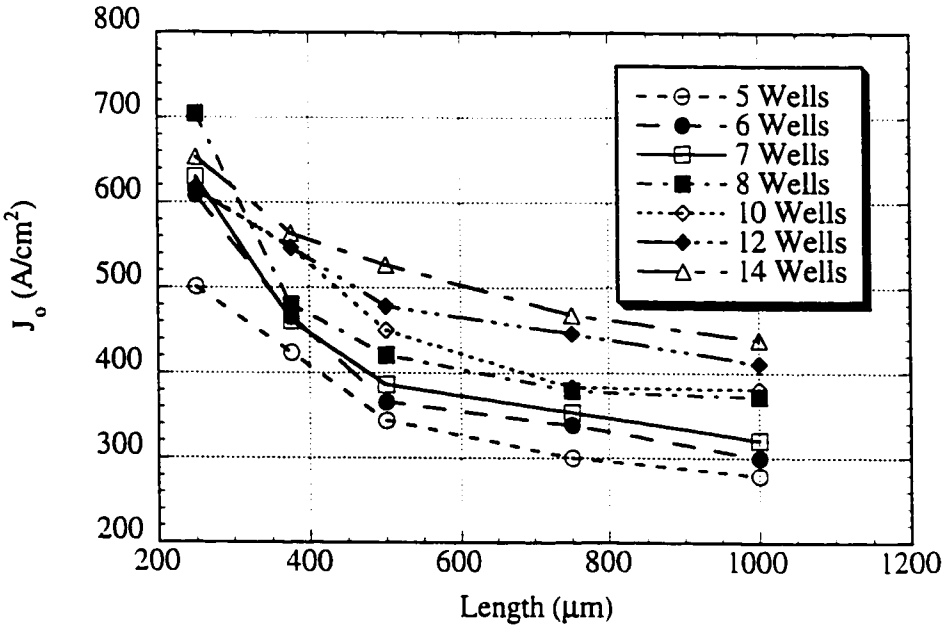

(b)

Figure 4.4 - The dependence of J_0 on (a) well number and (b) length.

The tendency of T_{max} to increase with N_W and L is not surprising since larger well numbers and lengths correspond to a lower threshold carrier density, which is usually associated with better temperature performance. In Figs. 4.3, ζ is observed to increase with increasing N_W and L, which means that, for a given T/T_{max} ratio, the temperature sensitivity increases for longer lengths and higher well numbers, in contrast to the T_{max} trend. The reason for this is discussed in Section 4.3.

Plots of J_0 as a function of well number and length are shown in Figs. 4.4. The nearly linear increase observed with well number is expected since more wells require proportionally more current density through the ridge to maintain the same level of inversion. The decrease with length can also be associated with a corresponding decrease in threshold carrier density.

4.3 DISCUSSION

In Section 3.3.1, the net modal gain of a laser at threshold (g_{th}) was written as

$$g_{th} = \Gamma\beta \ln(n_{th} / n_0) - \Gamma\gamma n_{th} - \alpha_0 = \ln(1/R)/L \quad . \tag{4.5}$$

If the carriers are not distributed evenly among the wells, the first two terms should ideally be replaced with

$$\Gamma\beta \ln(n_{th} / n_0) \rightarrow C\beta\left[\sum_{i=1}^{N} \ln(n_i / n_0)\right]_{th} ,$$
$$\Gamma\gamma n_{th} \rightarrow \Gamma\gamma \bar{n}_{th}$$

where n_i is the carrier density in the i^{th} well at threshold, and $\bar{n}_{th}$ is the average carrier density at threshold, and C is the confinement factor per well, as discussed in Chapter 3. For the sake of simplicity this step is omitted and it is recognized that the n_{th} in (4.5) is an *effective* value.

In Section 2.6, the carrier density was related to the current by [see (2.40)]

$$J_{th} = qt\left(an_{th} + bn_{th}^2 + cn_{th}^3\right) . \tag{4.6}$$

Equation (4.6) is often simplified to [5]-[7]

$$J_{th} = B_{eff} n_{th}^2 . \tag{4.7}$$

It is advantageous to maintain the simplicity of (4.7) while preserving as much as possible the accuracy of (4.6). This is done by generalizing (4.7) to the power law expression:

$$J_{th} = kn_{th}^{\xi} \tag{4.8}$$

where k and ξ are constants. Equation (4.8) has two adjustable parameters compared with one in (4.7) and, therefore, serves as a better approximation to the three-parameter description in (4.6). A detailed discussion of the influence of different values of a, b, and c on the power-law approximation, through its effect on the logarithmic gain-current density relation, is given in [8].

The value of $C\gamma n_{th}$ from the IVBA losses in (4.5) was estimated in Chapter 3 by

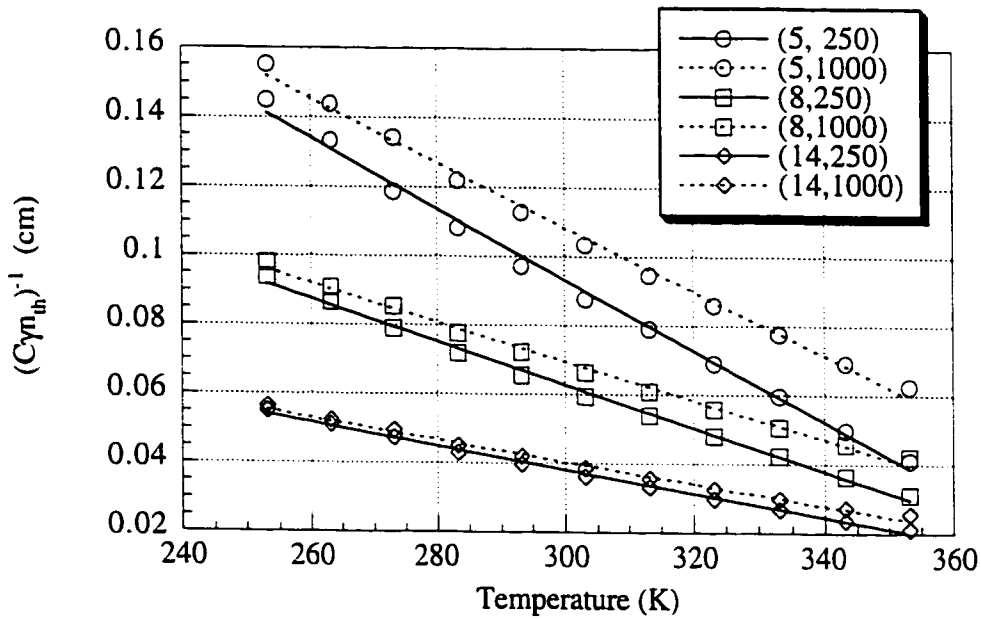

Figure 4.5 - The dependence of $(C\gamma n_{th})^{-1}$ on temperature, as measured from the differential quantum efficiency in Chapter 3. The lines are linear fits to the data.

measurement of the slope efficiency of these lasers. Figure 4.5 illustrates the temperature dependence of $(C\gamma n_{th})^{-1}$ for selected well numbers. In all cases, $(C\gamma n_{th})^{-1}$ decreases linearly with temperature, and can be described by the equation

$$(C\gamma n_{th})^{-1} = I(N_W, L) - S(N_W, L)T \tag{4.9}$$

where $I(N_W, L)$ and $S(N_W, L)$ are the intercept and slope, respectively, and depend on well number and length.

Measurements of γ have been reported and found to have only a weak temperature dependence [9]. Furthermore, changes in C from the expected temperature dispersion of the refractive indices [10] are small. It is therefore assumed that n_{th} is primarily responsible for the temperature behaviour of $(C\gamma n_{th})^{-1}$ in Fig. 4.5. By solving for n_{th} in (4.9) and substituting into (4.8), it can be shown that

$$J_{th} = k(C\gamma b)^{-\xi}\left(1 - \frac{T}{I/S}\right)^{-\xi} \tag{4.10}$$

from which the T_{max} relation (4.4) is recovered with the identities

$$J_0 = k(C\gamma b)^{-\xi}, \tag{4.11a}$$
$$T_{max} = I/S, \tag{4.11b}$$
$$\zeta = \xi. \tag{4.11c}$$

Equations (4.11) are an interesting result since they state that T_{max} is determined by the threshold carrier density given by the threshold gain condition in (4.5), while ζ is directly related to the J_{th} *vs.* n_{th} characteristic. However, direct experimental confirmation of (4.11) with the data presented here is complicated by several factors. The k and ξ parameters depend on the range over which n_{th} varies and, hence, the physical parameter (N_W, L, or T) which is being changed. In addition, the method by which an effective n_{th} may be calculated for (4.5) is different than that calculated for (4.8), so that the n_{th} appearing in (4.5) and (4.8) do not have the same meaning when the carrier density is not

uniform from well to well. In Chapter 3, fits to (4.5) were done simultaneously over all well numbers and lengths at each temperature, introducing another kind of averaging since any carrier non-uniformity at one (N_W, L) would affect all measured values of $(C\gamma n_{th})^{-1}$ at that temperature. Nevertheless, a reasonable degree of correlation is found between the ratio I/S calculated from the $(C\gamma n_{th})^{-1}$ values obtained from efficiency measurements on these devices, and the T_{max} values obtained by fits of the threshold current density to (4.4), as expected from (4.11b).

The results of the two methods are plotted together in Figs. 4.6. The measured T_{max} values for 250 μm and 375 μm devices in Fig. 4.6a agree well, differing by less than 10% from those predicted by I/S, and they display a similar well number and length dependence. Devices with longer cavity lengths have a maximum of 20% difference, as shown in Fig. 4.6b. Both the length dependence and slope of the data in Fig. 4.6b match the prediction for $N_W < 12$. However, the theoretical curves are shifted by about -25 K. We believe this systematic deviation is due to factors not included in this simple model, such as non-uniform carrier injection in the quantum wells. This idea is corroborated by the T_{max} values of the 12 and 14 well devices, which oppose the trend expected from the theoretical prediction and the rest of the experimental data. Fig. 4.7 is a plot of predicted *vs.* calculated T_{max} values indicating a correlation between the model and experiment for lower T_{max}, and increasing deviation for higher T_{max}.

It should be noted that Fig. 4.6 represents a prediction of the temperature sensitivity of the CW threshold current of these lasers over a wide range of well numbers, lengths and temperatures based on measurements of the slope efficiency. The model used is simple *and includes no adjustable parameters*. Predictions of T_0 are usually limited to small variations in device design, limited temperature ranges, and are compared to experimental data with the use of fitting parameters (see [2] for a large list of references). We believe that Fig. 4.6

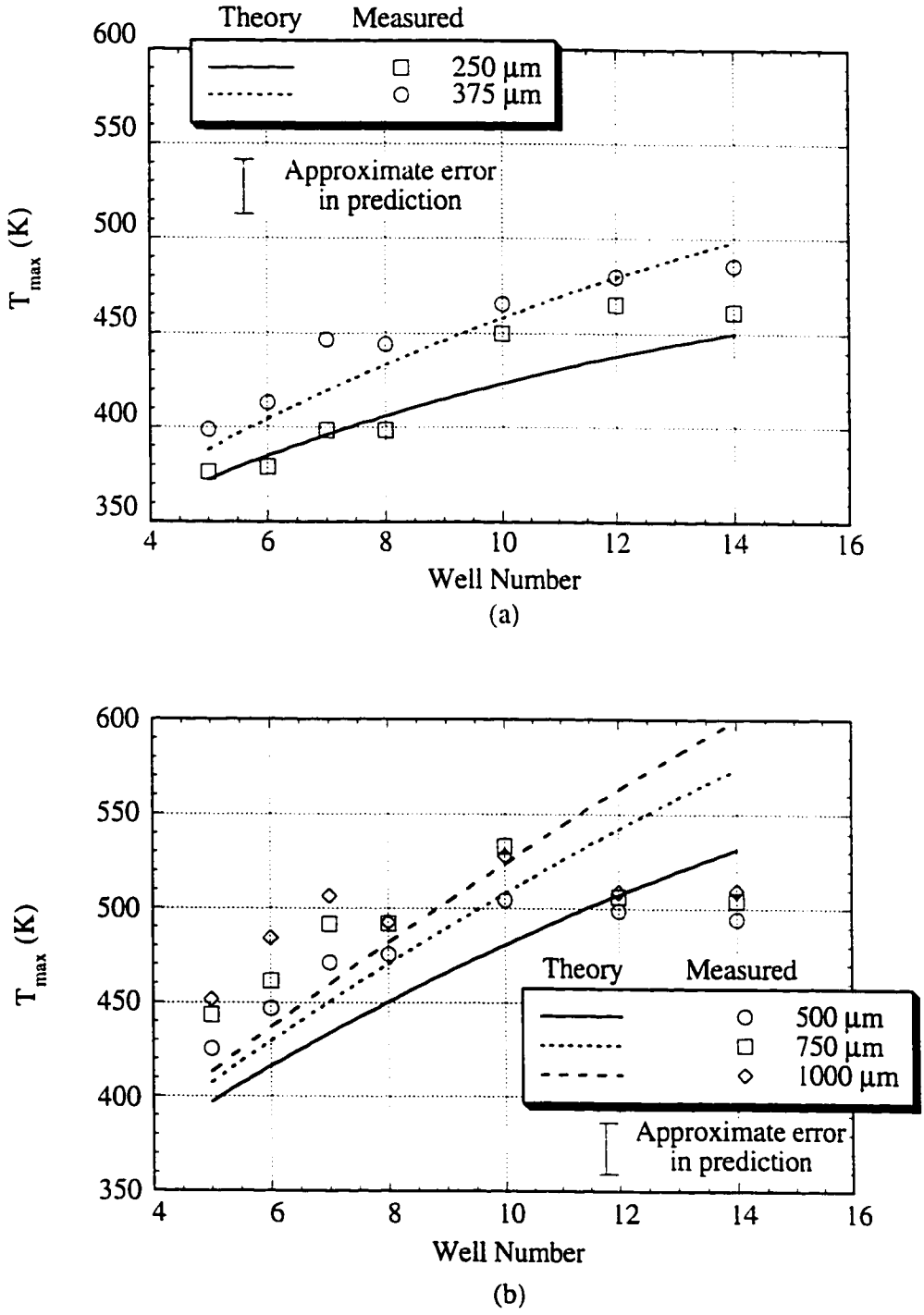

Figure 4.6 - T_{max} as a function of well number for various lengths. The lines are calculated from the I/S ratios as defined in (4.9) and the symbols are directly measured.

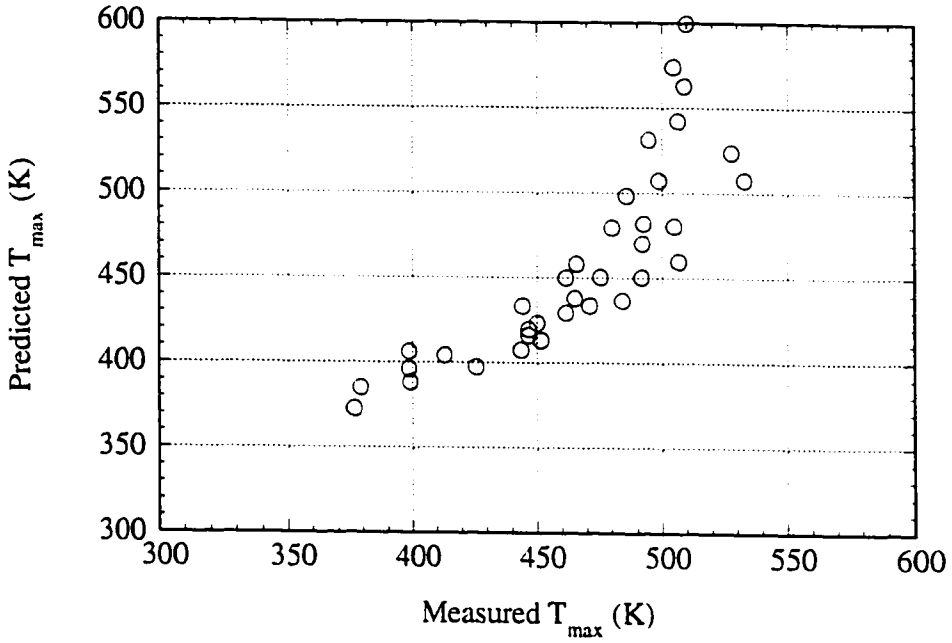

Figure 4.7 - Correlation plot between the predicted and measured values of T_{max}.

establishes a quantitative correlation between the temperature dependence of the slope efficiency and the threshold current and suggest that further investigation of the relationship, particularly with regards to the deviations noted above, may provide valuable information on the root causes of the high temperature sensitivity of InP-based lasers.

Although ζ cannot be compared to independently measured parameters in a similar fashion, it is interesting to calculate a rough typical value for ζ by matching J_{th} and $\partial J_{th} / \partial n_{th}$ at threshold for the two different expressions for J_{th} given by (4.6) and (4.8). Using $a = 2.2 \times 10^{8}$ s^{-1}, $b = 8 \times 10^{-11}$ $cm^3 s^{-1}$, $c = 1.3 \times 10^{-29}$ $cm^6 s^{-1}$, $n_{th} = 2.9 \times 10^{18}$ cm^{-3} [11] and eight quantum wells (t = 8 x 35 Å = 280 Å), a value of $\zeta = 1.80$ (and $k = 8.5 \times 10^{-7}$ $A \cdot cm^{-\zeta} \cdot cm^{-3}$) is obtained, which is in the middle of our range. It is not known how a, b, and c change with N_W and L, and reported values for these parameters vary greatly [11]-[14]. The calculated value of ζ can easily vary over the observed range of 1.1 to 2.4 for different values of n_{th} or reasonable changes in a, b, and c. The value of

$n = 1/2$ previously observed [2] corresponds to the accuracy of the simplified expression (4.7).

In terms of the threshold carrier density, ζ will change as

$$\frac{d\zeta}{dn_{th}} = \frac{b(2-\zeta) - cn_{th}(6-\zeta)}{n_{th}^2\left(a + bn_{th} + cn_{th}^2\right)} \tag{4.12}$$

which is negative for the typical values used above. This explains the observed counter-intuitive increase of ζ with N_W and L in Fig. 4.3, since the associated decrease in n_{th} increases ζ.

4.4 Chapter Summary and Conclusions

The threshold current density in strained MQW lasers has been empirically characterized while systematically varying the well number and length. In order to characterize the devices in such a way as to provide performance-related information, the T_{max} equation was used. It was found that T_{max} increased with well number and length, as would be intuitively expected, but the exponential sensitivity parameter, ζ, increased in opposition to expectations.

A carrier-density model was used to provide a phenomenological derivation of the T_{max} relation. The model gives meaning to ζ by relating it to the J_{th} *vs.* n_{th} curve, and explains the observed $n \approx 1/2$ and the changes in ζ with well number and length. T_{max} is shown to be associated with gain and losses in the laser and can be related quantitatively to the slope efficiency, establishing a connection between threshold and efficiency phenomena. The separation of gain/loss and current temperature sensitivity parameters further increases the utility of the T_{max} relation. The T_{max} relation is found to be valid as long as:

(1) n_{th}^{-1} varies linearly with temperature

(2) J_{th} varies over a small enough range that it can be adequately described by

$$J_{th} = kn_{th}^{\xi}$$

These conditions will not necessarily hold for all temperatures or for more esoteric devices. However, it is remarkable that they are valid for a temperature range as wide as 150°C (-50 to 100°C) for all the devices studied to date, including bulk lasers [2], [4].

REFERENCES

[1] K. Prosyk, J. G. Simmons, J. D. Evans, "A systematic empirical study of the well number, length, and temperature dependence of the threshold current density in InGaAsP/InP MQW lasers", *IEEE J. Quantum Electron.*, in press March 1997.

[2] J. D. Evans, J. G. Simmons, D. A. Thompson, N. Puetz, T. Makino, G. Chik, "An investigation into the temperature sensitivity of strained and unstrained multiple quantum-well, long wavelength lasers: new insight and methods of characterization", *IEEE J. Select. Top. Quantum Electron.*, vol. 1, pp. 273-283, 1995.

[3] J. A. I. Pankove, "Temperature dependence of emission efficiency and lasing threshold in laser diodes," *IEEE J. Quantum Electron.*, vol. QE-4, pp. 119-112, 1968.

[4] J. D. Evans, J. G. Simmons, "The dependence of the maximum operating temperature of long wavelength semiconductor lasers on physical and material device parameters", *IEEE Photon. Technol. Lett.*, vol. 27 no. 6, pp. 614-616, 1995.

[5] M. Asada, A. Kameyama, Y. Suematsu, "Gain and intervalence band absorption in quantum-well lasers," *IEEE J. Quantum Electron.*, vol. QE-20, pp. 745-753., 1984.

[6] P. W. A. McIlroy, A. Kurobe, Y. Uematsu, "Analysis and application of theoretical gain curves to the design of multi-quantum-well lasers," *IEEE J. Quantum Electron.*, vol. 21, pp. 1958-1963, 1985.

[7] T. Makino, "Analytical formulas for the optical gain of quantum wells," *IEEE J. Quantum Electron.*, vol. 32, pp. 493-501, 1996.

[8] T. A. DeTemple, C. M. Herzinger, "On the semiconductor laser logarithmic gain-current density relation", *IEEE J. Quantum Electron.*, vol. 29, pp. 1246-1252.

[9] D. A. Ackerman, P. A. Morton, G. E. Shtengel, M. S. Hybertsen, R. F. Kazarinov, T. Tanbun-Ek, R. A. Logan, "Analysis of T_0 in 1.3 μm multi-quantum-well and bulk active lasers", *Appl. Phys. Lett.*, vol. 62, pp. 2613-2615, 1995.

[10] G. Ghosh, "Temperature dispersion of refractive indices in semiconductors", *J.*

Appl. Phys., vol. 79, pp. 9388-9389, 1996.

[11] Y. Zou, J. S. Osinski, P. Grodzinski, P. D. Dapkus, W. C. Rideout, W. F. Sharfin, J. Schlafer, F. D. Crawford, "Experimental study of Auger recombination, gain, and temperature sensitivity of 1.5 μm compressively strained semiconductor lasers", *IEEE J. Quantum Electron.*, vol. 29 no. 6, pp. 1565-1575, 1993.

[12] G. P. Agrawal, N. Dutta, *Semiconductor Lasers*, VanNostrand-Reinhold, 1992.

[13] G. H. B. Thompson, "Analysis of radiative and non-radiative recombination law in lightly doped InGaAsP lasers", *Electron. Lett.*, vol. 19, pp. 154-155, 1983.

[14] R. Olshansky, J. LaCourse, T. Chow, W. Powazinik, "Measurement of radiative, Auger, and nonradiative currents in 1.3-μm InGaAsP buried heterostructure lasers", *Appl. Phys. Lett.*, vol. 50, pp. 310-312, 1987.

CHAPTER FIVE

GAIN AND THRESHOLD†

5.0 INTRODUCTION

IN Chapter 4, the temperature sensitivity of the threshold current was explored. Although the threshold currents for the entire parameter space of well number, length and temperature can be completely specified by $T_{max}(N_W,L)$, $\zeta(N_W,L)$ and $J_0(N_W,L)$, it is difficult to derive any physical insight or performance-related information at a specific temperature from the T_{max} of equation (4.4).

In this chapter, the influence of gain in determining threshold at room temperature (20°C) is studied in detail. The approximate logarithmic dependence of the gain on carrier density between transparency and threshold is used, as has been done in previous chapters. The logarithmic gain coefficient is determined by four independent methods: first-principles theoretical calculation; the dependence of efficiency on length and well number; the dependence of threshold current on length; and the below-threshold optical spectrum.

---

†Portions of this chapter will be submitted to [1]

The latter one is the most direct and will be used as the standard to which the others will be compared.

5.1 First Principles Calculation

The calculation of the gain coefficient in quantum well lasers first requires knowledge of the material band structure and composition. Once the mole fractions in the barrier and wells are known, the gain at the peak of the gain *vs.* wavelength curves can be calculated for a range of carrier densities. Fitting a natural logarithm to the plot of the peak gain *vs.* carrier density gives the logarithmic gain coefficient. In section 5.1.1, the method of calculating the energy levels in the quantum wells is introduced. In section 5.1.2, the band structure and composition for the devices under study are obtained. The gain coefficient is derived in section 5.1.3.

5.1.1 Carrier Energy Levels Using the Transfer Matrix Method

The quantum well energy levels of carriers in the conduction and valence bands will be calculated using the transfer matrix method (TMM) [2]. This method is widely used both for carrier wavefunctions and calculation of the optical confinement factor, which is a

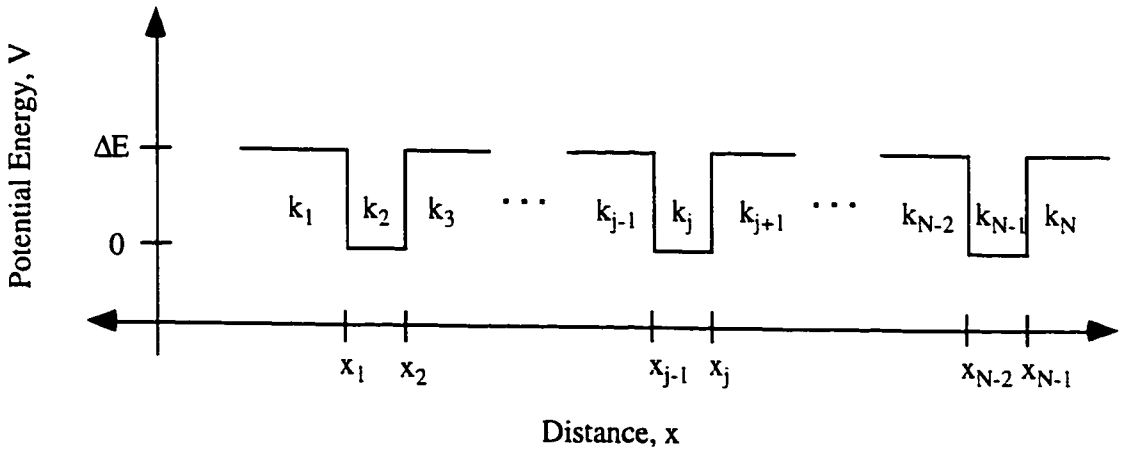

Figure 5.1 - Band diagram of N layers used in TMM calculation

similar problem. It is presented here since the elements of the transfer matrix for the carrier problem are not given explicitly in [2] and must be derived. The active region band structure is assumed to be a flat, alternating series of wells and barriers with the first and last barrier being infinite in width, as shown in Fig. 5.1. The envelope function and parabolic band approximations are employed and effective masses are used for each layer [3].

The general solution to the time-independent Schrodinger wave equation in the j^{th} section is a given by the sum of two counter-propagating waves:

$$\psi_j = A_j e^{k_j(x-x_{j-1})} + B_j e^{-k_j(x-x_{j-1})} \tag{5.1}$$

where

$$k_j = i\sqrt{\frac{2m_j}{\hbar^2}(E - V_j)},$$

$$x_0 \equiv 0,$$

x_j are the positions of the hetero-interfaces as in Fig. 5.1, m_j is the effective mass and V_j is the potential of the j^{th} section, E is the energy of the carrier, and A_j and B_j are the coefficients to be determined by boundary conditions.

At the interface between the j and j+1 sections, the following boundary conditions hold [3]:

$$\psi_j(x_j) = \psi_{j+1}(x_{j+1}) \tag{5.2a}$$

$$\left.\frac{1}{m_j}\frac{\partial\psi_j}{\partial x}\right|_{x=x_j} = \left.\frac{1}{m_{j+1}}\frac{\partial\psi_{j+1}}{\partial x}\right|_{x=x_j}. \tag{5.2b}$$

From (5.1) and (5.2),

$$A_{j+1} + B_{j+1} = A_j e^{k_j(x-x_{j-1})} + B_j e^{-k_j(x-x_{j-1})} \tag{5.3a}$$

$$A_{j+1} - B_{j+1} = A_j \frac{k_j m_{j+1}}{k_{j+1} m_j} e^{k_j(x_j - x_{j-1})} - B_j \frac{k_j m_{j+1}}{k_{j+1} m_j} e^{-k_j(x_j - x_{j-1})} . \qquad (5.3b)$$

Solving alternately for A_{j+1} and B_{j+1} in (5.3b) and substituting each in (5.3a), expressions for A_{j+1} and B_{j+1} can be obtained in terms of the coefficients of the j^{th} layer,

$$A_{j+1} = \frac{1}{2} A_j \left(1 + \frac{k_j m_{j+1}}{k_{j+1} m_j} \right) e^{k_j(x_j - x_{j-1})} + \frac{1}{2} B_j \left(1 - \frac{k_j m_{j+1}}{k_{j+1} m_j} \right) e^{-k_j(x_j - x_{j-1})} \qquad (5.4a)$$

$$B_{j+1} = \frac{1}{2} A_j \left(1 - \frac{k_j m_{j+1}}{k_{j+1} m_j} \right) e^{k_j(x_j - x_{j-1})} + \frac{1}{2} B_j \left(1 + \frac{k_j m_{j+1}}{k_{j+1} m_j} \right) e^{-k_j(x_j - x_{j-1})} . \qquad (5.4b)$$

Equations (5.4) can be expressed more conveniently in a matrix form:

$$\begin{bmatrix} A_{j+1} \\ B_{j+1} \end{bmatrix} = \hat{t}^j \begin{bmatrix} A_j \\ B_j \end{bmatrix} \qquad (5.5)$$

where $\hat{t}^j$ is the 2x2 transfer matrix of the j^{th} section. The elements of $\hat{t}^j$ are

$$\hat{t}^j = \begin{bmatrix} t_{11}^j & t_{12}^j \\ t_{21}^j & t_{22}^j \end{bmatrix}$$

$$t_{11}^j = \frac{1}{2} \left(1 + \frac{k_j m_{j+1}}{k_{j+1} m_j} \right) e^{k_j(x_j - x_{j-1})} \qquad (5.6a)$$

$$t_{12}^j = \frac{1}{2} \left(1 - \frac{k_j m_{j+1}}{k_{j+1} m_j} \right) e^{-k_j(x_j - x_{j-1})} \qquad (5.6b)$$

$$t_{21}^j = \frac{1}{2} \left(1 - \frac{k_j m_{j+1}}{k_{j+1} m_j} \right) e^{k_j(x_j - x_{j-1})} \qquad (5.6c)$$

$$t_{22}^j = \frac{1}{2} \left(1 + \frac{k_j m_{j+1}}{k_{j+1} m_j} \right) e^{-k_j(x_j - x_{j-1})} . \qquad (5.6d)$$

For bound solutions, the wavefunction must obey

$$\lim_{x \to -\infty} \{\psi_1(x)\} = 0 , \qquad (5.7a)$$

$$\lim_{x \to \infty} \{\psi_N(x)\} = 0 . \qquad (5.7b)$$

Depending on the sign of $E - V_j$, the various k_j are either purely imaginary or a negative

real number. Equations (5.7) can therefore only be satisfied when

$$A_1 = 0, \tag{5.8a}$$
$$B_N = 0 \ . \tag{5.8b}$$

and the energy, E, must be less than both V_1 and V_N.

From (5.8a) and (5.5),

$$\begin{bmatrix} A_2 \\ B_2 \end{bmatrix} = \hat{t}^1 \begin{bmatrix} 0 \\ B_1 \end{bmatrix}. \tag{5.9}$$

Repeated application of (5.5) to (5.9) gives

$$\begin{bmatrix} A_N \\ 0 \end{bmatrix} = \hat{t}^{N-1}\hat{t}^{N-2}\ldots\hat{t}^2\hat{t}^1 \begin{bmatrix} 0 \\ B_1 \end{bmatrix}$$
$$\begin{bmatrix} A_N \\ 0 \end{bmatrix} = \hat{T} \begin{bmatrix} 0 \\ B_1 \end{bmatrix} \tag{5.10}$$

where $\hat{T}$ is the total transfer matrix. Equation (5.10) can only be satisfied if

$$T_{22} = 0 \tag{5.11}$$

where T_{22} is the lower right-hand element of $\hat{T}$.

The numerical approach is now straightforward: calculate the total transfer matrix as in (5.10) by multiplying the matrices for each section given by (5.6), and keep adjusting the energy E until T_{22} vanishes. Although the elements in $\hat{t}^j$ are, in general, complex, T_{22} will always be real for bound solutions. This simplifies the algorithm since it is more efficient to search for zero crossings in T_{22} than searching for the zero minimum in $|T_{22}|$. The proof that T_{22} is real is tedious, so only a barrier-well-barrier section of the multi-layer stack is treated below. The general proof is obtained by replacing the well layer with a well-barrier-well series of layers.

Consider three layers taken out of the stack as shown in Fig. 5.2. In going from the j to the $j+2$ layer, two transfer matrices must be multiplied together,

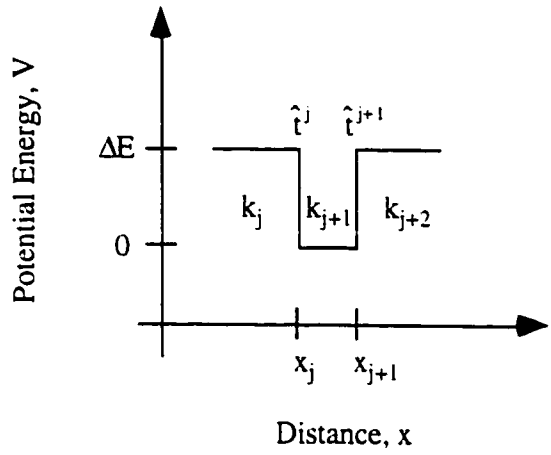

Figure 5.2 - A three-layer section of the multi-quantum-well material with propagation constants and transfer matrices between sections indicated.

$$\begin{bmatrix} A_{j+2} \\ B_{j+2} \end{bmatrix} = \hat{t}^{j+1}\hat{t}^{j} \begin{bmatrix} A_j \\ B_j \end{bmatrix}. \tag{5.12}$$

The bottom right-hand element of the combined $\hat{t}^{j+1}\hat{t}^{j}$ matrix is

$$t_{22} \equiv \left[\hat{t}^{j+1}\hat{t}^{j}\right]_{22} = t_{21}^{j+1}t_{12}^{j} + t_{22}^{j+2}t_{22}^{1} \tag{5.13}$$

which, from (5.6), can be expressed explicitly as

$$\begin{aligned} t_{22} = \frac{1}{4}\left(1 - \frac{k_{j+1}m_{j+2}}{k_{j+2}m_{j+1}} - \frac{k_j m_{j+1}}{k_{j+1}m_j} + \frac{k_j m_{j+2}}{k_{j+2}m_j}\right) e^{k_{j+1}(x_{j+1}-x_j)} e^{-k_j(x_j-x_{j-1})} \\ + \frac{1}{4}\left(1 + \frac{k_{j+1}m_{j+2}}{k_{j+2}m_{j+1}} + \frac{k_j m_{j+1}}{k_{j+1}m_j} + \frac{k_j m_{j+2}}{k_{j+2}m_j}\right) e^{-k_{j+1}(x_{j+1}-x_j)} e^{-k_j(x_j-x_{j-1})}. \end{aligned} \tag{5.14}$$

Although nothing is known about the wavefunction outside these three layers, something can be said about the propagation constants. For bound solutions, k_{j+1} is purely imaginary (see (5.1)). Similarly, k_{j+2} and k_j are real. Equation (5.14) can therefore be re-arranged as

$$t_{22} = \frac{1}{4}\left(1+\frac{k_j m_{j+1}}{k_{j+1} m_j}\right)\left(e^{k_{j+1}(x_{j+1}-x_j)} + e^{-k_{j+1}(x_{j+1}-x_j)}\right)e^{-k_j(x_j-x_{j-1})}$$
$$+\frac{1}{4}\left(\frac{k_{j+1} m_{j+2}}{k_{j+2} m_{j+1}}+\frac{k_j m_{j+1}}{k_{j+1} m_j}\right)\left(e^{k_{j+1}(x_{j+1}-x_j)} - e^{-k_{j+1}(x_{j+1}-x_j)}\right)e^{-k_j(x_j-x_{j-1})}$$
$$=\frac{1}{2}\left(1+\frac{k_j m_{j+2}}{k_{j+2} m_j}\right)\mathrm{Re}\left\{e^{k_{j+1}(x_{j+1}-x_j)}e^{-k_j(x_j-x_{j-1})}\right\}$$
$$-\frac{1}{2}i\left(\frac{k_{j+1} m_{j+2}}{k_{j+2} m_{j+1}}+\frac{k_j m_{j+1}}{k_{j+1} m_j}\right)\mathrm{Im}\left\{e^{k_{j+1}(x_{j+1}-x_j)}e^{-k_j(x_j-x_{j-1})}\right\} \qquad (5.15)$$

with the round brackets in the first term being real and the round brackets in the second term being purely imaginary, making t_{22} real.

5.1.2 Band Structure of the Devices Under Study

The band structure is calculated for the five quantum well lasers used in Chapter 3. The composition of the well and barriers is not known and must be determined from the wavelengths of the band-edge transitions. As shown in Fig. 3.1, the nominal transition wavelength of the barrier material is 1.1 μm. The nominal strain is 0.7% compressive in the wells and the lasing wavelength is 1.3 μm. This is enough information to determine the x and y mole fractions of $In_{1-x}Ga_xAs_yP_{1-y}$.

The empirically derived formula for the bandgap of a free-standing quaternary material is [4]

$$E_g(eV) = 1.35 + 0.668x - 1.068y + 0.758x^2 + 0.078y^2$$
$$-0.069xy - 0.322x^2y + 0.03xy^2 \ . \qquad (5.16)$$

Lattice constants for quaternary material can be calculated by linear interpolation from the constituent binaries. For a quaternary layer on an InP substrate with a fractional lattice mismatch of ε, the relationship between x and y is [4]

$$y = \frac{0.4182x - 5.8687\varepsilon}{0.189 + 0.0131x} \tag{5.17}$$

where ε is defined as

$$\varepsilon = \frac{a_{sub} - a}{a_{sub}},$$

a_{sub} is the substrate lattice constant, and a is the material lattice constant. Equations (5.16) and (5.17) can be used with $\varepsilon = 0$ to solve for the mole fractions in the barrier which give a transition wavelength of 1.1 μm. These are found to be $x_b = 0.14470$ and $y_b = 0.31600$.

Solving for the mole fractions in the well requires an iterative search. After guessing at an initial x_w, y_w is calculated using (5.17) with $\varepsilon = -0.007$, which corresponds to the assumed compressive strain of 0.7%. The mole fractions are then used to determine the required material parameters using the linear interpolation formula

$$Q(x,y) = xyQ_{GaAs} + x(1-y)Q_{GaP} + (1-x)yQ_{InAs} + (1-x)(1-y)Q_{InP} \tag{5.18}$$

where $Q(x,y)$ is the quantity value in the quaternary, and Q_{binary} is the quantity value of the binary.

The band discontinuities are next calculated. The components contributing to the calculation of the band discontinuities are labeled in Fig 5.3. In the presence of strain, the

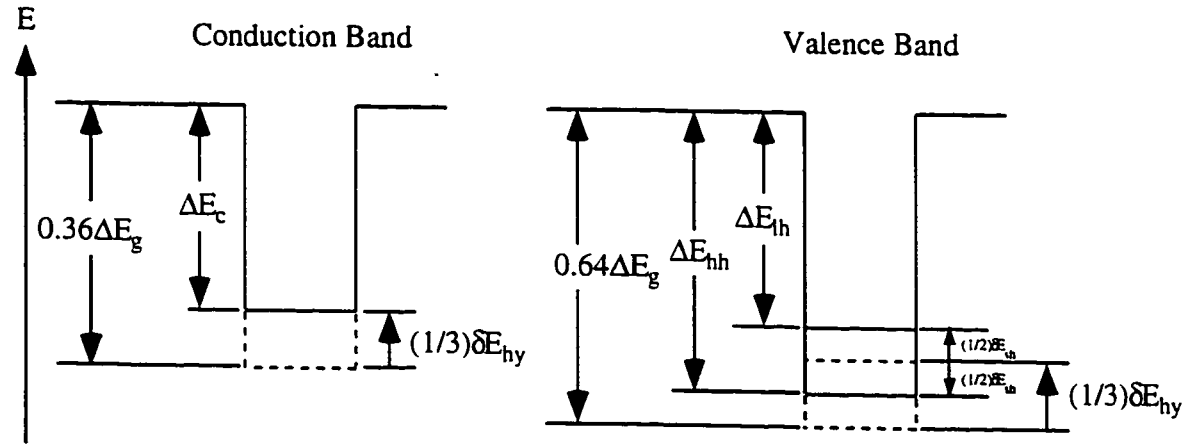

Figure 5.3 - Conduction and valence band structure in the absence of quantum size effects.

conduction (ΔE_c), heavy hole (ΔE_{lh}) and light hole (ΔE_{hh}) band discontinuities are given by [5]

$$\Delta E_c = 0.36\Delta E_g - (2/3)\delta E_{hy}\,, \tag{5.19a}$$

$$\Delta E_{hh} = 0.64\Delta E_g - (1/3)\delta E_{hy} + (1/2)\delta E_{sh}\,, \tag{5.19b}$$

$$\Delta E_{lh} = 0.64\Delta E_g - (1/3)\delta E_{hy} - (1/2)\delta E_{sh}\,. \tag{5.19c}$$

The discontinuities in the valence band are the absolute values of the differences, i. e. with the energy scale inverted. ΔE_g is the difference in bandgaps between the barrier and well material as determined by (5.16), δE_{hy} and δE_{sh} are the hydrostatic and shear contributions, respectively, and are given by

$$\delta E_{hy} = -2a^d(1 - c_{12}/c_{11})\varepsilon \tag{5.20a}$$

$$\delta E_{sh} = -2b^d(1 + 2c_{12}/c_{11})\varepsilon \tag{5.20b}$$

where a^d and b^d are the hydrostatic and shear deformation potentials, and c_{11} and c_{12} are the stiffness coefficients, the values of which can be obtained from (5.18) using the binary values listed in Table 5.1.

With the band discontinuities known, all that remains to be determined before the energy levels can be calculated are the effective masses of each of the bands in the barriers and quantum wells. The bands are assumed parabolic so that the effective masses are constant and unaffected by strain. Under such conditions, the conduction band effective mass can be determined by interpolating the binary values given in Table 5.1 with (5.18). The heavy hole and light hole effective masses are

$$m_{hh} = \frac{m_0}{\gamma_1 - 2\gamma_2} \tag{5.21a}$$

$$m_{lh} = \frac{m_0}{\gamma_1 + 2\gamma_2} \tag{5.21b}$$

where m_0 is the electron rest mass, and γ_1 and γ_2 are the Luttinger parameters and are also interpolated from binary values given in Table 5.1.

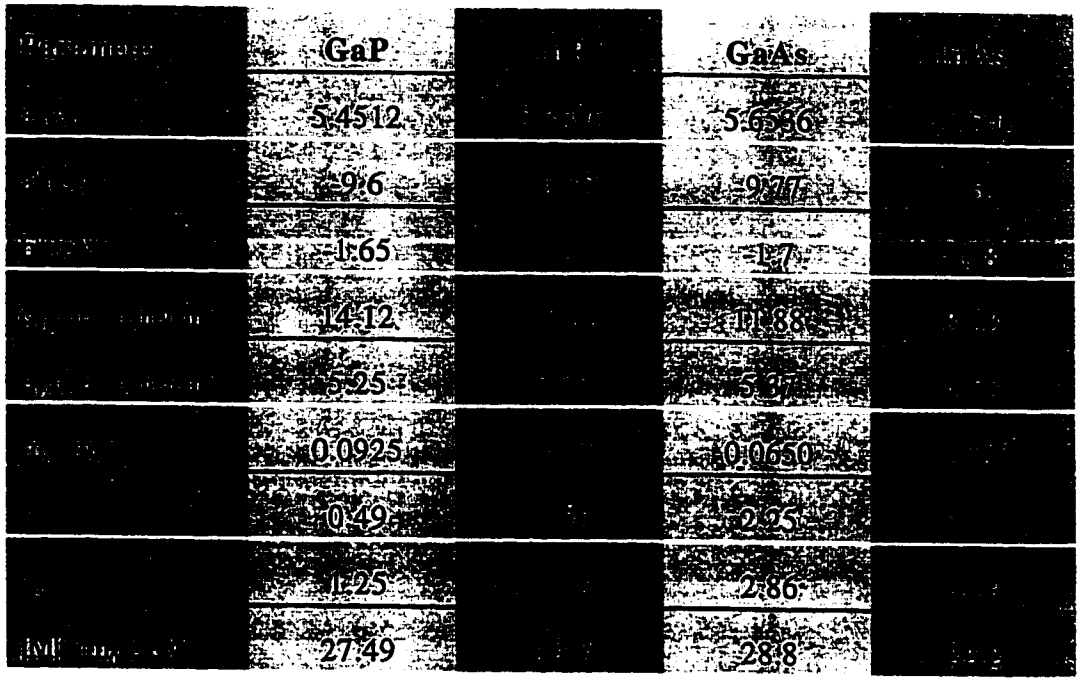

Table 5.1 - Material parameters used to interpolate quaternary values from the binaries. All values are taken from [6] except $|M|^2$ which is from [3].

The TMM of Section 5.1.1 was applied to determine the lowest quantum well energy levels in each band. Under compressive strain, the lowest level is always in the heavy hole band. The mole fraction x_w was adjusted until the energy difference between the lowest conduction band level and the lowest heavy hole level corresponded to an optical wavelength of 1.3 μm. The conduction band well was found to contain one energy level (c1), the heavy hole well had two (hh1, hh2) and the light hole had one (lh1). A slight coupling exists between the wells, causing a fine splitting of each of the levels into five sub-levels. The amount of fine splitting was so small (< 5 meV between adjacent levels in all cases) that it was ignored and the wells were approximated as being completely uncoupled. With uncoupled wells, the above analysis applies equally well to the devices with other numbers of quantum wells, 6-14. The mole fractions and energy levels are listed in Table 5.2.

Parameter	Value
x_w	0.18961
y_w	0.62667
ΔE_c	68.783 meV
ΔE_{hh}	195.19 meV
ΔE_{lh}	142.74 meV
E_{c1}	47.049 meV
c1 fine splittings	2.24, 3.60, 4.64, 4.81 meV
E_{hh1}	38.239 meV
hh1 fine splittings	< 0.01 meV
E_{lh1}	86.492 meV
lh1 fine splittings	1.49, 2.22, 2.50, 2.04 meV
E_{hh2}	141.52 meV
hh2 fine splittings	0.010, 0.014, 0.014, 0.010 meV
$\tilde{\beta}$	$19577 cm^{-1}$
ξ	0.419

Table 5.2 - Parameters calculated for the devices under study. The quantum well energy levels are measured from the bottom of the well and are the lowest level of the fine splittings. The fine splittings are the differences between levels starting from the lowest two. See Section 5.1.3 for the calculation of $\tilde{\beta}$ and ξ.

5.1.3 Theoretical Gain Coefficient

The theory of optical gain in semiconductors is well-established and will not be described here in great detail. Ref. [3] contains a good overview with other references for further reading. For the purposes of this calculation, only c1-hh1 transitions will be

considered. The overlap integral between the electron and hole wavefunctions is approximated to unity. As mentioned earlier, the parabolic band approximation is used and strict momentum conservation is invoked. With the average phase index of refraction approximated by the group index, the gain, $g(E_{eh})$, of the laser as a function of transition energy E_{eh} is [7]

$$g(E_{eh}) = \tilde{\beta} I \tag{5.22}$$

where $\tilde{\beta}$ is the magnitude of the gain in units of inverse length and I is a unitless integral determined by the carrier density that is always bounded between -1 and 1, and is referred to as the normalized gain. Explicitly, $\tilde{\beta}$ is given by [3]

$$\tilde{\beta} = \frac{\pi q^2 m_r |M|^2}{h\varepsilon_0 c m_0^2 L_w E_g' n_g} \tag{5.23}$$

where q is the electron charge, h is Planck's constant, c is the speed of light in vacuum, L_w is the width of the well, ε_0 is the permittivity of free space, m_0 is the electron rest mass, n_g is the group index, E_g' is the band-edge transition energy (in contrast to E_g, which is the energy gap between the bottoms of the conduction and valence band wells). m_r is the reduced mass, defined as

$$m_r^{-1} = m_{hh}^{-1} + m_c^{-1} \tag{5.24}$$

$|M|^2$ is the magnitude squared of the transition matrix element and is interpolated from the binary values given in Table II of ref. [3], with the exception of GaP which is calculated from the $k \cdot p$ theory in [3]. The binary values are also listed in Table 5.1. For the devices used in this study, $\tilde{\beta}$ was found to have a value of $\tilde{\beta} = 19577\ \text{cm}^{-1}$.

The integral I is given by

$$I(E_{eh}) = L(E_{eh}) \otimes \left[(f_c - f_v) E_g' / E_{eh} \right] \tag{5.25}$$

where $\otimes$ denotes convolution. $L(E_{eh})$ is a Lorentzian broadening function which is used

to account for the intraband relaxation of the carriers and is characterized by the intraband relaxation time, τ_{in}:

$$L(E_{eh}) = \frac{1}{\pi} \frac{\hbar / \tau_{in}}{E_{eh}^2 + (\hbar / \tau_{in})^2} \tag{5.26}$$

f_c and f_v are the quasi-Fermi functions for electrons in the conduction and valence bands, respectively, and are given by

$$f_{c,v} = \frac{1}{1 + e^{(E_{e,h} - E_{fc,v})/kT}} \tag{5.27}$$

where E_{fc} and E_{fv} are the quasi-Fermi levels in the conduction and valence bands, and E_e and E_h are the electron and hole energies. The energy axis for (5.27) is increasing towards the conduction band and decreasing towards the valence band.

For the purposes of this section, the quasi-Fermi levels are an intermediate step. To obtain the gain coefficient, the carrier density must be calculated. As discussed in Chapter 3, the intrinsically doped quantum wells are assumed charge-neutral, so the electron and hole densities are equal and evenly distributed among the wells. As will be seen, this assumption is not necessarily true, and may be responsible for the measurement of erroneous values for the gain coefficient when measured by the threshold method.

In calculating the carrier density, it is not clear whether only carriers in the state participating in lasing action (the c1 and hh1 bands), or if the other levels, including the unbound states above the wells, should also be included. A detailed analysis would consider all carriers for processes such as non-radiative recombination through localized defect states and Auger-assisted leakage over the hetero-barrier, but would consider radiative recombination primarily from the c1 and hh1 bands. Such an analysis is beyond the scope of this thesis. However, since measurements of the A, B, and C coefficients (see Chapter 4) relating the carrier density to current include all states, the same is done in this

calculation. In practice, the difference in the gain coefficient including all states and only c1 and hh1 states is within the error due to assumptions and accuracy in material parameters, about 9%.

The electron density in the conduction band is given by the sum of carriers in c1 and those above the well:

$$n = \int_{E_{c1}}^{\infty} D_{WC} f_c(E) dE + \int_{E_{tc}}^{\infty} D_{BC} f_c(E) dE \tag{5.28}$$

where E_{c1} is energy of the bottom of the quantum well subband, E_{tc} is the energy of the top of the quantum well, and D_{WC} and D_{BC} are the 2-d density of states in the well and the 3-d density of states above the well:

$$D_{WC} = \frac{m_c}{\pi \hbar^2 L_w} , \tag{5.29a}$$

$$D_{BC} = \frac{1}{2\pi^2}\left(\frac{2m_c}{\hbar^2}\right)^{3/2} \sqrt{E - E_{tc}} . \tag{5.29b}$$

The first integral in (5.28) can be evaluated in closed form, the second requires numerical integration. Equation (5.28) can be re-written as

$$n = kTD_{WC} \ln\left(1 + e^{(E_{fc} - E_{c1})/kT}\right) + \frac{1}{2\pi^2}\left(\frac{2m_c}{\hbar^2}\right)^{3/2} \int_0^{\infty} \frac{\sqrt{x}dx}{1 + e^{(E_{tc} - E_{fc})/kT} e^x} . \tag{5.30}$$

The valence band quasi-Fermi level can be similarly related to the carrier density. The hh1, lh1 and hh2 bands must all be accounted for, in addition to the unbound states above the well:

$$n = p = \sum_i \int_{E_i}^{\infty} D_{Wi} f_v(E) dE + \int_{E_{tv}}^{\infty} D_{BV} f_v(E) dE \tag{5.31}$$

where $i = hh1, lh1, hh2$ and the densities of states can be obtained from (5.29) by replacing m_c with the appropriate effective mass and E_{tc} with E_{tv}. In using (5.29b) and (5.31) for the valence band, the energy scale must be inverted, i. e. the energy at the

bottom of the valence band quantum well is lower than the top.

Using (5.25)-(5.31), plots of the normalized peak gain, I, as a function of carrier density, $I_p(n)$, can be obtained by choosing a carrier density, searching for the corresponding quasi-Fermi levels, calculating I as a function of E_{eh}, and identifying the maximum. Above transparency ($I_p(n) > 0$), the curve is well described by a logarithm, as shown in Fig. 5.4,

$$I_p(n) = \xi \ln(n / n_0) \ . \tag{5.32}$$

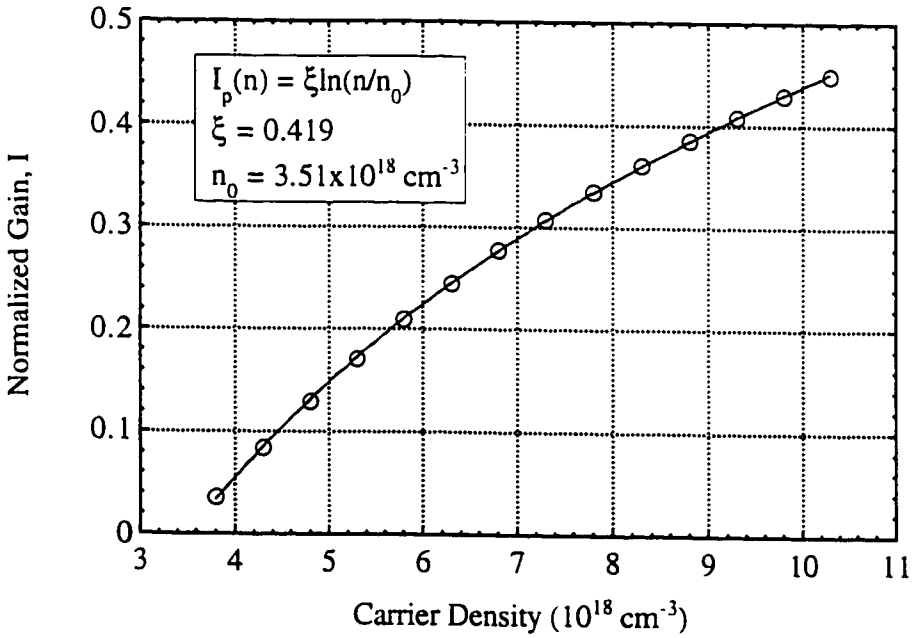

Figure 5.4 - Theoretical calculation of the normalized gain, I, as a function of carrier density. The open circles are the calculated points, the solid line is a logarithmic fit to the points.

5.2 EFFICIENCY CALCULATION

In Chapter 3, the variation in slope efficiency with well number was described by a model based on inter-valence band absorption (IVBA). Although the model provided an

economical explanation for the observed behaviour, it could not be considered as having been proven. Results from Chapter 3 were used in Chapter 4 in calculating the temperature sensitivity of the threshold current. The calculation was found to correlate with experimental data, particularly for low well numbers.

The gain in the quantum wells, B, in Chapter 2 was given by

$$B = \Gamma\beta \ln(n / n_0). \tag{5.33}$$

By calculating the optical confinement factor and using the data in Chapter 3, it was found that $\beta = 8900 \pm 1300\ \mathrm{cm}^{-1}$ at 20°C. The theoretical value calculated from the previous section is $\beta = \tilde{\beta}\xi = 8204\ \mathrm{cm}^{-1}$, using $\tilde{\beta} = 19577\ \mathrm{cm}^{-1}$ and $\xi = 0.419$. The efficiency value is in reasonable agreement with theory, further validating the model of Chapter 3. The calculation of Γ could be a significant contributor to the difference, since carrier filling of the bands, internal temperature variations, and gain guiding were not accounted for. Uncertainties in the values of the material parameters used to calculate the gain are also a possible culprit. Even if these problems were eliminated, however, a difference may still exist due to non-uniform filling of the quantum wells, as will be discussed in Section 5.5.

It has been suggested that IVBA may have an impact on the effective gain coefficient [7]. This can easily be calculated using the expression for the net gain, (2.39),

$$g = \Gamma\beta \ln(n / n_0) - \Gamma\gamma n_0 (n / n_0) - \alpha_0 \tag{5.34}$$

with $\beta = 8900\ \mathrm{cm}^{-1}$, $\gamma n_0 = 333\ \mathrm{cm}^{-1}$ and $\alpha_0 = 1.6\ \mathrm{cm}^{-1}$ from the 20°C measurements in Chapter 3. Figure 5.5 is a comparison of net modal gain, g, with the gain term $\Gamma\beta \ln(n / n_0)$ as a function of n / n_0 for 5 and 14 wells. Despite the presence of linear and constant terms in (5.34), g still maintains a logarithmic shape. The gain coefficient when IVBA and α_0 are included is $8470\ \mathrm{cm}^{-1}$ for both 5 and 14 wells, with the differences in magnitude in Fig 5.5 caused by the change in Γ for the different well numbers. Therefore

IVBA has only a small effect on the gain coefficient and, furthermore, is essentially independent of well number.

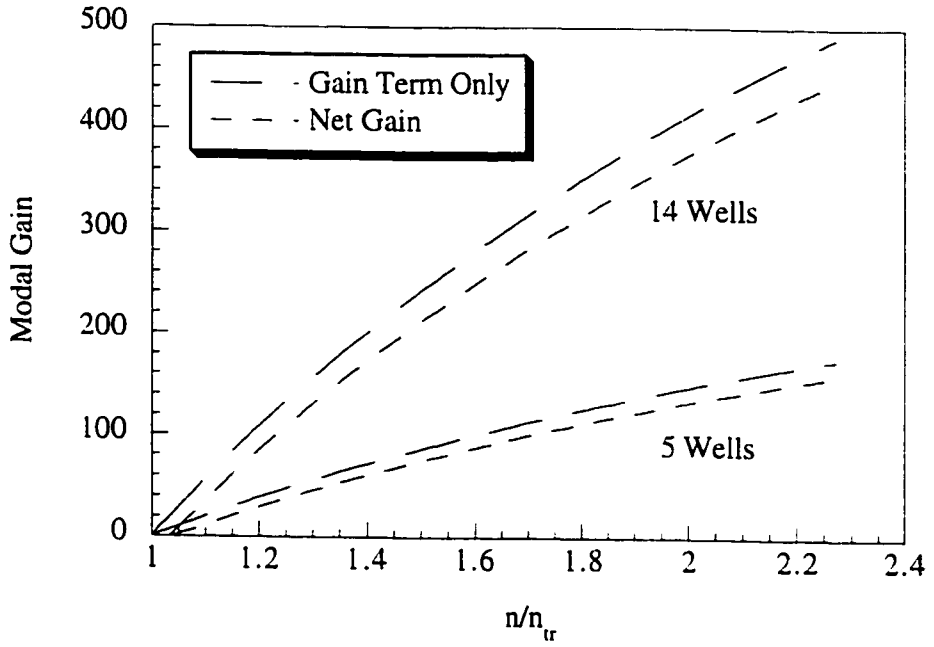

Figure 5.5 - Gain and net gain for the optical mode for 5 and 14 quantum wells. The dots represent the calculated points and the dashed lines are logarithmic fits. The logarithmic gain coefficient for both well numbers is 8900 cm^{-1} when only QW gain is considered and 8470 cm^{-1} when IVBA and residual losses are included. The transparency carrier density is modified by a factor of 1.04 for 5 wells and 1.03 for 14 wells.

5.3 THRESHOLD CALCULATION

One of the simplest and most commonly used methods of inferring the gain coefficient is by examining the length dependence of the threshold current density. The logarithmic dependence of the net gain on carrier density is written

$$g = \Gamma\beta \ln(n / n_{tr}) \tag{5.35}$$

where β and n_{tr} includes the effects of IVBA and residual losses, and, using the threshold condition

$$g_{th} = \ln(1/R)/L\ , \tag{5.36}$$

(5.34) can be re-written

$$n_{th} = n_{tr}\exp\left\{\frac{\ln(1/R)}{\Gamma\beta L}\right\}. \tag{5.37}$$

To relate carrier density to current density, the approximate relationship of Chapter 4 can be used,

$$J = L_W N_W k' n^{\zeta}\ . \tag{5.38}$$

The thickness of the active region, $L_W N_W$, has been written explicitly in (5.38)

Substitution of (5.37) into (5.38) gives

$$J_{th} = N_w J_{tr}\exp\left\{\frac{\ln(1/R)}{\Gamma G_0 L}\right\} \tag{5.39}$$

where

$$J_{tr} = L_W k' n_{tr}^{\zeta}\ ,$$
$$G_0 = \beta/\zeta\ .$$

By plotting J_{th} as a function of L and assuming a value for R, ΓG_0 can be obtained. The gain coefficient of the current density, G_0, ultimately determines the threshold performance of the laser, and is more useful as a figure of merit than β. Values will therefore be compared by converting β to G_0 by assuming $\zeta = 2$, rather than the other way around.

Figure 5.6 contains a plot of the threshold current density as a function of length for the 5 quantum well devices. From a least squares fit to (5.39), it is found that

$$\Gamma G_0 = 47.5 \pm 1.1\ \mathrm{cm}^{-1} \quad \text{(threshold current method).}$$

The corresponding values from theory and efficiency are

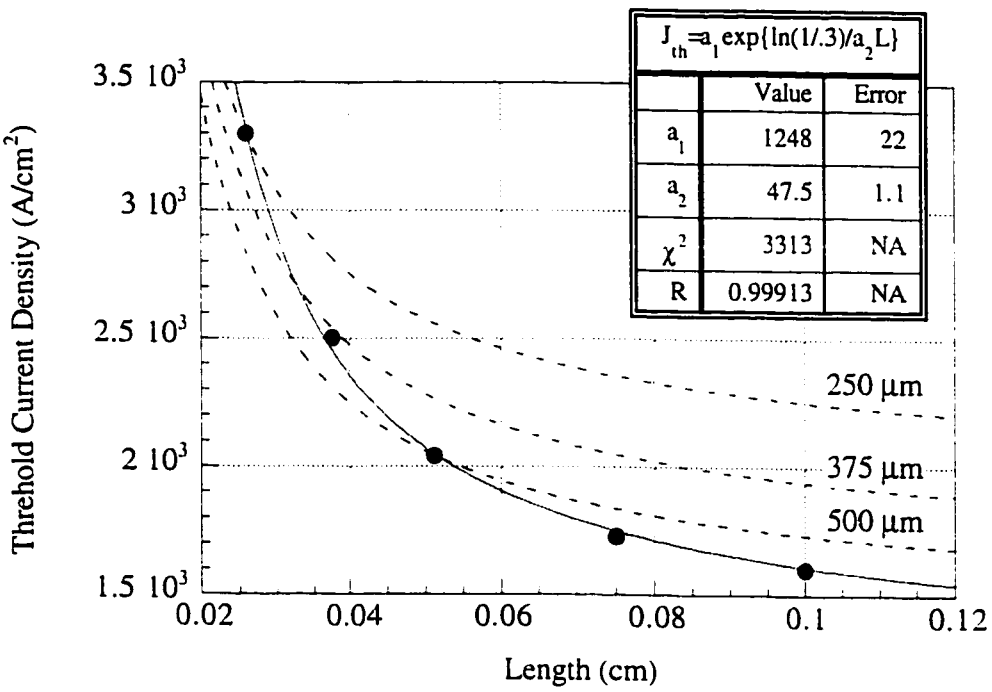

Figure 5.6 - Threshold current density as a function of length (dots) used to obtain the gain coefficient (fitting parameter a_2) and transparency current density (fitting parameter a_1). The fit is given by the solid line. The dashed lines indicate the J_{th} values expected from the direct gain measurements in Section 5.4.3. The χ^2 and correlation factor R for the fit are also shown.

$$\Gamma G_0 = \Gamma\tilde{\beta}\xi / \zeta$$
$$= 0.0048 \cdot 5 \cdot 19577 \cdot 0.419 \cdot 0.952 / 2$$
$$= 93.7\ \mathrm{cm}^{-1} \quad \text{(theoretical calculation)},$$

$$\Gamma G_0 = \Gamma\beta / \zeta$$
$$= 5 \cdot 0.0048 \cdot 8470 / 2$$
$$= 102 \pm 15\ \mathrm{cm}^{-1} \quad \text{(efficiency method)}.$$

The extra factor of 0.952 in the theoretical calculation accounts for the reduction of the gain coefficient due to IVBA, as calculated from efficiency measurements in Section 5.2. The β used for the efficiency value includes IVBA.

It is evident from the above that the threshold current value of $\Gamma G_0 = 47.5 \pm 1.1\ \mathrm{cm}^{-1}$ is significantly lower than the others, differing by a factor of about

1/2. This cannot be accounted for by altering ζ in the theoretical calculation, since even a rather high value such as $\zeta = 2.5$ still gives $\Gamma G_0 = 75\,\mathrm{cm}^{-1}$, a significant difference. Similar discrepancies have been noted in the literature [7], [8]. It is desirable to discover the cause of the difference since it might lead to reduced threshold currents.

5.4 DIRECT MEASUREMENT

In order to reach an understanding of the discrepancy between the gain coefficient obtained through the threshold method and those that were calculated theoretically and inferred from the slope efficiency, below-threshold spectral measurements were undertaken to measure the gain as a function of current density. It was discovered that both the gain coefficient and the transparency current density have a significant length dependence which gives misleading results when using the threshold method. In section 5.4.1 the experimental details are given, in section 5.4.2 the method of analysis is given, and in section 5.4.3 the results are presented and discussed.

5.4.1 Experimental Details

The lasers were placed on a copper stage thermally stabilized by a thermo-electric cooler. Light from the laser output was collected, chopped and coupled into a 1/2-metre double-pass monochromator. The monochromator output was imaged onto an InGaAs detector connected to a lock-in amplifier which used the chopper signal as a reference. The monochromator was scanned over a range of wavelengths with a step size typically on the order of 0.08 Å for various laser drive currents. A computer was used to drive all mechanical and electrical components and to collect and record the signal from the lock-in amplifier.

The lens system was designed to minimize the reflection of emitted light back in to

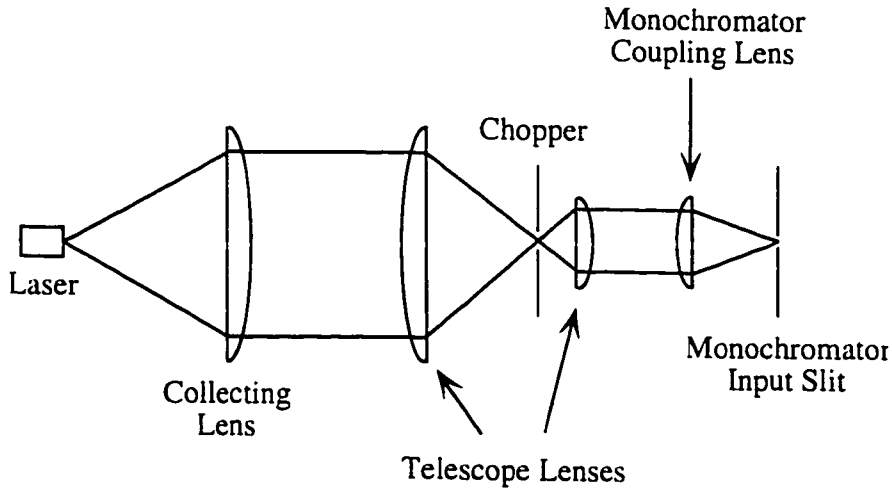

Figure 5.7 - Schematic representation of the optical system used to couple light from the laser into the monochromator.

the laser, which could cause a modification of the free-running spectrum, and yet still collect a significant portion of the light. A schematic diagram of the lenses is given in Fig. 5.7. All lenses were anti-reflection coated for 1.3 μm wavelength. The collecting lens was chosen to have a 50.8 mm diameter and a 62.9 mm focal length. An effort was made to reduce the amount of spherically aberrant light entering the monochromator. An iris aperture was placed between the laser and the first collecting lens to reduce the cone of light entering the lens system. It was discovered through experimentation, however, that the aperture was unnecessary when the monochromator entrance slit was closed to a narrow enough width (< 10 μm).

The second and third lenses along the beam path form a Galilean telescope system. Aside from creating a small beam spot for chopping at the focal point, the width of the collimated beam is reduced to less than half the original width. This is useful both for reducing spherical aberration and introducing additional degrees of freedom permitting the fine adjustment of the beam diameter striking the final lens. In this manner, optimal filling of the monochromator grating is ensured. The final lens focuses the beam on the

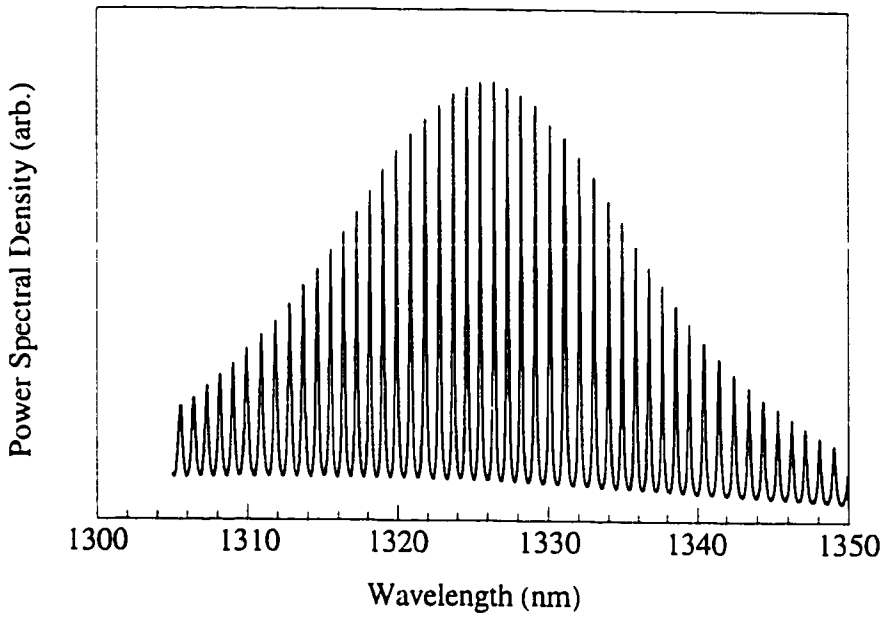

Figure 5.8 - Sample spectrum of a 5 well, 250 μm laser.

monochromator entrance slit.

5.4.2 Method of Analysis [9]

A sample of the Fabry-Perot spectrum of a 5 well, 250 μm laser is given in Fig. 5.8. The drive current is such that the single-pass gain (as defined in Chapter 2) is approximately $RG = 0.5$. Note the similarity between this spectrum and the theoretical spectrum in Fig. 2.7. To obtain the gain, the ratio, p, between the integrated power in each mode (from minimum to minimum) and the average of the minima on either side is calculated. From Chapter 2 (equation (2.17)) the output spectral density for a symmetric laser is

$$P_{out}(\nu) = \frac{\gamma_{sp} u_{sp}}{2g} \frac{(1-R)(1+RG)(G-1)}{\left[(1-RG)^2 + 4RG\sin^2(\theta)\right]} \tag{5.40}$$

where $\theta = \pi\nu / \nu_{FSR}$. All variables have the same meaning as in Chapter 2, and G, g, and

$\gamma_{sp}u_{sp}$ have an implicit frequency dependence which is considered small over the span of one mode. The minima of mode m occur when $\theta = (m \pm 1/2)\pi$, so that

$$P_{min,m} = \frac{\gamma_{sp}u_{sp,m}}{2g_m}\frac{(1-R)(G_m-1)}{(1+RG_m)} \quad . \tag{5.41}$$

The total power in each mode is given by integrating (5.40) with respect to frequency over one mode ($\theta = -\pi/2 \rightarrow \pi/2$). This is given by (2.31) as

$$P_{sum,m} = \frac{\gamma_{sp}u_{sp,m}}{2g_m}\frac{(1-R)(G_m-1)}{(1-RG_m)} \quad . \tag{5.42}$$

Therefore, the ratio is

$$\begin{aligned} p_m &= P_{sum,m} / P_{min,m} \\ &= \frac{1+RG_m}{1-RG_m} \end{aligned} \tag{5.43}$$

or, if the ratio is known, RG_m is given by

$$RG_m = \frac{p_m - 1}{p_m + 1} \quad . \tag{5.44}$$

The calculation of the gain of each mode can be accomplished by numerically integrating the measured spectrum and dividing by the average of the minimum on each side of the mode to determine p_m. Equation (5.44) can then be used to obtain RG_m.

A further refinement is required to account for the finite resolution of the monochromator. Although the total power in one mode is constant, it will be convolved with the response function of the monochromator. Power from the centre of the mode will be shifted to the edges, increasing the minima. This can be corrected for by Taylor expanding (5.40) about a minimum, to obtain the factor, F, by which it is increased [9]:

$$F = \left\{1 + \frac{4RG}{(1+RG)^2}\left[\sigma^2 + \sigma^4\left(\frac{4RG}{(1+RG)^2} - \frac{1}{3}\right)\right]\right\} \tag{5.45}$$

where σ^2 and σ^4 are the second and fourth moments of the response function, respectively. Multiplying $P_{min,m}$ by F^{-1} will give the true value of RG when substituted into (5.44). However, since the RG in (5.45) is also the true value, the correction must be applied iteratively until it converges.

It is usually beneficial to average over several points at the minimum to reduce the random error in $P_{min,m}$. Averaging is equivalent to convolving a box function the same size as the averaging window with the spectrum. The systematic error due to averaging can be corrected by convolving the box function with the monochromator response function before calculating the moments for (5.45).

The monochromator response function was measured by biasing the laser above threshold. Since the width of the lasing mode will be much less than the response function, the spectrum of the mode will actually be the response function (i. e. - the response function is effectively convolved with a delta-function at the centre of the mode). The response function was measured each time a laser was placed in the measurement apparatus, since the exact response function is alignment-dependent.

As the cavity length of the laser increases, the free spectral range, $\nu_{FSR} = c / 2n_g L$, decreases and the effect of the monochromator response function becomes more severe. As higher order terms than those given in (5.45) become significant, the iterative correction will not converge to the actual value of RG. In order to quantify the expected error, a typical response function was convolved with theoretical spectra having $RG = 0...1$. The mode sum/min method discussed above was then applied and the resulting RG was compared to the original value. Figure 5.9 is a plot of the error as a function of RG for various cavity lengths. Based on this plot, it is concluded that only lasers with $L \leq 500\mu m$ incurred acceptable errors.

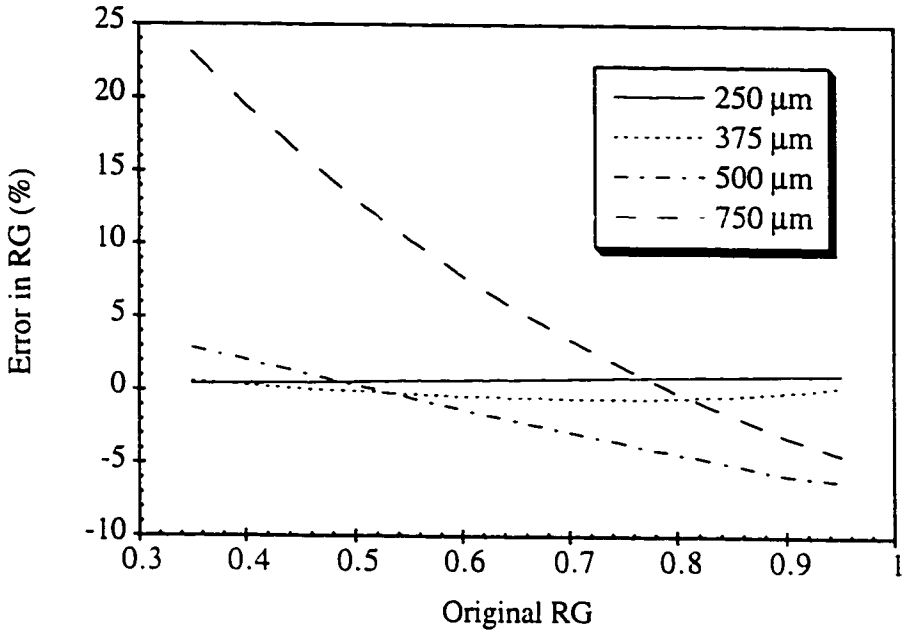

Figure 5.9 - Expected percentage error in RG measurements as a function of the actual RG value for various cavity lengths.

5.4.3 Results and Discussion

According to the standard theory used to derive (5.39) for the threshold current density, a single gain curve parameterized by $N_W J_{tr}$ and ΓG_0 will apply to lasers that have varying length but are otherwise identical. The threshold current density varies because the position of the mirror loss line, $\alpha_m = \ln(1/R)/L$, changes with L, as depicted in Fig. 5.10. Therefore, direct measurement of the g *vs.* J for devices with varying length should yield curves that are collinear, merely saturating at different threshold gain values (see Chapter 2 for a discussion of gain saturation).

Figure 5.11 is a plot of the experimentally measured gain curves for the 5 quantum well structure in Chapter 3 at a heat sink temperature of 20°C, for cavity lengths of 250, 375, and 500 µm. It is evident that the curves have a significant dependence on length. In

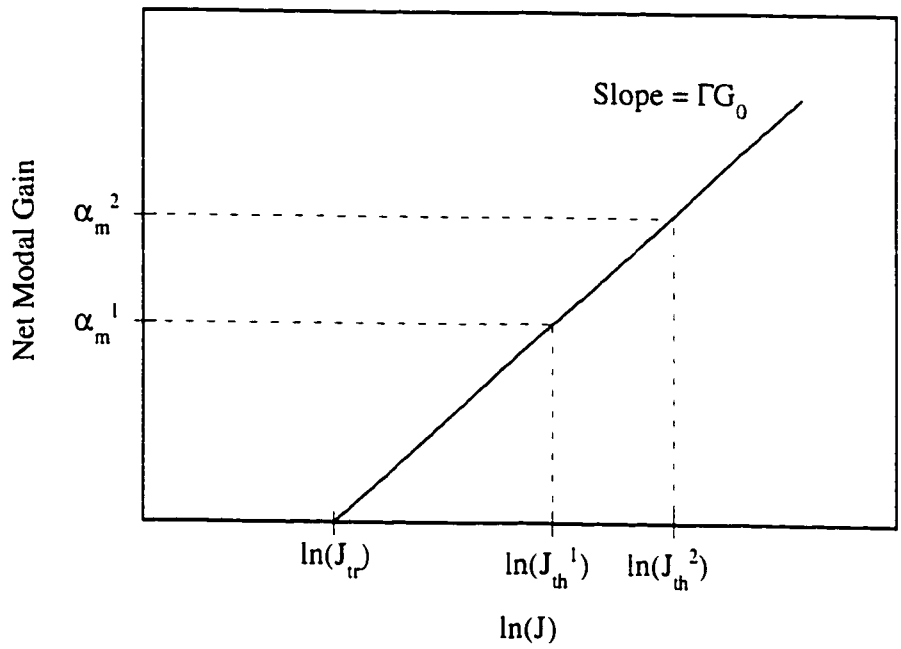

Figure 5.10 - Schematic diagram of the theoretically expected gain as a function of the logarithm of the current density for two identical laser structures of different length. The mirror loss, $\alpha_m = \ln(1/R)/L$ changes, giving rise to changes in J_{th}.

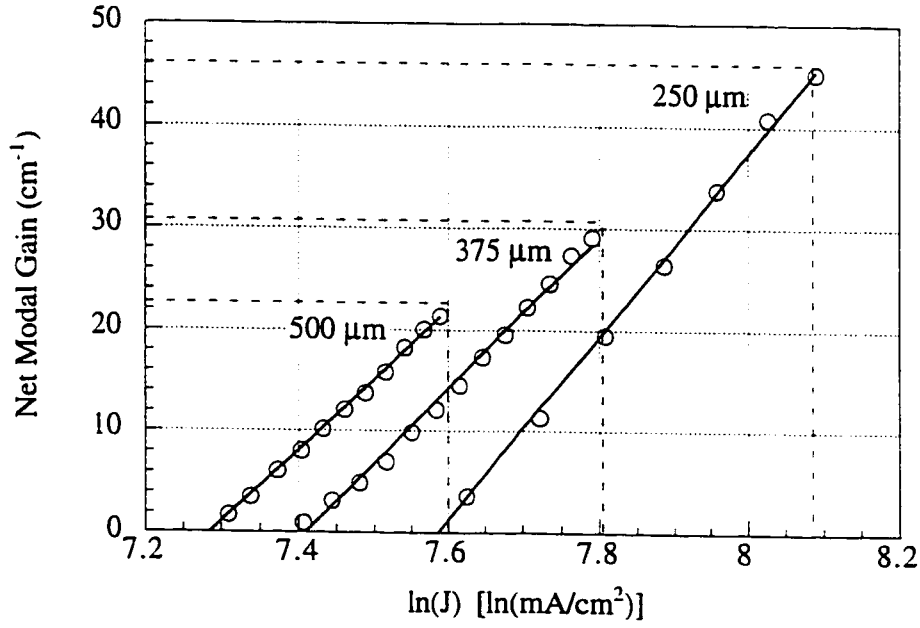

Figure 5.11 - Experimentally determined modal gain as a function of the logarithm of the current density for the 5 quantum well devices and three different cavity lengths. The dashed lines indicate threshold.

Device Length	$N_W J_{tr}$ (A / cm^2)	ΓG_0 (cm^{-1})
250 μm	1970 ± 10	90.1 ± 1.5
375 μm	1650 ± 8	74.4 ± 1.6
500 μm	1459 ± 3	69.9 ± 1.0
J_{th} all lengths (Fig. 5.6)	1248 ± 22	47.5 ± 1.1

Table 5.3 - Summary of gain coefficient and transparency current density values measured directly, as well as those inferred from the threshold current density of all lengths.

addition to a change in the gain coefficient ΓG_0, a large change in the transparency current density can be seen. An interesting feature of Fig. 5.12 is that ΓG_0 decreases with length (i. e., it gets worse), while $N_W J_{tr}$ also decreases with length (i. e., it gets better). It is not clear whether this is the result of two independent mechanisms at work, one which affects the gain and one which affects the transparency current density, or whether a single mechanism is invalidating one or more of the assumptions used to derive (5.39). The gain coefficient for the 250 μm device is

$$\Gamma G_0 = 90.1 \pm 1.5 \text{ cm}^{-1} \qquad \text{(direct measurement)}$$

which compares favourably to the theoretical calculation and the efficiency method in Section 5.3. The values for the gain coefficient and transparency current density for the devices measured are given in Table 5.3

To further illustrate the effect of the varying parameters, a hypothetical J_{th} *vs.* L curve was calculated for the ΓG_0 and $N_W J_{tr}$ of each device using (5.39). The results are shown as dashed lines in Fig. 5.6. It is surprising that even though the shape of the gain curve changes with length, the same form of J_{th} *vs.* L curve expected from (5.39) is still obtained, albeit with different parametric values. The parameters ΓG_0 and $N_W J_{tr}$ are plotted as a function of length in Fig. 5.12. It is evident that both quantities change with L in a similar manner. A function with an exponentiated reciprocal of L like (5.39) can be used to describe the behaviour. Note that the fitting parameter a_2 has a value much closer

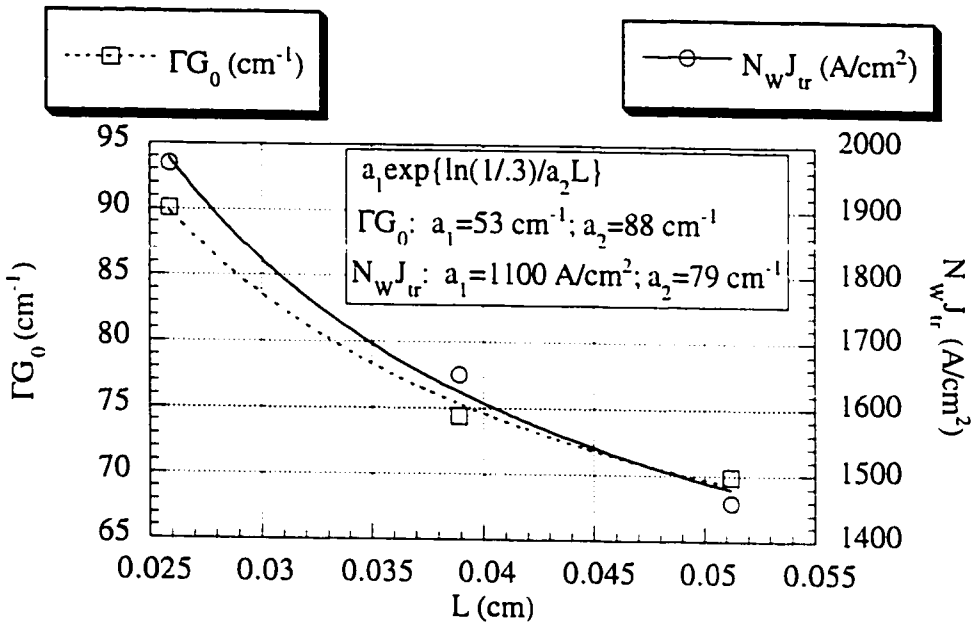

Fig. 5.13 - Directly measured gain coefficient and transparency current density as a function of length. The two quantities decrease with length in a manner similar to that expected from the threshold current density.

to that calculated theoretically for ΓG_0. The error in the fits are not shown since two fitting parameters were used for only three points.

One possible mechanism for the observed changes in the gain curve with length is a change in the internal junction temperature of the laser. Although the heat sink was maintained at 20°C, resistive heating due to current passing through the device can raise the crystal temperature in the active region. Not only will different lengths have different current densities, the change in physical dimensions may have an effect on the rate at which heat is dissipated. An estimate of the temperature change for a unit change of the current density was obtained experimentally.

When a laser is biased above threshold, one mode usually dominates in power, as discussed in Section 2.5. In the absence of crystal defects, this will be the mode closest to the wavelength peak of the gain curve. The position of the gain peak is a function of the

material composition, structure, carrier density, and crystal temperature. Since the carrier density is essentially clamped above threshold, the only factor which changes is crystal temperature. As the drive current is increased, the dominant mode, m_0, is observed to decrease in power and the mode next to it on the long wavelength side, m_1, increases. At some point, this mode peaks in power and begins to decrease while mode m_2 starts to increase.

A similar effect is observed if the current is held constant and the heat sink temperature is adjusted, with an increase in temperature corresponding to a similar red shift in the gain peak. Therefore, the temperature change per unit change in current density, dT / dJ, can be estimated as follows. The laser is biased above threshold with the heat sink temperature at 20°C at a point where m_0 has peaked in power. The change in current required for the m_2 mode to peak (ΔI) is recorded, and the wavelength difference between m_0 and m_2 ($\Delta\lambda$) is also noted. The wavelength change per unit current is thus approximated by

$$\frac{\partial\lambda}{\partial I} \approx \frac{\Delta\lambda}{\Delta I} .$$

The change in temperature (ΔT) required to shift the gain peak from m_1 to m_2 is obtained by biasing the laser at the original current and slowly incrementing the heat sink temperature. Note that $\Delta\lambda$ must be re-recorded since the wavelengths of the modes shift slightly with temperature. The change in temperature per unit wavelength is approximated by

$$\frac{\partial T}{\partial\lambda} \approx \frac{\Delta T}{\Delta\lambda} .$$

Assuming that the change in heat sink temperature over this range is representative of the change in internal temperature, the differential resistive heating is approximately

$$\frac{dT}{dJ} = wL\frac{dT}{dI}$$
$$\approx wL\frac{\partial T}{\partial \lambda}\frac{\partial \lambda}{\partial I}$$
$$\approx wL\frac{\Delta T}{\Delta \lambda}\frac{\Delta \lambda}{\Delta I} \qquad (5.46)$$

where w is the ridge width and L is the cavity length.

Length	ΔI (mA)		ΔT (°C)		dT/dI (°C/mA)	
	16.7		7.2		0.33	
	8.4		2.79		0.26	

Table 5.4 - Measured and calculated quantities used to estimate the differential resistive heating occurring inside the lasers under study.

The quantities in (5.46) were measured for 250 μm and 1000 μm cavity lengths and are summarized in Table 5.2. It can be seen that dI / dT is lower for longer devices, but dJ / dT is higher. To get an idea of the magnitude of the heating in real terms, the change in temperature between zero bias and threshold can be estimated using the above-threshold dI / dT. From Fig. 5.6, the threshold currents of the 250 μm and 1000 μm devices were 17.1 and 32.0 mA, respectively. The change in temperature in both cases is

$$\Delta T_{250\mu m}(0 \rightarrow 17.1mA) \approx \Delta I\frac{dT}{dI}$$
$$= 17.1 \cdot 0.33$$
$$= 5.6°C,$$

$$\Delta T_{1000\mu m}(0 \rightarrow 32mA) \approx 32 \cdot 0.26$$
$$= 8.3°C.$$

The temperature difference at threshold between the 250 μm and 1000 μm devices is on the order of 3°C. One would expect the temperature difference between the 250 μm

and 500 μm devices to be even less. The gain coefficient, ΓG_0, of these two devices changes by about 22% according to Table 5.1. In contrast, a change in heat sink temperature of 10°C (20-30°C) causes the gain coefficient determined by efficiency measurements Fig. 3.9 to change by only about 10%. Apparently, the temperature difference due to the different lengths cannot directly explain the change in gain coefficient. Note that the transparency current density also cannot be explained since it is expected to increase with temperature and hence with length.

In Chapter 4, it was observed that T_{max} increased with well number up to 10 wells, then decreased for 12 and 14 well devices with longer cavity lengths. Several mechanisms could explain this behaviour. For example, an increase in the number of strained layers could cause an increase in the number of crystal defects. The resulting increase in current leakage paths could, conceivably, affect the temperature performance of the threshold current. However, the low-temperature extrapolation of the threshold current density, J_0, did not show an abnormal increase for 12 and 14 wells, as would be expected in such a case.

It was suggested in Chapter 4 that a non-uniform carrier distribution among the wells could explain the anomalous T_{max} values of the 12 and 14 well devices. Obviously, the larger the number of quantum wells, the more likely it is that the finite transport time of the holes across the active region (since holes have a lower mobility) plays a role. As the length of the device decreases, a higher gain and hence higher population inversion is required to reach threshold. More carriers in the quantum wells and a higher Fermi level will give rise to greater carrier spill-over into barrier states. Carriers could then be re-captured by other quantum wells, thus partially alleviating the transport problem. When the length is increased, the lower carrier density may mean that some wells will not contribute as much as others to the net gain. Fewer wells will be participating fully in consuming

current, giving a lower value for $N_w J_{tr}$ (i. e. - it will appear to *improve*). At the same time, the gain available to the optical mode will be reduced, giving a lower value for ΓG_0 (i. e. - it will appear to *degrade*). Since the same mechanism is responsible for both phenomena, both $N_w J_{tr}$ and ΓG_0 should change in a similar manner. J_0 would not necessarily reflect this situation since the hole mobility has a strong temperature dependence [6]. At lower temperatures, the increased mobility may mean that carrier transport problems are not significant.

As a final note, a curve similar to the fit in Fig. 5.6 can be produced by fixing the gain coefficient at its 250 μm value of $\Gamma G_0 = 90.1$ and adding a length independent current loss term so that

$$J_{th} = a_1 \exp\{\ln(1/.3) / 90.1L\} + a_2 / wL$$

where a_1 and a_2 are fitting parameters. The best fit gives $a_1 = 990\ A/cm^2$ and $a_2 = 8.3$ mA. The χ^2 for this fit is 7624 $(A/cm^2)^2$ in contrast to 3313 $(A/cm^2)^2$ for the fit in Fig. 5.6

5.5 Chapter Summary and Conclusions

The gain coefficient of a five quantum well device was calculated at room temperature by four separate methods. The theoretical calculation, direct measurement of the below-threshold spectrum of a 250 μm long device, and measurement of the above-threshold slope efficiency all yielded similar results. However, the standard method of observing the threshold current density as a function of cavity length yielded a value nearly one-half that of the other methods.

In order to understand this discrepancy, the gain curves for 375 μm and 500 μm devices were also measured directly. Contrary to expectations, both the gain coefficient and transparency current density were found to have a significant dependence on cavity

length. Furthermore, the two quantities changed by fractionally the same amount. This is quite remarkable since they have opposing effects on the threshold current. Internal resistive heating was considered as a possible source, but was discounted because it would cause the two quantities to change in opposition and the magnitude was not large enough support the hypothesis. However, it was found that a non-uniform distribution of carriers among the quantum wells could qualitatively explain the observations.

REFERENCES

[1] K. Prosyk, R. Kalnins, J. G. Simmons, "Observation of a length-dependent gain coefficient in quaternary MQW lasers", *IEEE J. Quantum Electron.*, to be submitted February 1998.

[2] B. Jonsson, S. T. Eng, "Solving the Schrodinger equation in arbitrary quantum-well potential profiles using the transfer matrix method", *IEEE J. Quantum Electron.*, vol. 26, pp. 2025-2035, 1990.

[3] P. S. Zory, ed., *Quantum Well Lasers*, Academic Press Inc., ch. 2, 1993.

[4] A. T. Macrander, S. Lau, "X-ray, photoluminescence, stoichiometry, and thickness mapping of $In_{1-x}Ga_xAs_yP_{1-y}$", *J. Electrochem. Soc.*, Vol. 138, pp. 1147-1154, 1991.

[5] S. L. Chuang, "Efficient band-structure calculations of strained quantum wells", *Phys. Rev. B*, Vol. 43, pp. 9649-9659, 1991.

[6] O. Madelung, *ed.*, *Landolt-Bornstein - Numerical Data and Functional Relationships in Science and Technology*, vol. 17a & 22a, Springer-Verlag, 1987.

[7] D. T. DeTemple, C. M. Herzinger, "On the semiconductor laser logarithmic gain-current density relation", *IEEE J. Quantum Electron.*, vol. 29, pp. 1246-1252, 1993.

[8] J. E. A. Whiteaway, G. H. B. Thompson, P. D. Greene, R. W. Glew, "Logarithmic gain/current density characteristic of InGaAs/InGaAlAs/InP multi-quantum-well separate-confinement-heterostructure lasers", *Electron. Lett.*, vol. 27, pp. 340-342, 1991.

[9] D. T. Cassidy, "Technique for measurement of the gain spectra of semiconductor diode lasers", *J. Appl. Phys.*, vol. 56, pp. 3096-3098, 1984.

CHAPTER SIX

LINEWIDTH[†]

6.0 INTRODUCTION

THE above-threshold laser line is of interest both from a physics point of view and in terms of practical applications. Narrow spectral sources are desirable in demanding applications such as analogue cable television (CATV) links and coherent communications. Linewidth specifications for these devices can be considerably less than 1 MHz. Measurements of linewidths this narrow is challenging. For example, it has been observed that linewidth measurements suffer from highly imprecise results. A recent round-robin study was performed by a European opto-electronics consortium (COST 215) wherein a set of semiconductor lasers was passed from company to company, and the linewidth was evaluated by various methods at each site. The lasers were returned to the original site and re-evaluated to ensure against handling and operational degradation. It was found that discrepancies in the measured linewidth between different sites varied by a factor of more

---

[†]Portions of this chapter have been submitted for publication in [1].

than two for similar techniques and up to a factor of ten for different techniques [2].

Obviously then, it is desirable to pursue a method of linewidth measurement which can be made reproducible and free from errors. To this end, the delayed self-homodyne (DSH) technique was investigated. Both the DSH and the very similar delayed self-heterodyne techniques are the most popular approaches due to their high resolution, stability and ease of use.

In Section 6.1, the DSH technique is outlined and examples of linewidth *vs.* inverse power plots are given. The effect of carefully filtering the drive current source for the laser is investigated. In preparation for a mathematical description of the effect of laser current noise on the DSH technique, a model of the DSH technique in the absence of source current noise is developed in Section 6.2. In Section 6.3, a simplified "single tone" noise model is developed and verified experimentally in Section 6.4. Finally, in Section 6.5, a low-pass band of current noise is considered and guidelines for appropriate filtering of the current source are provided. Although this chapter deals exclusively with the DSH technique, everything presented here is equally applicable to delayed self-heterodyne measurements. The only observable difference is a shift in the RF spectrum by an amount equal to the frequency of the acousto-optic modulator.

6.1 Linewidth Measurements Using the DSH Technique

In delayed self-homodyning, the laser output is interfered with itself [3]. A schematic of a DSH experimental set-up is shown in Fig. 6.1. The laser output is launched into a tapered fibre, passed through a high return-loss (< -65 dB) optical isolator, and split into two paths of approximately equal intensity. The laser line can be observed while the fibre is moved by small amounts to ensure that reflections from the tapered fibre tip are having no effect on the lineshape.

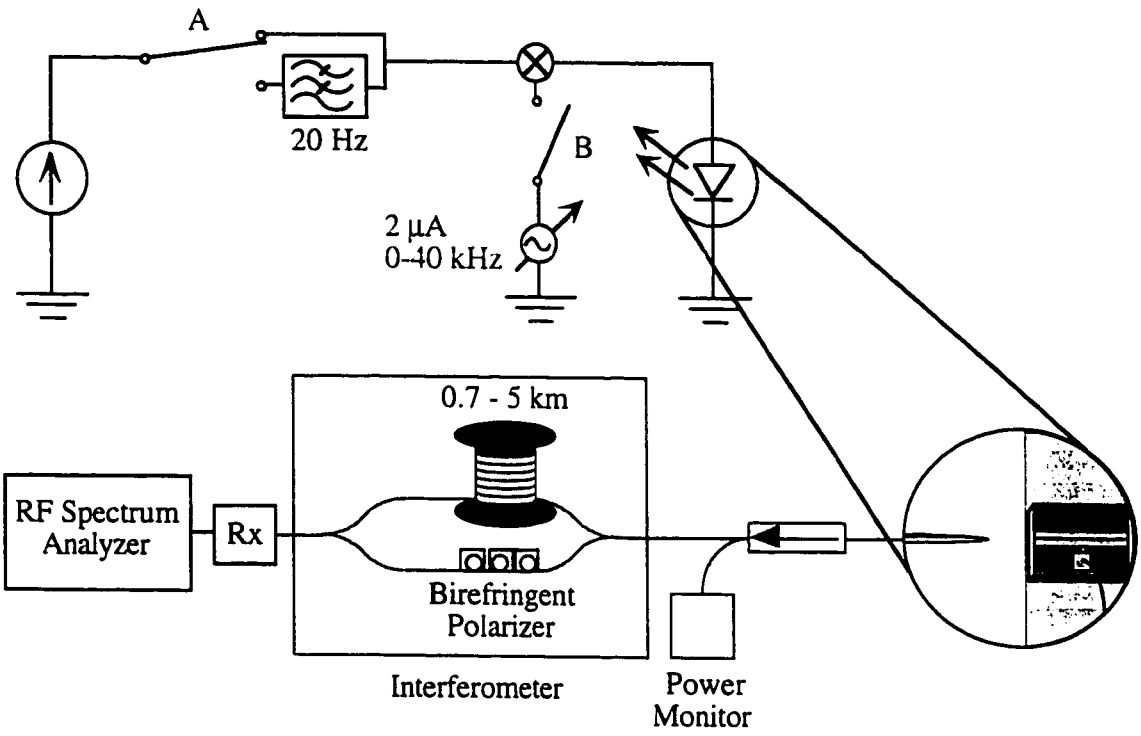

Figure 6.1 - Schematic diagram of the DSH experiment. Switches A and B are shown in the standard 'off' positions.

The polarization difference between the two paths is kept at a minimum by using small amounts of stress in one arm to introduce birefringence. The light through one path is delayed by a length, L_D, corresponding to a transit time of τ_D. L_D is chosen so that the outputs of the two arms are mutually uncorrelated. One rule of thumb is that τ_D should be greater than three times the coherence time, τ_C, of the laser, which is related to the (Lorentzian) linewidth, $\Delta\nu$, by [4]

$$\tau_C = \frac{1}{\pi\Delta\nu}. \qquad (6.1)$$

Decreasing linewidths require increasing L_D. Typical delay lengths range from 700 m to 5 km or more. Self homo- and hetero-dyne fibre interferometers are available from a variety of commercial sources.

The two paths are recombined and detected with an RF receiver, and displayed on an RF spectrum analyzer with resolution and video bandwidths of 30 kHz and 10 kHz, respectively. The output power of the laser is monitored simultaneously by splitting off a small portion of the optical signal before entering the interferometer. Current to the laser is supplied by a commercially available, shielded lead-acid battery source with a 100 kHz low-pass filter network. Although this is considered an adequate precaution against current noise [5], it will be shown in the next section that the DSH technique is far more sensitive to current noise than previously appreciated, and inappropriate filtering of the current source can introduce significant errors in the measured linewidth.

The detected RF signal represents the laser line convolved with itself [6], as shown in Section 6.2. In the DSH technique, the negative frequency components are folded onto the positive side of the spectrum, so only half of the line is observed. Figure 6.2 shows a typical trace from a DSH measurement. The first 100 kHz is omitted to avoid the dc spike of the spectrum analyzer. Delayed self-heterodyne measurements give the same lineshape,

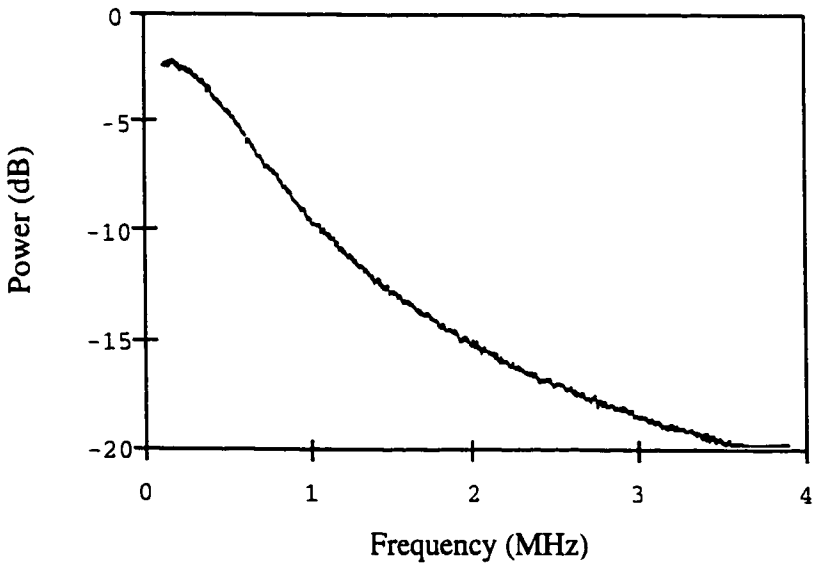

Figure 6.2 - Typical spectrum analyzer trace of the intrinsic laser line as observed by the DSH experiment (with switch A 'on' in Fig. 6.1). The trace is a digitally scanned scope photograph, with the correct axes added afterwards.

but the spectrum is shifted so that both sides of the RF spectrum can be viewed separately and the dc spike is avoided. Delayed self-heterodyning is achieved by winding some fibre from one arm around a cylinder of piezoelectric material. An RF voltage on the cylinder causes it to oscillate in diameter. The resulting index modulation of the fibre shifts the RF spectrum of the received signal.

In Chapter 2, an inverse relation between the linewidth and output power was derived for a Fabry-Perot laser. Although distributed feedback (DFB) lasers [7] are used here, the same characteristic is expected [4]. However, other non-ideal characteristics are often found instead, as depicted in Fig. 6.3. The extrapolation of the linear portion of the linewidth *vs.* inverse power curve to infinite power does not yield zero linewidth, but a residual linewidth is observed. At high powers, the linewidth departs from the linearity and becomes approximately constant, forming a linewidth "floor". As the power is further

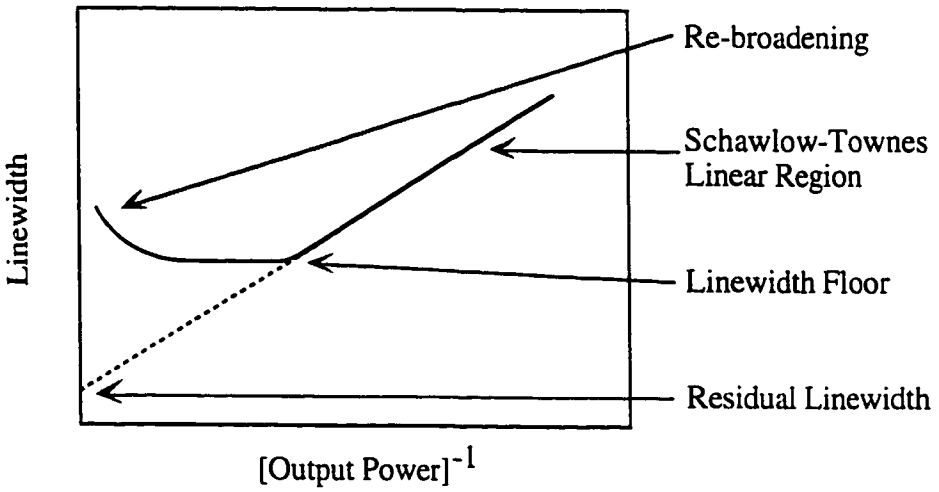

Figure 6.3 - Typical experimentally observed features of the linewidth *vs.* inverse power plot. Theoretically, the Schawlow-Townes linear region should have a zero intercept.

increased, a re-broadening of the laser line is observed. In addition, the lineshape is often found to have a non-Lorentzian component, usually assumed to be Gaussian, giving an overall Voigt profile†. The source of all these has been attributed to 1/f noise [8], [9], the physical cause of which has been postulated to be a variety of mechanisms [10], such as mode partition noise [11], event driven temperature fluctuations [12], fluctuations in local current density [13]-[15], optical absorption [16], and spatial hole burning [17].

Although, obviously, the source of non-ideal effects is of interest since eliminating them would reduce the linewidth, the presence of a non-Lorentzian lineshape component is especially irksome. Since a Lorentzian convolved with itself is a Lorentzian with twice the full width at half maximum (FWHM), the laser linewidth is easy to get from the RF spectrum: simply use the half width at half maximum (HWHM) of the RF spectrum. This is not the case when a non-Lorentzian component exists. Notably, the convolution of a Gaussian with itself is a Gaussian with $\sqrt{2}$ times the FWHM. The relationship between the FHWMs of a Voigt profile and an auto-convolved Voigt profile depends on the relative widths of the constituent Lorentzian and Gaussian components. An accurate determination of an arbitrary laser linewidth would require taking the square root of the Fourier transform, and then calculating the inverse Fourier transform. Although this is certainly possible to do, a further complication arises from the fact that the system impact of non-Lorentzian components is not well understood.

Two points are required to obtain the linewidth of a Lorentzian function. The (arbitrarily normalized) equation for the displayed RF spectrum in the absence of a non-Lorentzian component is

$$D_{RF} = \frac{1}{1+(v/\Delta v)^2} \tag{6.2}$$

---

† A Voigt profile is the convolution between a Lorentzian and a Gaussian function.

where, once again, $\Delta\nu$ is the laser FWHM and the HWHM of the RF spectrum. If two points on the RF spectrum are measured at ν_1 and ν_2 having a ratio, p, of the power at ν_1 divided by the power at ν_2, then from (6.2)

$$\Delta\nu = \frac{\nu_1}{2}\left[\frac{\left(\nu_2^2 / \nu_1^2\right)p - 1}{p - 1}\right]^{1/2} \tag{6.3}$$

Linewidth measurements were performed using (6.3) on a Nortel Technology partially gain-coupled distributed feedback (GC-DFB) laser [18]. The frequency ν_1 was kept at 200 kHz for all measurements and ν_2 was adjusted for $p = 3$ dB. As a check on the lineshape, ν_2 was also measured at $p = 10$ dB, which will give the same $\Delta\nu$ for a

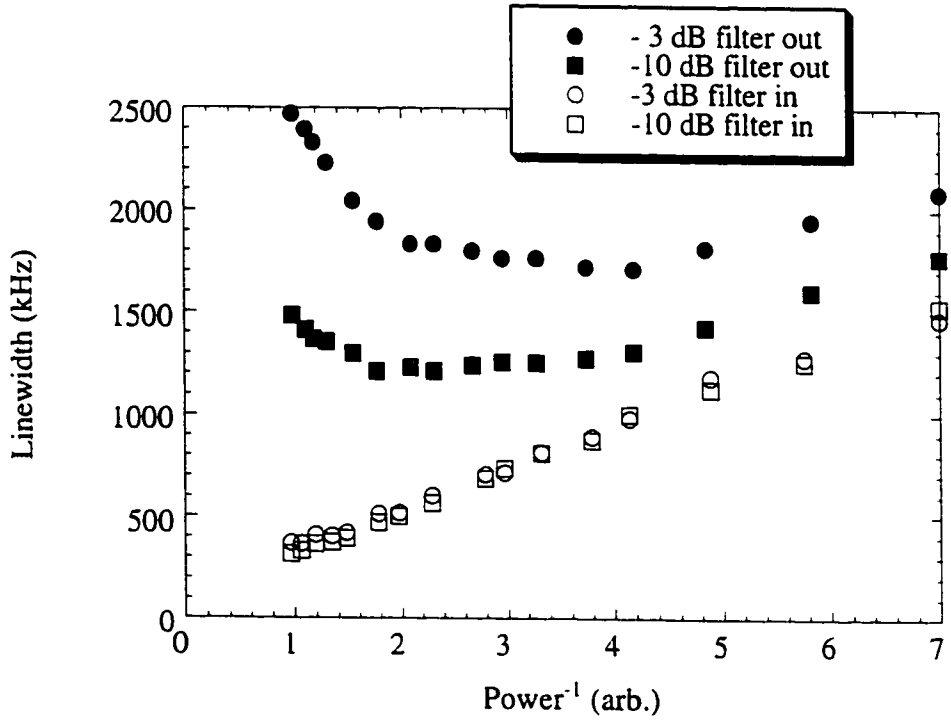

Figure 6.4 - Linewidth of a GC-DFB laser as a function of inverse power. The solid symbols represent the measured linewidth in the absence of additional current filtering (switch A in the 'off' position in Fig. 6.1) and the open symbols are with a 20 Hz filter in place. The circles are the linewidth measured at the -3 dB point, the squares are measured at the -10 dB point.

Lorentzian line. The results of these measurements are shown as a function of inverse power in Fig. 6.4 as the solid symbols. All the features usually associated with 1/f-noise mentioned above appear in the Figure, including a significant non-Lorentzian component as is indicated by the large difference in $\Delta\nu$ obtained from the different values of p. However, when a very narrow low pass (20 Hz) filter is placed in series with the current source output (switch A 'on' in Fig. 6.1), the lineshape becomes Lorentzian, and the residual linewidth, linewidth floor, and premature re-broadening all disappear. From the open symbols in Fig. 6.4, it is evident that the ideal inverse power relation derived in Chapter 2 is recovered.

6.2 THE DSH MODEL

Given the remarkable change in the behaviour of the linewidth when a narrow band filter is placed in series with the current source, further investigation is required to determine whether the actual linewidth has changed, or if this is an artifact of the measurement technique. Before examining the effect of current noise on the measurement technique, it is first necessary to derive an expression for the linewidth observed by the DSH method in the absence of noise. The output field, E, of a laser above threshold can be written in terms of the mean frequency at the centre of the laser line

$$E = \mathrm{Re}\left\{\tilde{E}\right\} \tag{6.4}$$

where the tilde (~) denotes a complex (or "analytic") signal,

$$\tilde{E} = E_0 e^{i(\omega_0 t + \phi_N(t))},$$

ω_0 is the centre frequency of the lasing mode, $\phi_N(t)$ is the phase noise induced by spontaneous emission and the finite passband of the laser cavity, and E_0 is the field amplitude. The amplitude noise is small compared to the phase noise [4] and is ignored

here.

The phase signal $\phi_N(t)$ is a peculiar variable and its properties need to be outlined before proceeding. It is a random signal and is assumed here to be ergodic; i. e. that the time average of a function of $\phi_N(t)$ is equal to the statistical average of an ensemble of randomly chosen lasers, each with its own $\phi_N(t)$ [19]. Such an average is independent of time and hence $\phi_N(t)$ is also strictly stationary.

Writing the time average of $\phi_N(t)$ can be conceptually confusing if not dealt with properly. If a laser is chosen randomly from an ensemble, $\phi_N(t)$ is equally likely to take on any value. Furthermore, values separated by 2π are equivalent. The latter could be addressed by taking the 2π modulo of $\phi_N(t)$. A range of 2π could be chosen, say

$$\phi_N(t) \,(\mathrm{mod}\, 2\pi) = -\pi...\pi \tag{6.5}$$

giving

$$\langle \phi_N(t) \rangle = 0$$

where $\langle\ \rangle$ denotes ensemble or time average. However, the choice of range is arbitrary and could easily have been chosen to be

$$\phi_N(t) \,(\mathrm{mod}\, 2\pi) = 0...2\pi$$

in which case

$$\langle \phi_N(t) \rangle = \pi$$

In a sense, there is a gauge freedom present in $\langle \phi_N(t) \rangle$. The issue can be side-stepped by conceptually choosing an arbitrary reference phase Φ_0, and writing all $\phi_N(t)$ as a difference between the reference phase. In this manner, the time average becomes

$$\langle \phi_N(t) - \Phi_0 \rangle = 0$$

which is a definite zero-mean process. Since this is the same as choosing the zero-mean gauge of (6.5) that is what is done in the following derivations. The probability

distribution function (PDF) of $\phi_N(t)$, p_{ϕ_N}, is therefore

$$p_{\phi_N} = \begin{cases} 1/2\pi & -\pi < \phi_N < \pi \\ 0 & \text{otherwise} \end{cases}$$

from which the PDF of the cosine and sine of $\phi_N(t)$ are calculated to be [20]

$$p_z = \begin{cases} \left(\pi\sqrt{1-z^2}\right)^{-1} & -1 \le z \le 1 \\ 0 & \text{otherwise} \end{cases}$$

where z is $\cos\phi_N$ or $\sin\phi_N$. Since the PDFs are symmetric about $z = 0$, the time average of z vanishes and

$$\left\langle e^{i\phi_N} \right\rangle = 0. \tag{6.6}$$

Although $\phi_N(t)$ is ergodic, it is still has a limited causality; $\phi_N(t+\tau)$ is not statistically independent of $\phi_N(t)$ unless $\tau > 3\tau_c$, where τ_c is the coherence time. The phase difference function is defined by

$$\Delta\phi_N(t,\tau) \equiv \phi_N(t+\tau) - \phi_N(t) \tag{6.7}$$

and has a symmetric PDF.

We are now in a position to determine the relationship between the phase noise and the laser lineshape. The power spectral density of the intrinsic laser line is given by the Fourier transform of the (suitably normalized) autocorrelation, Γ, of the complex field [20]

$$\Gamma_{\tilde{E}} \alpha \left\langle \tilde{E}(t+\tau)\tilde{E}^*(t) \right\rangle$$

where (*) denotes complex conjugate. Substituting for the field in (6.4),

$$\begin{aligned} \Gamma_{\tilde{E}} &= 4P_0 \left\langle e^{i(\omega_0(t+\tau)+\phi_N(t+\tau))} e^{-i(\omega_0 t+\phi_N(t))} \right\rangle \\ &= 4P_0 e^{i\omega_0\tau} \left\langle e^{i(\Delta\phi_N(t,\tau))} \right\rangle. \end{aligned} \tag{6.8}$$

The factor of 4 appears in (6.8) because the power spectral density of the analytic signal is four times that of the real signal [20].

In Fourier transforming (6.8), $e^{i\omega_0\tau}$ acts to shift the line so that it is centred about ω_0. The actual shape of the laser line, $\mathcal{L}(\nu)$, is given by

$$\mathcal{L}(\nu) = \Im\{\langle e^{i\Delta\phi(t,\tau)}\rangle\} \tag{6.9}$$

where $\Im\{\}$ signifies the Fourier transform with respect to τ.

A laser with a noiseless current source being measured by the DSH technique (switch A 'on' and switch B 'off' in Fig. 6.1) will have its field split into two paths. One path will be delayed by a time $\tau_d > 3\tau_c$ to ensure mutual incoherence between the two arms. The phase noises from the arms are $\phi_N(t)$ and $\phi_N(t+\tau_d)$ respectively. However, writing the phase noise this way presents a minor problem when forming the autocorrelation at the interferometer output because $\phi_N(t+\tau)$ and $\phi_N(t+\tau_d)$ are not mutually incoherent for all τ (i. e. - when τ approaches τ_d). Since the autocorrelation integral is over all τ, it would seem that the statistics of $\phi_N(t)$ over the whole range from completely coherent to completely incoherent needs to be known. Treatments in this vein have been done for arbitrary τ_d by assuming, for example, a white frequency noise spectrum [21]. Aside from relaxing the pre-condition on the frequency noise spectrum [6], restricting the analysis to the non-coherent regime simplifies the mathematics and allows for an easier introduction of current noise. From the ensemble viewpoint this is not a problem: demanding $\tau_d > 3\tau_c$ automatically restricts the ensemble to lasers with mutually incoherent phase noise outputs from the two arms. To translate this ensemble into the time domain, the phase noise from the short and long arms are written as $\phi_1(t)$ and $\phi_2(t)$ respectively, where $\phi_1(t)$ and $\phi_2(t)$ are mutually incoherent for all t. Note that the ϕ_i $(i = 1,2)$ have the same statistics as ϕ_N so that

$$\langle e^{i\phi_i}\rangle = \langle e^{i\phi_N}\rangle = 0 \tag{6.10a}$$

$$\langle e^{i\Delta\phi_i(t,\tau)}\rangle = \langle e^{i\Delta\phi_N(t,\tau)}\rangle \tag{6.10b}$$

$$\langle f(\phi_1)g(\phi_2)\rangle = \langle f(\phi_1(t))\rangle\langle g(\phi_2(t))\rangle \tag{6.10c}$$

Equation (6.10c) is the well-known property that the mean of the product of two mutually incoherent processes is equal to the product of the means [20].

The real field output of the interferometer is

$$E_b = \frac{E_0}{\sqrt{2}}\left[\cos(\omega_0 t + \phi_1(t)) + \cos(\omega_0(t+\tau_d) + \phi_2(t))\right]$$

A 1:1 split ratio and equal polarizations have been assumed for simplicity, but is not necessary in general. The time dependence of the output power is given by the square of the real field,

$$\begin{aligned} P_b &= P_0\left[\cos(\omega_0 t + \phi_1(t)) + \cos(\omega_0(t+\tau_d) + \phi_2(t))\right]^2 \\ &= P_0\left[1 + \frac{1}{2}\cos(2\omega_0 t + 2\phi_1(t)) + \frac{1}{2}\cos(2\omega_0(t+\tau_d) + 2\phi_2(t))\right. \\ &\qquad \left. + \frac{1}{2}\cos(\omega_0\tau_d + \phi_2(t) - \phi_1(t)) + \frac{1}{2}\cos(2\omega_0 t + \phi_2(t) + \phi_1(t))\right] \end{aligned}$$

which has an analytic signal of

$$\begin{aligned} \tilde{P}_b = P_0\left[1 + \frac{1}{2}e^{i[2\omega_0 t + 2\phi_1(t)]} + \frac{1}{2}e^{i[2\omega_0(t+\tau_d) + 2\phi_2(t)]}\right. \\ \left. + \frac{1}{2}e^{i[\omega_0\tau_d + \phi_2(t) - \phi_1(t)]} + \frac{1}{2}e^{i[2\omega_0 t + \omega_0\tau_d + \phi_2(t) + \phi_1(t)]}\right]. \end{aligned} \qquad (6.11)$$

When the optical power is detected, it will give rise to a photocurrent, $\tilde{I}(t)$, given by

$$\tilde{I}(t) = \eta\tilde{P}_b(t)$$

where η is the optical-to-electrical conversion efficiency. The electrical power spectrum is given by Fourier transforming the autocorrelation, $\Gamma_{\tilde{I}}$, of the current. Using (6.11), one finds

$$\begin{aligned}\Gamma_{\tilde{I}} &= 4\eta^2\left\langle \tilde{P}_b(t+\tau)\tilde{P}_b^*(t)\right\rangle \\ &= 4\eta^2\left\langle 1+\frac{1}{4}e^{i[2\omega_0\tau+2\Delta\phi_1(t,\tau)]}+\frac{1}{4}e^{i[2\omega_0\tau+2\Delta\phi_2(t,\tau)]}\right. \\ &\qquad \left.+\frac{1}{4}e^{i[\Delta\phi_2(t,\tau)-\Delta\phi_1(t,\tau)]}+\frac{1}{4}e^{i[2\omega_0\tau+\Delta\phi_2(t,\tau)-\Delta\phi_1(t,\tau)]}\right\rangle \qquad (6.12)\end{aligned}$$

The cross-terms produced in multiplying out the analytic signal of the power vanish in (6.12) since they contain factors such as

$$\left\langle e^{i2(\phi_2(t)-\phi_1(t))}\right\rangle$$

which, from (6.10c) and (6.10a),

$$\begin{aligned}\left\langle e^{i2(\phi_2(t)-\phi_1(t))}\right\rangle &= \left\langle e^{-2i\phi_1(t)}\right\rangle\left\langle e^{2i\phi_2(t)}\right\rangle \\ &= 0\end{aligned}$$

or have factors such as

$$\left\langle e^{i2(\phi_2(t)+\phi_2(t))}\right\rangle$$

which similarly vanishes.

By applying (6.10b) and (6.10c) and collecting terms, (6.12) can be written

$$\Gamma_{\tilde{I}} = 4\eta^2P_0^2\left[1+\frac{3}{4}e^{2i\omega_0\tau}\left\langle e^{i\Delta\phi_N(t,\tau)}\right\rangle^2+\frac{1}{4}\left\langle e^{i\Delta\phi_N(t,\tau)}\right\rangle^2\right]$$

The first term is a dc term. The second term contains a factor of $e^{2i\omega_0\tau}$ which acts to shift the laser line to twice the optical frequency. Since most detectors cannot respond to a signal this fast, the power from this term is also detected as dc. The ac signal will therefore be given by the final term, called the homodyne cross-term, $\Gamma_{\tilde{I}_x}$,

$$\Gamma_{\tilde{I}_x} = \eta^2P_0^2\left\langle e^{i\Delta\phi_N(t,\tau)}\right\rangle^2.$$

By taking one-quarter of the Fourier transform of $\Gamma_{\tilde{I}_x}$ and using (6.9), the RF power spectral density of the real signal, $P_{RF}(\nu)$, is found to be

$$P_{RF}(\nu) = \frac{\eta^2 P_0^2}{4} \mathcal{L}(\nu) \otimes \mathcal{L}(\nu) \tag{6.13}$$

Self-homodyning, then, serves to down shift the laser line from the original optical frequency so that it is centred about $\nu = 0$ and convolve the line with itself.

6.3 THE SINGLE-TONE MODEL

A single frequency tone is the limit of a noise band as the bandwidth is reduced to a very small frequency range. This limit will be examined first, since it is easier to treat both mathematically and experimentally.

When the drive current of a laser is changed, the centre frequency of the laser line also changes or "chirps". The amount of frequency change per unit current is called the FM sensitivity, S_{FM}. For a dc biased laser undergoing modulation of amplitude I_m at a modulation frequency f_m, the radial frequency shift, $\dot{\phi}_M(t)$, of the laser centre frequency is

$$\dot{\phi}_M(t) = 2\pi S_{FM} I_m \cos(2\pi f_m t)$$

giving a phase shift, $\phi_M(t)$, after time t of

$$\phi_M(t) = \frac{S_{FM} I_m}{f_m} \sin(2\pi f_m t) \ . \tag{6.14}$$

We now wish to examine the effect of the chirp-induced sinusoidal phase shifting of (6.14) on the DSH interferometer. The new autocorrelation function of the homodyne cross-term can be obtained by replacing the phase noise of each arm, $\phi_1(t)$ and $\phi_2(t)$ in (6.12) with the total phase, $\phi_1(t) + \phi_M(t)$ and $\phi_2(t) + \phi_M(t + \tau_d)$, respectively, so that

$$\begin{aligned} \Gamma_{\bar{i}_x} &= \frac{\eta^2 P_0}{4} \left\langle e^{i[\Delta\phi_2(t,\tau) - \Delta\phi_1(t,\tau)]} e^{i[\Delta\phi_M(t+\tau,\tau_d) - \Delta\phi_M(t,\tau_d)]} \right\rangle \\ &= \frac{\eta^2 P_0}{4} \left\langle e^{i\Delta\phi_N(t,\tau)} \right\rangle^2 \left\langle e^{i\Delta\phi_M(t+\tau,\tau_d)} e^{-i\Delta\phi_M(t,\tau_d)} \right\rangle \end{aligned} \tag{6.15}$$

The modulation contribution (second angle brackets) has been separated from the intrinsic

phase noise because the two are statistically independent. The modulation contribution is given the symbol $M(\tau)$, defined as

$$M(\tau) \equiv \left\langle e^{i\Delta\phi_M(t+\tau,\tau_d)} e^{-i\Delta\phi_M(t,\tau_d)} \right\rangle \tag{6.16}$$

The exponential factors can be expressed in terms of cosines and sines, for example,

$$e^{-i\Delta\phi_M(t,\tau_d)} = \cos\left[x\sin(2\pi f_m t + \varphi)\right] - i\sin\left[x\sin(2\pi f_m t + \varphi)\right]$$

where

$$\begin{aligned}\Delta\phi_M(t,\tau_d) &= \phi_M(t+\tau_d) - \phi_M(t) \\ &= \frac{S_{FM} I_m}{f_m}\left[\sin(2\pi f_m(t+\tau_d)) - \sin(2\pi f_m t)\right] \\ &= x\sin(2\pi f_m t + \varphi)\,,\end{aligned}$$

and

$$\begin{aligned}x &= \frac{2S_{FM} I_m}{f_m}\sin(\pi f_m \tau_d) \\ \varphi &= \pi f_m \tau_d + \pi/2\,.\end{aligned}$$

Expanding this in terms of Bessel functions, we arrive at a even real series and an imaginary odd series:

$$\begin{aligned}e^{-i\Delta\phi_M(t,\tau_d)} = {} & J_0(x) + 2J_2(x)\cos 2\theta + 2J_4(x)\cos 4\theta + \ldots \\ & - i\left[2J_1(x)\sin\theta + 2J_3(x)\sin 3\theta + \ldots\right]\end{aligned}$$

where

$$\theta = 2\pi f_m t + \varphi\,.$$

A similar expansion can be made for the $e^{i\Delta\phi_M(t+\tau,\tau_d)}$ factor in (6.16), except that t is replaced with $t+\tau$ and the imaginary series has a plus sign in front of it. The product of the two factors results in four series: the product of the two even Bessel series, the product of the two odd Bessel series, and two cross-series. All terms in both cross-series vanish, since

$$\langle \cos A \sin B \rangle = \left\langle \frac{1}{2}\left[\sin(B-A) + \sin(B+A)\right] \right\rangle = 0$$

where A and B are integer multiples of $\theta(t)$ or $\theta(t+\tau)$. Similarly, cross terms in the other two (even and odd) series also vanish since

$$\langle \cos A \cos B \rangle = \left\langle \frac{1}{2}[\cos(A-B)+\cos(A+B)] \right\rangle = 0$$

when $A \neq B$. This leaves only direct terms of the form

$$\begin{aligned}
&\langle \cos(2\pi n f_m(t+\tau)+n\varphi)\cos(2\pi n f_m t+n\varphi)\rangle \\
&= \langle \cos^2(2\pi n f_m t+n\varphi)\rangle \cos(2\pi n f_m \tau) - \langle \sin(2\pi n f_m t+n\varphi)\cos(2\pi n f_m t+n\varphi)\rangle \sin(2\pi n f_m \tau) \\
&= \frac{1}{2}\cos(2\pi n f_m \tau)
\end{aligned}$$

and

$$\begin{aligned}
&\langle \sin(2\pi n f_m(t+\tau)+n\varphi)\sin(2\pi n f_m t+n\varphi)\rangle \\
&= \langle \sin^2(2\pi n f_m t+n\varphi)\rangle \cos(2\pi n f_m \tau) - \langle \cos(2\pi n f_m t+n\varphi)\sin(2\pi n f_m t+n\varphi)\rangle \sin(2\pi n f_m \tau) \\
&= \frac{1}{2}\cos(2\pi n f_m \tau)
\end{aligned}$$

where n is an integer. Applying these identities, (6.16) becomes

$$M(\tau) = \sum_{n=-\infty}^{\infty} [J_n(x)]^2 \cos(2\pi n f_m \tau) \tag{6.17}$$

The Fourier transform of (6.17) is

$$\mathcal{M}(\nu) = \sum_{n=-\infty}^{\infty} [J_n(x)]^2 \delta(\nu - n f_m) \, . \tag{6.18}$$

The modified detected RF spectrum is given by the Fourier transform of (6.15) which, with (6.13) and (6.18), can be written

$$P_{RF}(\nu) = \frac{\eta^2 P_0}{4} \mathcal{M}(\nu) \otimes [\mathcal{L}(\nu) \otimes \mathcal{L}(\nu)] \, . \tag{6.19}$$

Equations similar to (6.18) and (6.19) have been presented previously for other purposes [22], but in the absence of any derivation. Equation (6.19) represents a sum of shifted

lasers lines, each weighted by $[J_n(x)]^2$.

6.4 EXPERIMENTAL VERIFICATION

To experimentally verify (6.19), the set-up in Fig. 6.1 was used with switch A and B both in the 'on' positions. A dither current amplitude of $I_m = 2$ μA was used and the frequency was varied over a range of $f_m = 0...40$ kHz. Two interferometers were used with delay lengths of 5 km and 700 m and corresponding differential optical mode delays of τ_d = 25.6 and 3.60 μs, respectively. Both lengths gave the same linewidth of 400 kHz in the absence of a dither. S_{FM} was measured independently using a scanning Fabry-Perot interferometer (FPI) with the following procedure.

Light was coupled into the FPI using single-mode fibre and a lens system which is built in to the commercially available FPI package. One mirror of the FPI was scanned with a piezo-electric positioner and the output of the scan was displayed on an oscilloscope set to trigger at the beginning of the scan. The temperature stabilized laser was dc biased above threshold. The scope graticule was calibrated by adding an RF signal of known frequency to the laser drive current. The resulting AM sidebands were observed on the scope and used to adjust the frequency scale. The RF source was replaced by the low-frequency source in Fig. 6.1. As the laser centre frequency oscillates, a distinctive "double horn" curve is observed on the scope trace (see below). The FM chirp at that frequency and amplitude is given by half the frequency between the two horns. In order to obtain a resolvable difference between the horns, a much larger current amplitude had to be used (I_m ~ 1 mA). The chirp was found to be proportional to current amplitude in the range $I_m = 0.1...2$ mA, and is assumed to be similarly proportional down to $I_m = 2$ μA. The measured S_{FM} as a function of frequency for the laser under study is given in Fig. 6.5 and can be seen to be well described by a logarithm function,

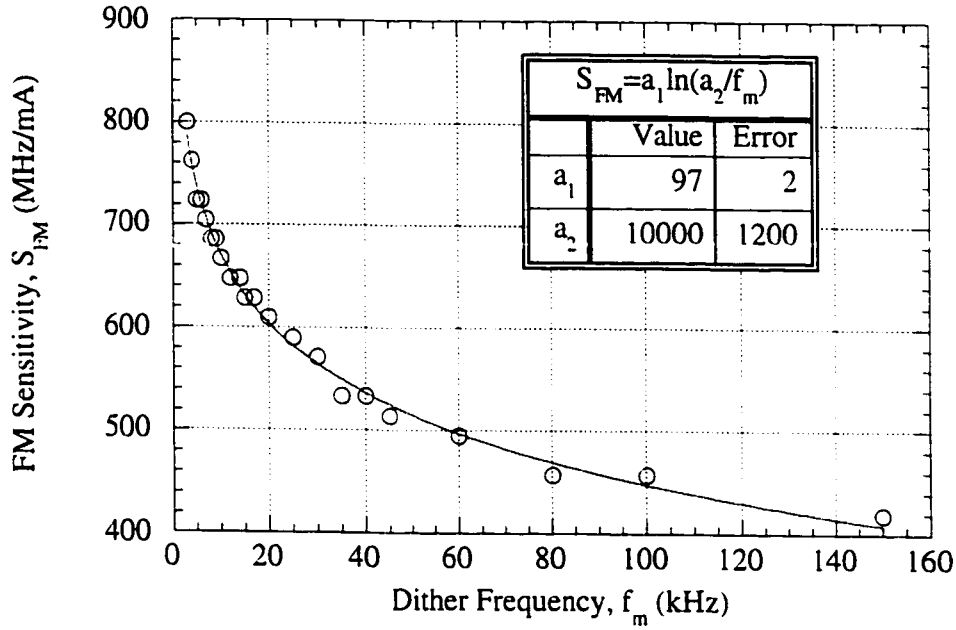

Figure 6.5 - FM sensitivity as a function of dither frequency at low frequencies.

$$S_{FM}(\text{MHz / mA}) = 97 \ln\left(10^4 / f_m\right) \tag{6.20}$$

where f_m is in kHz.

With the above information, a prediction for the apparent linewidth in the presence of the 2 μA dither can be made for a range of f_m. Applying the known values of f_m, I_m, τ_d, and $S_{FM}(f_m)$ to (6.18), $\mathcal{M}(\nu)$ can be calculated. This is then convolved with the auto-convolved natural laser line which is assumed to be Lorentzian. An "apparent" linewidth is obtained by the usual method in (6.3) with $\nu_1 = 200$ kHz and $p = 3$ dB.

Qualitatively, it is convenient to picture $\mathcal{M}(\nu)$ in the so-called "quasi-static approximation" [19]. The oscillating dither current causes the laser centre frequency to oscillate sinusoidally. This signal is separated into two paths, but when they are recombined, the sinusoidal oscillation in the delayed path is phase-shifted with respect to the reference arm. This will have an effect on the detected RF signal which is caused by the beating between the two arms. If there is no phase difference between the centre

frequency of the two arms, then no effect will be observed in the RF beat spectrum. A small phase difference will mean a small amplitude sinusoidal modulation of the beat spectrum as the laser centre frequencies follow each other and cross when they are equidistant from the turning point. As the phase difference increases to 180°, a maximum in the average size of the beat signal will be reached. The RF spectrum will then return to its unperturbed value when the phase difference reached 360°.

Under these circumstances, the difference, $\Delta\nu_{DSH}$, between the centre frequencies of the two arms is

$$\begin{aligned}\Delta\nu_{DSH} &= S_{FM}I_m\left[\sin\left(2\pi f_m(t+\tau_d)\right)-\sin\left(2\pi f_m t\right)\right]\\ &= 2S_{FM}I_m\sin\left(\pi f_m\tau_d\right)\sin\left(2\pi f_m(2t+\tau_d)\right)\,.\end{aligned} \tag{6.21}$$

The quasi-static modulation function, $\mathcal{M}_{QS}(\nu)$, is the probability of finding $\Delta\nu_{DSH}$ between ν and $\nu+d\nu$. From (6.21), it is given by the PDF of a simple harmonic oscillator oscillating with amplitude $2S_{FM}I_m\sin\left(\pi f_m\tau_d\right)$:

$$\mathcal{M}_{QS}(\nu)=\begin{cases}\dfrac{1}{\pi\sqrt{\left[2S_{FM}I_m\sin\left(\pi f_m\tau_d\right)\right]^2-\nu^2}} & \text{for } \nu\le 2S_{FM}I_m\sin\left(\pi f_m\tau_d\right)\\ 0 & \text{for } \nu>2S_{FM}I_m\sin\left(\pi f_m\tau_d\right)\end{cases} \tag{6.22}$$

which will be convolved with $\mathcal{L}(\nu)\otimes\mathcal{L}(\nu)$ as in (6.19). Equation (6.19) contains a series of δ-functions and (6.22) approaches infinity at the limits $\nu=\pm 2S_{FM}I_m\sin\left(\pi f_m\tau_d\right)$. In order to compare the two, the sideband height (integrating the δ-function) of $\mathcal{M}(\nu)$ for $f_m=10$ kHz and $I_m=2\,\mu$A was summed into bins 40 kHz in width. $\mathcal{M}_{QS}(\nu)$ was integrated over the same bin width. The two-sided results are plotted in staircase format in Fig. 6.6. As the bin width is increased, the two functions become increasingly similar. Since the linewidth being convolved with the modulation function is a factor of ten larger than the bin size in Fig. 6.6, $\mathcal{M}_{QS}(\nu)$ should in fact be a valid approximation.

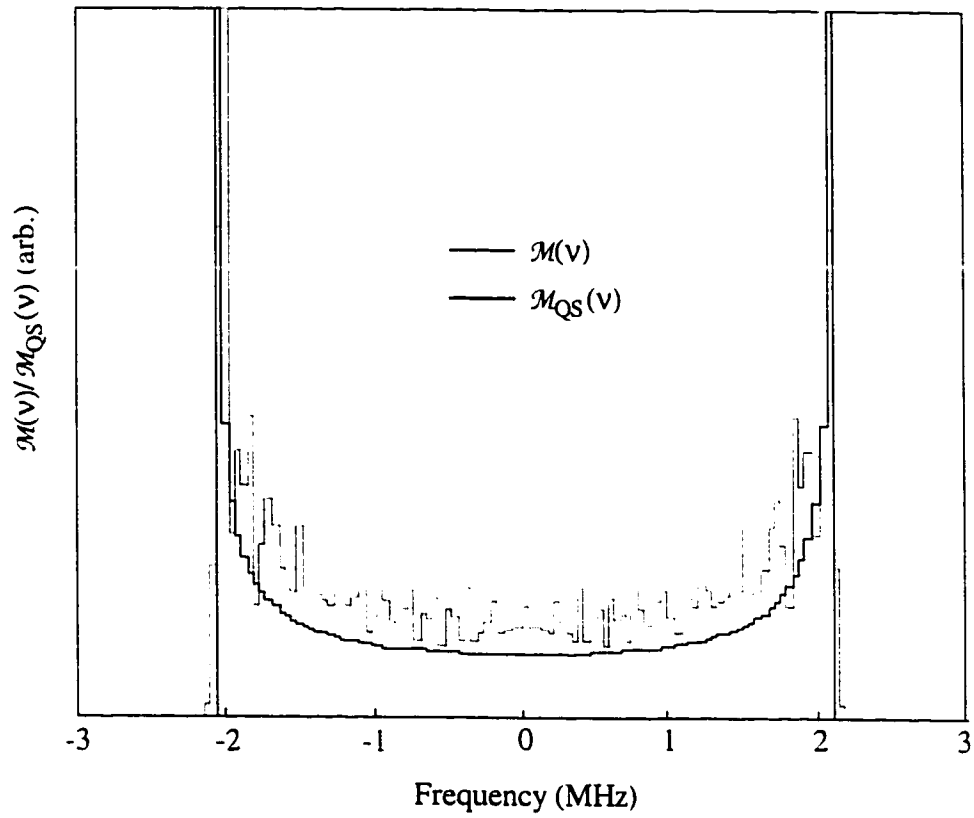

Figure 6.6 - A plot of the exact modulation function and the modulation function obtained by the quasi static approximation for a modulation frequency of $f_m = 10$ kHz and amplitude of $I_m = 2$ μA. Both functions were integrated over consecutive 40 kHz bins.

Note that both functions in Fig. 6.6 have a distinctive double "horn" feature. Under higher amplitude modulation, this feature can be observed directly and was used to calibrate the oscilloscope graticule, as discussed above, in measuring the FM sensitivity of the laser. This frequency difference between the horns reaches a maximum when $f_m \tau_d = 0.5$.

The modified linewidth as a function of the modulation frequency for the two delay line lengths are given by the solid lines in Fig. 6.7. It can be seen that the 5 km line reaches a maximum linewidth at $f_m = 0.5 / \tau_d = 0.5 / 25.6\ \mu s = 19.5$ kHz and returns to the natural linewidth at twice that frequency. The maximum for the 700 m line cannot be seen

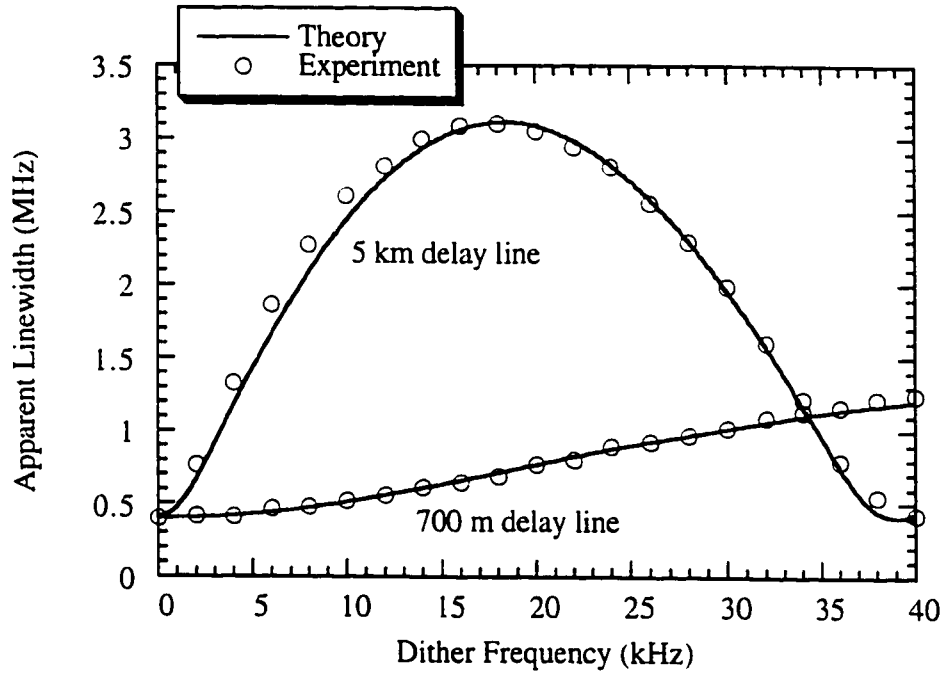

Figure 6.7 - Theoretical and experimental apparent linewidth as a function of frequency for a 5 km and 700 m delay line.

in the frequency range shown because it is at $f_m = 0.5 / 3.6\,\mu s = 139$ kHz. The same conditions of $I_m = 2\,\mu A$ and $f_m = 0...40$ kHz were used experimentally with switch A and B both 'on' in Fig. 6.1 and is indicated by open circles in Fig. 6.7. The single-tone model is evidently confirmed.

6.5 Band-Limited White Current Noise

With the single-tone model confirmed in Section 6.4, it is useful to extend the model to a band of low-density white current noise, as might be found in a typical low-noise current source. The purpose of this section is to provide a discussion of the impact of current noise based on non-rigorous quantitative arguments and then provide rough guidelines on the amount of current filtering required to eliminate current noise effects. A

closed-form frequency-domain expression is derived and is verified with a time-domain computer calculation.

Consider an ideal filter with a narrow passband δf centred about frequency f. The time average variance of the output current is

$$\left\langle (\Delta i)^2 \right\rangle = \begin{cases} I^2 \delta f & \text{between } f - \delta f / 2 \text{ and } f + \delta f / 2 \\ 0 & \text{otherwise} \end{cases}$$

where I^2 is the spectral density (nA^2 / Hz) of the current noise and is assumed constant (white noise). If δf is small enough, then the output of the filter will look like a single tone of frequency f. In Section 6.4, it was found that the PDF of the centre frequency of the laser in the quasi-static approximation was a "horn" function, with both horns approaching infinity at an equal rate at $\nu = \pm 2 S_{FM} I_m \sin(\pi f_m \tau_d)$. The output of the filter is the same with $f_m = f$ and $I_m = I\sqrt{2\delta f}$ (the factor of $\sqrt{2}$ comes from converting rms to amplitude).

The single-tone PDF can be compared favourably to the PDF of a coin toss, which has two delta functions of equal amplitude, one for each orientation: heads and tails. If a toss decides whether a particle moves a fixed distance in the positive or negative direction and a series of independent tosses are made, the total PDF for the net position of the particle is given by the solution to the well-known random walk problem. If the "horns" of the PDF in (6.22) are approximated by two delta functions,

$$\mathcal{M}_{QS}(\nu) \approx \tfrac{1}{2}\left[\delta\left(\nu - 2S_{FM} I (2\delta f)^{1/2} \sin(\pi f \tau_d)\right) + \delta\left(\nu + 2S_{FM} I (2\delta f)^{1/2} \sin(\pi f \tau_d)\right)\right] \qquad (6.23)$$

then the step size, $s_n(f)$, describing the motion of the laser centre frequency for a filter n is

$$s_n(f) = \pm 2 S_{FM} I (2\delta f)^{1/2} \left|\sin(\pi f \tau_d)\right| \ . \qquad (6.24)$$

Now consider a larger low passband of frequencies, B, composed of the summed output of $N (= B / \delta f)$ elemental filters place side-by-side in frequency, each with a centre

frequency f_n. At any moment in time, each of the elemental filters will contribute a frequency shift of the laser line to either the positive or negative frequency side. The output of each of the filters is uncorrelated with respect to the others. If an ensemble of DSH experiments are performed, the average frequency shift over the ensemble, $\langle s_n \rangle$, due to the n^{th} filter is

$$\langle s_n \rangle = 0 \ . \tag{6.25}$$

The total shift of the centre frequency, ν_{tot}, for one member of the ensemble is

$$\nu_{tot} = \sum_{n=1}^{N} s_n \tag{6.26}$$

with the ensemble average of the total frequency shift being

$$\begin{aligned} \langle \nu_{tot} \rangle &= \left\langle \sum_{n=1}^{N} s_n \right\rangle \\ &= \sum_{n=1}^{N} \langle s_n \rangle \\ &= 0. \end{aligned} \tag{6.27}$$

The squared standard deviation of ν_{tot} is

$$\sigma^2 = \left\langle \left(\nu_{tot} - \langle \nu_{tot} \rangle \right)^2 \right\rangle .$$

Expanding the square, applying (6.27), and using the definition (6.26),

$$\begin{aligned} \sigma^2 &= \langle \nu_{tot} \rangle^2 \\ &= \left\langle \left(\sum_{n=1}^{N} s_n \right)^2 \right\rangle \\ &= \left\langle \left(\sum_{n=1}^{N} s_n \right) \left(\sum_{m=1}^{N} s_m \right) \right\rangle . \end{aligned} \tag{6.28}$$

The second sum above can be separated into terms which form direct products with the same terms in the first sum and those which form cross products:

$$\sum_{m=1}^{N} s_m = \sum_{m=n} s_m + \sum_{m \neq n} s_m$$

so that

$$\sigma^2 = \sum_{m=1}^{N} \left\langle (s_m)^2 \right\rangle + \sum_{n=1}^{N} \sum_{m \neq n} \langle s_n s_m \rangle \ . \tag{6.29}$$

Since s_n and s_m are statistically independent for $m \neq n$, the mean of the products is the product of the means:

$$\begin{aligned} \langle s_n s_m \rangle &= \langle s_n \rangle \langle s_m \rangle \quad (n \neq m) \\ &= 0 \end{aligned} \tag{6.30}$$

from (6.25). Equation (6.29) becomes

$$\sigma^2 = \sum_{n=1}^{N} \left\langle (s_n)^2 \right\rangle \ . \tag{6.31}$$

From (6.24),

$$\left\langle (s_n)^2 \right\rangle = (s_n)^2 \tag{6.32}$$

since the two possible values of s_n differ only by a sign. σ^2 can be more easily calculated if the sum in (6.31) is approximated by an integral with $\delta f \rightarrow df$. Using (6.31), (6.32) and (6.24),

$$\begin{aligned} \sigma^2 &= 4 \int_0^B S_{FM}^2 I^2 \sin^2(\pi f \tau_d) df \\ &= 2 S_{FM}^2 I^2 \left[B - \frac{\sin(2\pi B \tau_d)}{2\pi\tau_d} \right] \end{aligned} \tag{6.33}$$

where it has been assumed that S_{FM} is a constant function of f for simplicity. For a large number of small steps, the PDF of a random walk approaches a Gaussian function [23]. The modulation function for band limited white current noise, $\mathcal{M}_{BL}$, is therefore

$$\mathcal{M}_{BL}(v) = \frac{e^{v^2/2\sigma^2}}{\sqrt{2\pi\sigma}} \tag{6.34}$$

which is convolved with the auto-convolved lineshape in place of $\mathcal{M}$ in (6.19). The FWHM of $\mathcal{M}_{BL}$, α_G, is

$$\begin{aligned}\alpha_G &= 2\sqrt{2\ln(2)}\sigma \\ &= 4\sqrt{\ln(2)}S_{FM}I\left[B - \frac{\sin(2\pi B\tau_d)}{2\pi\tau_d}\right]^{1/2}.\end{aligned} \tag{6.35}$$

If the intrinsic laser line is Lorentzian, the noise will produce a Voigt profile for the RF spectrum. The FWHM of the Voigt profile, α_V, is approximately related to the FHWM of the laser line, $\Delta\nu$, and the Gaussian modulation function by

$$\alpha_V = 1.0692 + \tfrac{1}{2}\sqrt{0.866639(\Delta\nu)^2 + 4\alpha_G^2} \tag{6.36}$$

The above discussion describes a situation where a 1/f-like (i. e., Gaussian) component is present in the measured laser line. This component adds a dependence of the measured linewidth on the differential delay time, as has been observed previously [8] and can cause all of the associated properties of linewidth flooring, residual linewidth, and premature re-broadening. However, this phenomenon should be in no way be considered an intrinsic property of the laser for the following reasons:

1. Although the laser centre frequency is changing with time and a long time average would yield a larger overall linewidth, the rate at which the shifting occurs is orders of magnitude slower than the processes usually associated with linewidth, and has limited practical impact on linewidth-related phenomena. For example, it will have no affect on FM to AM conversion noise in analogue optical fibre transmissions [24], [25]. An important exception where white current noise would be important is applications where a high degree of frequency stability is required.
2. The amount of apparent linewidth broadening depends on the experiment being performed. Different current sources will produce different results. As the delay length of the fibre is changed, a different linewidth will be measured. Other measurement methods, such as a Fabry-Perot interferometer locked in quadrature, may also yield different results.
3. Most importantly, the amount of apparent broadening depends unpredictably on such extrinsic effects as the length, type, and positioning of cables used to supply current to the laser, the location of the measurement site relative to equipment that generates electrical noise,

humidity and local weather conditions, *etc.*

Therefore, DSH linewidth broadening due to band-limited current noise is considered to be an error introduced by the improper filtering of the current source. Since the peculiarities of laser chirp mean that it is the largest at very low frequencies, and, as seen in (6.35), the amount of broadening depends not only on the amplitude of the noise but on the bandwidth as well, the magnitude of this artifact has not been previously appreciated. Furthermore, experimental investigations into laser 1/f noise which do not describe in detail careful precautions taken to low-pass filter the current source are highly suspect.

At this point, it is useful to generate guidelines for the high accuracy operating regimes of the DSH technique. The desired delay line length will be a trade-off between two conflicting requirements. There should be sufficient delay to ensure incoherent mixing, yet it should not get so long that problems arise with an increased broadening artifact as described by (6.35). To quantify this trade-off, (6.35) was solved for the intrinsic linewidth which would give rise to a fractional error of ε (i.e., $\alpha_v = (1+\varepsilon)\Delta\nu$). With the help of (6.34),

$$\Delta\nu = \frac{4\sqrt{\ln(2)}S_{FM}I}{\sqrt{(2\varepsilon+0.9308)^2 - 0.866639}}\left[B - \frac{\sin(2\pi B\tau_d)}{2\pi\tau_d}\right]^{1/2}. \qquad (6.36)$$

Equation (6.36) is plotted in Fig. 6.6 (solid lines) as a function of the delay line length, $L_d = \tau_d c / n_g$ where n_g is the fibre group velocity. Three noise bandwidths are shown with an assumed noise amplitude of $1\ \text{nA}/\sqrt{\text{Hz}}$[†], an S_{FM} of 700 MHz/mA, and

[†]As an example, the LDX-3620 Ultra Low Noise Current Source manufactured by the ILX Lightwave Corporation is rated for 100 nA rms noise between 5 Hz and 10 kHz (which corresponds to an average of $I = 1\ \text{nA}/\sqrt{\text{Hz}}$) and a total of 850 nA rms out to 10 MHz (an average over that range of $I = 0.3\ \text{nA}/\sqrt{\text{Hz}}$). This, of course, does not include FM pick-up in the cables or contact noise.

$\varepsilon = 1\%$. The curves describe the minimum natural linewidth for which the current noise incurs no more than a 1% error in measurement. Linewidths below these lines will be measured with decreasing accuracy. The incoherent mixing condition defined by three times the coherence time in (6.1) is indicated by the dashed line.

As a check on the frequency domain approach, a time domain computer model was also employed, where the passband of white current noise was simulated by the sum of a large number of single tones at evenly spaced frequencies. The current waveform was then applied to a hypothetical laser. The resulting signal was used to build a histogram of instantaneous centre frequencies, which was then equated to the modulation function in

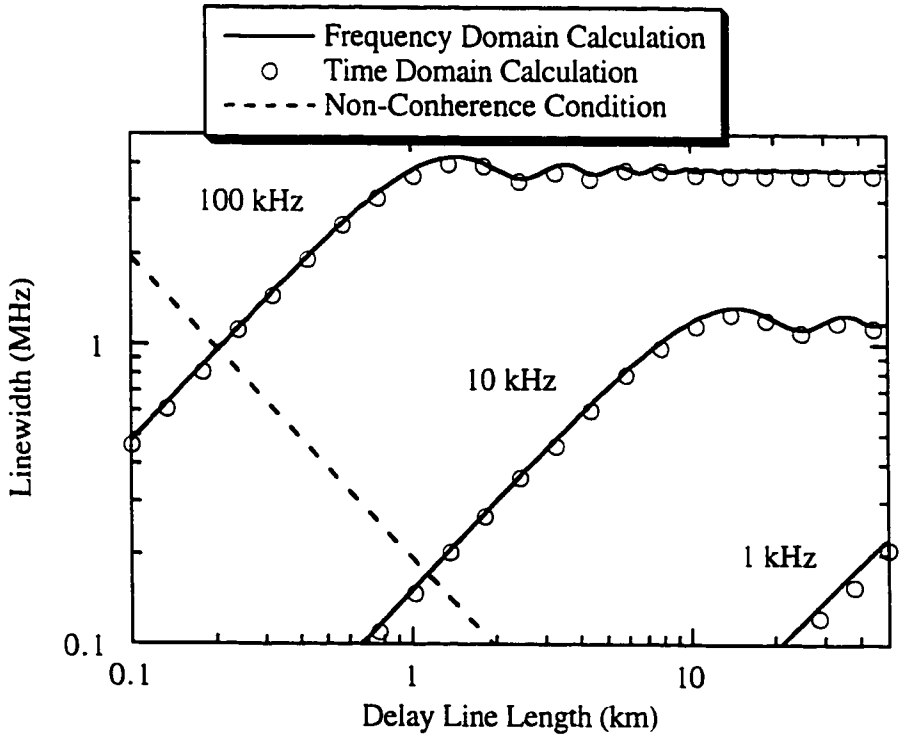

Figure 6.8 - Conditions for accurate linewidth measurements for 1, 10 and 100 kHz noise bandwidths with a current noise density of $I = 1\ \text{nA} / \sqrt{\text{Hz}}$ in the frequency domain model (solid lines) and time domain model (circles). The dashed line indicates the non-coherence condition given by [4]. The contours represent the minimum allowable linewidth at any given delay line length.

accordance with the quasi-static approximation. The results of the simulation are indicated by circles in Fig. 6.8. They agree quite well with the frequency domain equation, with only minor deviations caused by approximating the harmonic oscillator PDF in (6.22) by the two delta functions in (6.23) in the frequency domain model.

As can be seen from Fig. 6.8, linewidth measurement accuracy is greatly enhanced if the current noise bandwidth is tightly controlled. The root-mean-squared (rms) magnitude of the current noise is reduced with a lower noise bandwidth, but as well the more troublesome higher noise frequencies (see Fig. 6.7) will be preferentially suppressed. This should by kept in mind when selecting the bias current source to be used for linewidth measurements. Proper shielding and layout precautions should also be taken to prevent any extraneous noise from being picked up.

6.5 Chapter Summary and Conclusions

It has been observed that the effect of laser-bias current noise on the accuracy of delayed self-homodyne measurements is much more severe than has previously appreciated. In addition to producing an apparent broadening of the laser line, artifacts such as a linewidth floor, residual linewidth, premature re-broadening, and a Gaussian component can be introduced. These phenomena have been discussed in connection with various intrinsic excess noise mechanisms such as mode partition noise and spectral hole burning. However, in the presence of current noise the impact of the intrinsic mechanisms may be greatly overestimated. It was found that simple low-pass filtering of the current source could essentially eliminate all of the above problems.

References

[1] J. Goodwin, K. Prosyk, M. Poirier, "Laser linewidth artifacts using the delayed self-

homodyne technique", *submitted to Appl. Phys. Lett.*

[2] M. O. van Deventer, P. Spano, S. K. Nielsen, "Comparison of DFB laser linewidth measurement techniques results from COST 215 round robin", *Electron. Lett.*, Vol. 26, pp. 2018-2020, 1990.

[3] T. Okoshi, K. Kikuchi, A. Nakayama, "Novel method for high resoution measurement of laser output spectrum", *Electron. Lett.*, Vol. 16, pp. 630-631, 1980.

[4] K. Petermann, *Laser Diode Modulation and Noise*, Kluwer, 1988.

[5] D. Welford, A. Mooradian, "Output power and temperature dependence of the linewidth of single-frequency cw (GaAl)As diode lasers", Appl. Phys. Lett., Vol. 40, pp. 865-867, 1982.

[6] M. Nazarathy, W. V. Sorin, D. M. Baney, S. A. Newton, "Spectral analysis of optical mixing measurements", *J. Lightwave Technol.*, Vol. 7, pp. 1083-1096, 1989.

[7] G. P. Agrawal, N. K. Dutta, *Semiconductor Lasers*, Van Nostrand-Reinhold, 1993.

[8] K. Kikuchi, T. Okoshi, "Dependence of semiconductor laser linewidth on measurement time: evidence of the predominance of 1/f noise", *Electron. Lett.*, Vol. 21, pp. 1011-1012, 1985.

[9] L. B. Mercer, "1/f frequency noise effects on self-heterodyne linewidth measurements", *J. Lightwave Technol.*, Vol. 9, pp.485-493, 1991.

[10] J. Kitching, Y Shevy, J. Iannelli, A. Yariv, "Measurements of 1/f frequency noise reduction in semiconductor lasers using optical feedback with dispersive loss", *J. Lightwave Technol.*, vol. 11, pp. 1526-1532, 1993.

[11] M. P. van Exeter, S. J. M. Kuppens, J. P. Woerdman, "Excess phase noise in self-heterodyne detection", *IEEE J. Quantum Electron.*, vol 28, pp. 580-584, 1992.

[12] R. J. Lang, K. J. Vahala, A. Yariv, "The effect of spatially dependent temperature and carrier fluctuations on noise in semiconductor lasers", *IEEE J. Quantum Electron.*, vol. QE-21, pp. 443-451, 1985.

[13] A. Dandridge, H. F. Taylor, "Correlation of low-frequency intensity and frequency fluctuations in GaAlAs lasers", *IEEE J. Quantum Electron.*, vol. QE-18, pp. 1738-1750, 1982.

[14] G. P. Agrawal, R. Roy, "Effect of injection-current fluctuations on the spectral linewidth of semiconductor lasers", *Phys. Rev. A*, vol. 37, pp. 2495-2501, 1988.

[15] D. Welford, A. Mooradian, "Observation of linewidth broadening in (GaAs)As diode lasers due to electron number fluctuations", *Appl. Phys. Lett.*, vol. 40, pp. 560-562, 1982.

[16] R. J. Fronen, L. K. J. Vandammme, "Low frequency intensity noise in semiconductor lasers", *IEEE J. Quantum Electron.*, vol. 24, pp. 724-736, 1988.

[17] H. Yasaka, M. Fukuda, T. Ikegami, "Current tailoring for lowering linewidth floor", *Electron. Lett.*, vol. 24, pp. 760-762, 1988.

[18] G. P. Li, T. Makino, R. Moore, N. Puetz, K. W. Leong, H. Lu, "Partly gain-coupled 1.55 μm strained-layer multiquantum-well DFB lasers", *IEEE J. Quantum Electron.*, vol. 29, pp. 1736-1742, 1993.

[19] H. E. Rowe, *Signals and Noise in Communication Systems*, Van Nostrand Company Inc., 1965.

[20] J. W. Goodman, *Statistical Optics*, John Wiley & Sons, 1985.

[21] B. Moleshi, "Analysis of optical phase noise in fiber-optic systems employing a laser source with arbitrary coherence time", *J. Lightwave Technol.*, vol. LT-4, pp. 1334-1351, 1986.

[22] S. Ryu, S. Yamamoto, "Measurement of direct frequency modulation characteristics of DFB-LD by delayed self-homodyne technique", *Electron Lett.*, vol. 22, pp. 1052-1054, 1986.

[23] K. Stowe, *Introduction to Statistical Mechanics and Thermodynamics*, John Wiley & Sons, 1984.

[24] K. Petermann, "FM-AM noise conversion in dispersive single-mode fibre transmission lines", *Electron. Lett.*, vol. 26, pp. 2097-2098, 1990.

[25] S. Yamamoto, N. Edagawa, H. Taga, Y. Yoshida, H. Wakabayashi, "Analysis of laser phase noise to intensity noise conversion by chromatic dispersion in intensity modulation and direct detection optical-fiber transmission", *J. Lightwave Technol.*, vol. 8, pp. 1716-1722, 1990.

CHAPTER SEVEN

CONCLUSIONS

7.0 INTRODUCTION

THE preceding chapters have offered a careful examination of some of the most fundamental techniques used to characterize the power and spectral properties of semiconductor lasers. In this chapter, I summarize the results which I believe to be the most significant in terms of their impact on the characterization and understanding of semiconductor lasers. In addition, I would like to take this opportunity to suggest some interesting ways in which the work in this thesis may be extended.

7.1 THESIS SUMMARY

7.1.1 Laser Modeling

A classical, phenomenological model was introduced in Chapter 2 which was able to reproduce basic laser properties. The advantages of the model are its simplicity and the ability to use portions of it directly to analyze experimental data. Additionally, quantities

within the model, such as the logarithmic gain coefficient, can be easily calculated from first principles if desired.

The dependence of the optical power on spontaneous emission, gain and longitudinal position within the laser cavity was derived by two methods. By comparing the results of the two methods it was proven that the power in each mode is separately conserved. Although this has been known for some time from quantum mechanical and classical circuit-equivalent methods, to my knowledge it is the first-ever classical all-optical derivation. From the same equation, a linewidth formula was derived similar to that obtained classically from the transmission-line matrix method, and exhibits the same inverse-power relationship exhibited by quantum-mechanical treatments.

7.1.2 Efficiency and Optical Loss

A large-scale study of the effect of varying well number, length and temperature on the differential quantum efficiency was performed. Variations in the optical loss were observed that could be best explained by the presence of inter-valence band absorption (IVBA). A model based on IVBA was used to infer the gain and loss coefficients as a function of temperature. Results of numerical fits indicate that the dominant mechanisms affecting the differential quantum efficiency fall into two identifiable regimes. IVBA dominates in the normal regime, where the reciprocal of the differential quantum efficiency exhibits the expected linear length dependence. In the anomalous regime, the usual linear length dependence is not followed and changes in the internal efficiency, likely due to hetero-barrier leakage, become significant.

The model confirms a previous observation by others that the presence of IVBA can introduce errors into the internal efficiency and optical loss measured by the standard method. A strategy for avoiding this pitfall was discussed. Because of the high

temperature dependence of the gain coefficient, a highly temperature-sensitive internal efficiency could indicate a problem.

A further interesting result of the model was the successful prediction of the failure of certain devices to lase. The failure to lase was connected to the inability to achieve sufficient gain to overcome the increased optical losses due to high carrier concentrations at high temperature. It was found that the IVBA contribution to the degradation of the differential quantum efficiency could be minimized with an appropriate choice of optical confinement factor.

7.1.3 Temperature Sensitivity of Threshold

The large-scale study was continued by examining the effect of well number and length and the temperature sensitivity of threshold. For this, a slightly re-arranged version of the previously proposed T_{max} equation was employed, and was observed to fit the data with a high correlation factor. A simple phenomenological derivation of the T_{max} equation was presented which gave physical meaning to the parameters involved. It was found that T_{max} was related to the variation of the threshold carrier density with temperature, which is in turn determined by the optical gain and losses. The exponential sensitivity parameter, ζ, was found to be related to the power-law dependence of the current density on the carrier density, explaining the previously observed value of $\zeta \approx 2$. The increase in ζ with well number and length was also explained.

An attempt was made to make predictions of T_{max} based on the gain and loss coefficients measured from the differential quantum efficiency. Although for many lengths and well numbers reasonable agreement was found, there were certain areas of parameter space (long lengths and high well numbers) where discrepancies exist. It was conjectured that non-uniform carrier injection into the quantum wells is responsible for this behaviour.

Finally, the conditions under which the T_{max} equations would accurately describe experimental data were discussed. These are:

(1) the inverse of the threshold carrier density varies linearly with temperature, and

(2) the threshold current density varies over a small enough range that it can be adequately described by a power-law dependence on the threshold carrier density.

7.1.4 Threshold and Gain

The logarithmic gain coefficient was determined for a five quantum-well device by four independent methods: first principles calculation; the new IVBA model; the length dependence of threshold; and direct observation of the below-threshold spectrum of a 250 μm device. All methods agreed to within about 10%, with the exception of the threshold method which yielded a gain coefficient which was about one-half that of the other values. This discrepancy, while having been noted before in the literature as a disagreement between theory and experiment, had not been previously explained. It was discovered by further direct measurements, however, that the source of the disparity is in the unexpected dependence of the gain coefficient on length. Changes in the internal resistive heating with cavity length as a possible cause was rejected because the magnitude did not appear large enough and it could not also explain the changes in transparency current density. Finally, it was described how the previously conjectured non-uniform carrier injection into the quantum wells could be responsible for this phenomenon.

7.1.5 Linewidth

Observations were reported of 1/f-like behaviour of the laser linewidth which appeared to be unrelated to the intrinsic properties of the laser, but rather to the extrinsic conditions relating to the measurement set-up, specifically the degree to which the laser bias

current was filtered. In order to determine the exact cause of the 1/f noise, the effect of current noise on the delayed self-homodyne technique was investigated.

A derivation was given for the RF beat spectrum of a delayed self-homodyne experiment. The mathematics of the problem were simplified by applying the mutual non-coherence of the interferometer arms at an early stage in the problem. The model was then extended to include the presence of a single noise tone, which is the limit of an infinitesimally narrow noise pass band. The model was confirmed experimentally and it was demonstrated that the presence of a noise tone would introduce errors into the technique in the form of artificially inflating the measured linewidth. The model was further extended to include a finite band of white current noise. It was shown, with certain approximations, that the noise would approach the form of a Gaussian linewidth component, as is typically associated with intrinsic 1/f noise mechanisms. The model was used to determine guidelines for appropriately filtering the current source to avoid such errors.

7.2 Recommendations for Future Work

The phenomena influencing the characterization techniques presented suggest a number of interesting areas where further investigation would be productive. One common thread throughout Chapters 3 through 5 was the possibility of non-uniform carrier injection into the quantum wells affecting the performance of the laser. This has been described theoretically [1], [2] and is thought to affect laser dynamics. It could be investigated by designing a laser with quantum wells of varying widths but similar depths. Since the band gap due to the quantum size effect would be different for each well, the recombination rate in each well could be determined by examining the spectrum of spontaneously emitted light. To account for the possibility that different well widths may influence the carrier

capture time of the quantum well, the results could be compared to a device structure which has the ordering of the well widths from the p to n contact reversed.

Although it is encouraging that the model presented in Chapter 3 gives reasonable predictions of T_{max} and gives the correct gain coefficient for five quantum-well lasers at room temperature, it should not be considered proven without further empirical support, preferably direct measurement of IVBA. Direct measurement is problematic since it is difficult to discriminate between band gap absorption and IVBA. An estimate of the influence of IVBA could be obtained by optically probing the laser below the band gap. The spectral output of the laser would be a series of Fabry-Perot fringes with a finesse determined by the facet reflectivity and the optical losses. Part of these losses will be due to scattering, but IVBA could be searched for by changing the bias current below threshold and looking for a carrier-density dependence. The obvious drawback to this method is the fact that the probing does not take place at the lasing wavelength.

Much work still remains to be done regarding the temperature dependence of threshold. Carrier lifetime measurements could be performed to obtain the carrier density dependence of the current density, and compare the temperature dependence of this with the power law relationship used in Chapter 4. A quantity of intense interest which was not discussed in this thesis is the relationship of device design to the maximum operating power as a function of temperature. An investigation into the influence of the characteristic parameters from the T_{max} relation on the maximum operating power under CW and pulsed conditions could provide useful insight into some of the contributing mechanisms.

By eliminating the errors introduced into the delayed self-homodyne technique due to current noise, reliable studies of intrinsic 1/f-noise and linewidth re-broadening can be conducted. A further possible concern is linewidth de-stabilization due to minute drifting of the temperature from air currents, which can be eliminated by using an evacuated

chamber. This may have an effect on linewidth measurements which was not accounted for in Chapter 6.

REFERENCES

[1] G. Debaisieux, G. Herve-Gruyer, M. Filoche, S. Bouchoule, J. F. Palmier, "Self-consistent 1-D solution of multiquantum-well laser equations", *Opt. Quantum Electron.*, vol. 29, pp. 651-660, 1997.

[2] C. H. Lin, C. L. Chua, Z. H. Zhu, Y. H. Lo, "On nonuniform pumping for multiple-quantum well semiconductor lasers", vol. 65, pp. 2383-2385, 1994.